NUMERICAL PREDICTION OF INTERMITTENT TWO-PHASE FLOW IN HORIZONTAL AND INCLINED PIPELINES AND COMPARISON WITH EXPERIMENTS

Carina Nogueira Sondermann

Tese de Doutorado apresentada ao Programa de Pós-graduação em Engenharia Mecânica, COPPE, da Universidade Federal do Rio de Janeiro, como parte dos requisitos necessários à obtenção do título de Doutor em Engenharia Mecânica.

Orientadores: Gustavo César Rachid Bodstein
Felipe Bastos de Freitas Rachid

Rio de Janeiro
Junho de 2021

NUMERICAL PREDICTION OF INTERMITTENT TWO-PHASE FLOW IN HORIZONTAL AND INCLINED PIPELINES AND COMPARISON WITH EXPERIMENTS

Carina Nogueira Sondermann

TESE SUBMETIDA AO CORPO DOCENTE DO INSTITUTO ALBERTO LUIZ COIMBRA DE PÓS-GRADUAÇÃO E PESQUISA DE ENGENHARIA DA UNIVERSIDADE FEDERAL DO RIO DE JANEIRO COMO PARTE DOS REQUISITOS NECESSÁRIOS PARA A OBTENÇÃO DO GRAU DE DOUTOR EM CIÊNCIAS EM ENGENHARIA MECÂNICA.

Orientadores: Gustavo César Rachid Bodstein
Felipe Bastos de Freitas Rachid

Aprovada por: Prof. Gustavo César Rachid Bodstein
Prof. Felipe Bastos de Freitas Rachid
Prof. Manuel Ernani de Carvalho Cruz
Prof. Gustavo Rabello dos Anjos
Profª. Maria Laura Martins Costa
Prof. Eduardo Pereyra

RIO DE JANEIRO, RJ - BRASIL
JUNHO DE 2021

Sondermann, Carina Nogueira

Numerical Prediction of Intermittent Two-Phase Flow in Horizontal and Inclined Pipelines and Comparison with Experiments/ Carina Nogueira Sondermann. – Rio de Janeiro: UFRJ/COPPE, 2021.

XX, 145 p.: il.; 29,7 cm.

Orientadores: Gustavo César Rachid Bodstein

Felipe Bastos de Freitas Rachid

Tese (doutorado) – UFRJ/ COPPE/ Programa de Engenharia Mecânica, 2021.

Referências Bibliográficas: p. 120-128.

1. Two-Phase Flow. 2. Numerical Simulation. 3. Intermittent Flow. I. Bodstein, Gustavo César Rachid *et al.* II. Universidade Federal do Rio de Janeiro, COPPE, Programa de Engenharia Mecânica. III. Título.

Agradecimentos

Gostaria de agradecer muitas pessoas que fizeram parte desta longa caminhada até a conclusão deste trabalho.

Agradeço aos meus professores orientadores Gustavo Bodstein e Felipe Rachid que sempre me motivaram e me guiaram com sabedoria no desenvolvimento deste trabalho. Vocês foram fundamentais para tornar meu sonho em realidade.

Gostaria de agradecer ao meu marido Raphael Viggiano por todos os anos juntos e por fazer parte de todas as minhas conquistas. Mais do que ninguém você esteve junto comigo durante todo o trabalho e sabe o quanto a concretização dele é importante para mim.

Agradeço a minha família por todo apoio e amor incondicional que recebi durante toda a minha vida. Meu pai Roberto, minha mãe Marcia, minhas irmãs Melissa e Simone são minhas maiores fontes de inspiração.

Sou grata também aos meus amigos e colegas do Laboratório de Mecânica dos Fluidos e Aerodinâmica (LABMFA): Aline, Jaciara Roberta, Rodrigo, Antônia e Lionel por todos os dias de convivência e troca de experiências.

Agradeço aos professores Eduardo Pereyra e Cem Sarica pela oportunidade e por todo aprendizado obtido na Universidade de Tulsa. Também gostaria de agradecer aos amigos, colegas e técnicos da Universidade de Tulsa pelo acolhimento e cuidado comigo em toda a minha estadia nos EUA.

Gostaria de agradecer à CAPES e à Petrobras pelo apoio através de bolsas de estudos que foram fundamentais para que este trabalho fosse concretizado.

Resumo da Tese apresentada à COPPE/UFRJ como parte dos requisitos necessários para a obtenção do grau de Doutor em Ciências (D.Sc.)

PREDIÇÃO NUMÉRICA DE ESCOAMENTO BIFÁSICO INTERMITENTE EM DUTOS HORIZONTAIS E INCLINADOS E COMPARAÇÃO COM EXPERIMENTOS

Carina Nogueira Sondermann

Junho/2021

Orientadores: Gustavo César Rachid Bodstein
Felipe Bastos de Freitas Rachid

Programa: Engenharia Mecânica

Simulações numéricas de escoamento bifásico intermitente são importantes para acompanhar e prever o comportamento desse padrão de escoamento ao longo de uma tubulação. Alguns trabalhos antecessores provaram que o modelo de dois fluidos unidimensional e transiente é capaz de capturar golfadas automaticamente, apenas como resultado da dinâmica do escoamento. Neste trabalho, duas abordagens para o modelo de dois fluidos em combinação com diferentes métodos numéricos são implementadas. Os modelos matemáticos propostos possuem cinco e sete equações, são incondicionalmente hiperbólicos e são avaliados para simular problemas benchmark. O modelo numérico que melhor reproduz os problemas benchmarks é utilizado para simular casos de escoamento intermitente através do método de captura de golfadas. Resultados obtidos com a modelagem numérica são comparados com caso da literatura e com dados experimentais obtidos através de uma campanha experimental que também é parte deste trabalho. Os resultados demonstram que o modelo numérico é bastante promissor, apresentando boa concordância para algumas características de golfadas, como frequência e velocidade translacional, embora possivelmente ajustes sejam necessários a fim de contemplar efeitos que são intrinsicamente tridimensionais e influenciam no escoamento.

Abstract of Thesis presented to COPPE/UFRJ as a partial fulfillment of the requirements for the degree of Doctor of Science (D.Sc.)

NUMERICAL PREDICTION OF INTERMITTENT TWO-PHASE FLOW IN HORIZONTAL AND INCLINED PIPELINES AND COMPARISON WITH EXPERIMENTS

Carina Nogueira Sondermann

June/2021

Advisors: Gustavo César Rachid Bodstein
Felipe Bastos de Freitas Rachid

Department: Mechanical Engineering

Numerical simulations of intermittent two-phase flow are important to monitor and predict the behavior of this flow pattern along a pipe. Some previous works have proved that the transient one-dimensional two-fluid model is capable of capturing slugs automatically, just as a result of the flow dynamics. In this work, two approaches of the two-fluid model in combination with different numerical methods are implemented. The proposed mathematical models have five and seven equations, are unconditionally hyperbolic and are evaluated to simulate benchmark problems. The numerical model that best reproduces the benchmark problems is used to simulate cases of intermittent flow through the slug capturing approach. Results obtained with the numerical model are compared with a literature case and with experimental data obtained through an experimental campaign that is also part of this work. The results demonstrate that the numerical model is promising, presenting good agreement for some slug characteristics, such as slug frequency and translational velocity, although adjustments to contemplate effects that are intrinsically three-dimensional and that have an impact on the flow may be needed.

Contents

List of Figures

List of Tables

List of Symbols

Latin letters:

A	Cross-section area [m²]
A_k	Cross-section are for each phase $k \in$ (G,L) [m²]
A	Jacobian matrix
B	Matrix defined in the Roe method derivation
B_{fk}	Body force for each phase $k \in$ (G,L) [kg/(m^{2}s^2)]
b_R	Combined systematic uncertainty
C	Matrix defined in the Roe method derivation
C_D	Drag coefficient defined in Eq. (3.72)
C_{DT}	Parameter defined in Eq. (3.73)
C_f	Fanning friction parameter
C_V	Critical wave velocity for the inviscid analysis
C_{IV}	Critical wave velocity for the viscous analysis
c	Common speed of sound for the AUSM-type methods [m/s]
c_k	Speed of sound for each phase $k \in$ (G,L) [m/s]
c_0	Distribution coefficient for Eq. (3.76)
$c_{G/D}$	Gas and droplets mixture wave speed [m/s]
$c_{L/B}$	Liquid and bubbles mixture wave speed [m/s]
D	Matrix defined in the Roe method derivation
D	Diameter [m]
D_{hk}	Hydraulic diameter for each phase $k \in$ (G,L) [m]
d_B	Bubble diameter [m]
E	Matrix defined in the Roe method derivation
E_o	Eötvös number
f_F	Fanning friction factor
f_I	Friction factor at the interface
f_k	Friction factor for each phase $k \in$ (G,L)
F	Flux vector
$\mathbf{F}^{\mathrm{AUSM}}$	Flux term for AUSM-type methods

$\mathbf{F}^C$	Convective flux term for AUSM-type methods
$\mathbf{F}^p$	Pressure flux term for AUSM-type methods
Fr	Froude number
G	Damping function
g	Gravity [m/s²]
h_L	Liquid height [m]
$\mathbf{H}$	Matrix of non-conservative terms
$\mathbf{J}$	Transformation matrix
$\mathbf{J^{-1}}$	Inverse transformation matrix
K	Constant for the instability analysis
K	Temporary variable
L	Pipeline length [m]
m	Function defined in Eq. (4.27)
$\mathbf{M_1}$	Matrix defined in the hyperbolicity analysis
$\mathbf{M_2}$	Matrix defined in the hyperbolicity analysis
$\mathbf{N}$	Matrix defined in Eqs. (4.3) and (4.6)
n	Fanning friction parameter
N	Number of computational cells along the pipe
N_p	Number of data points
N_S	Number of systematic uncertainty sources
N_{vis}	Dimensionless viscosity
p_k	Pressure for each phase $k \in$ (G,L) [Pa]
p_{Ik}	Interfacial pressure for each phase $k \in$ (G,L) [Pa]
$P^{\pm}$	Pressure-weighted factor for the AUSM-type methods
P	Momentum [kg.m/s]
P_{ref}	Momentum for the reference solution [kg.m/s]
$\mathbf{Q}$	Conservative variables vector
Q	Variable defined in Eq. (7.11)
$\mathbf{r}$	Right eigenvectors written in columns
$\mathbf{R}$	Right eigenvectors matrix
$\mathbf{R^{-1}}$	Inverse matrix of $\mathbf{R}$
Re_k	Reynolds number for each phase $k \in$ (G,L) or $k \in$ I for the interface

Re_{sk}	Reynolds number for each phase $k \in$ (G,L) related to the superficial velocity
r_P	Relaxation parameter
s	Signal function defined in Eq. (4.27)
$\mathbf{S}$	Source terms vector
S_I	Wet perimeter for the interface [m]
S_k	Wet perimeter for each phase $k \in$ (G,L) [m]
ss	Weighted parameter for the AUSMDV method
S_X	Standard deviation
$S_{\bar{X}}$	Standard deviation of the average
t	Time [s]
t^n	Time discretization
T_I	Interfacial drag force per unit volume [kg/(m^{2}s^2)]
T_{kw}	Drag force per unit volume between the fluid k and the wall [kg/(m^{2}s^2)]
U	Propagated uncertainty
u_d	Drift velocity [m/s]
u_I	Interfacial velocity [m/s]
u_k	Velocity for each phase $k \in$ (G,L,B,D) [m/s]
u_m	Mixture velocity [m/s]
u_s	Mean velocity in the slug body [m/s]
u_{sk}	Superficial velocity of phase $k \in$ (G,L) [m/s]
u_t	Translational velocity [m/s]
$U_{u_{tP}}$	Uncertainty associated to Bendiksen's correlation for translational velocity
U_{95}	Overall uncertainty
$\tilde{V}^{\pm}$	Velocity defined in Eq. (4.14)
$\boldsymbol{w}$	Waves crossing the cell interface
$\boldsymbol{W}$	Primitive variables vector
x	Longitudinal cartesian coordinate [m]
X	Temporary variable
$\bar{X}$	Average value of all data points
$\mathbf{x}$	Vector defined in Eq. (4.28)

X_i	Data points
$\mathbf{y}$	Vector defined in Eq. (4.28)
Y	Temporary variable
$\mathbf{z}$	Vector defined in Eq. (4.28)
Z	Temporary variable

Greek letters:

α_k	Volume fraction for each phase $k \in$ (G,L,B,D)
β	Variable defined in Eq. (4.35)
δ	Dimensionless parameter defined in Eq. (3.42)
Δt	Time variation [s]
Δx	Distance variation [m]
$\Delta p_{I,k}$	Pressure correction term for each phase $k \in$ (G,L)
ζ	Parameter defined in Eq. (3.62)
$\boldsymbol{\eta}$	Matrix defined in the Roe method derivation
θ	Pipeline inclination angle with the horizontal [degree]
λ	Eigenvalues [m/s]
λ_{max}^{n}	Largest eigenvalue of the flow domain [m/s]
μ_k	Viscosity for each phase $k \in$ (G,L) [Pa.s]
ξ	Relative error
ρ_k	Density for each phase $k \in$ (G,L,B,D) [kg/m³]
ρ_k^0	Reference density for each phase $k \in$ (G,L,B,D) [kg/m³]
σ	Surface tension [N/m]
τ	Temporal lag [s]
τ_I	Interfacial shear stress [Pa]
τ_k	Wall shear stress for each phase $k \in$ (G,L) [Pa]
Φ	Flux limiter function
χ	Parameter defined in Eq. (4.15)
Ψ	Variable defined in Eq. (4.38)
ψ	Parameter defined to obtain the instantaneous pressure relaxation

Acronyms:

AUSM	Advection Upstream Splitting Method
AUSMD	Advection Upstream Splitting Method biased towards Flux Difference Splitting
AUSMDV	Balance between AUSMV and AUSMD
AUSMV	Advection Upstream Splitting Method biased towards Flux Vector Splitting
CAPES	Coordenação de Aperfeiçoamento Pessoal de Nível Superior (Brazilian Federal Government Agency)
CFL	Courant-Friedrichs-Lewy
CS	Conductivity/Capacitance Sensor
DFM	Drift Flux Model
DP	Differential Pressure Transducer
FCT	Flux-Corrected Transport
FDS	Flux Difference Splitting
FORCE	First Order Centered Scheme
FVS	Flux Vector Splitting
HEM	Homogeneous Equilibrium Model
HLL	Harten, Lax and van Leer
IKH	Inviscid Kelvin Helmholtz
PDSE	Programa de Doutorado Sanduíche no Exterior (Brazilian program from CAPES to sponsor students to do part of their studies abroad)
PT	Pressure Transmitter
QCV	Quick Closing Valve
RTD	Resistance Temperature Detector
TFM	Two-Fluid Model
TT	Temperature Transmitter
TUFFP	Tulsa University Fluid Flow Projects
TVD	Total Variation Diminishing
VKH	Viscous Kelvin Helmholtz
WMS	Wire Mesh Sensor

4E1P	4 Equations and 1 Common Pressure
5E2P	5 Equations and 2 Pressures
7E2P	7 Equations and 2 Pressures

Subscript:

k	General phase, $k \in$ (G,L,B,D)
j	Spatial discretization

Superscript:

L	Left
R	Right
p	Number of eigenvalues
n	Evolution in time

1. Introduction

1.1 Motivation

Gas-liquid two-phase flows are present in many engineering applications that are particularly important to the world energy generation. The performance of those processes is related to the correct characterization of the engineering parameters of the flow and in the prediction of possible failures during their operation. Two-phase flow engineering problems can be encountered, for instance, in the design of flow separators, in thermal systems of nuclear reactors and in the entire oil and gas production chain.

In the oil and gas field, two-phase flow pipelines transport the mixture of oil and natural gas from platforms to the processing units. Along those pipelines, the flow can be characterized by different flow patterns, depending on gas and liquid flow rates, pipeline inclination and diameter, and fluids properties. For horizontal and slightly inclined pipelines, the flow patterns can be classified as stratified, intermittent, annular, or dispersed bubble, as presented by Taitel and Dukler (1976).

The intermittent flow is denoted by the alternate passage of a bubble of gas and a liquid slug. The gas bubble may carry droplets with it and the liquid slug can be aerated, containing dispersion of small gas bubbles entrained, or not. According to Issa and Kempf (2003), the slugs are formed due to natural growth of hydrodynamic instabilities or liquid accumulation originated by the pressure and gravitational forces. Consequently, the waves that grow at the interface between the fluids fill the pipe section with liquid blocking the passage of gas and travel along the line.

The intermittent flow is not always desired in the oil and gas industry, since its intermittent behavior allows the flow rates to oscillate in such a way that can impact the equipment that catch the flow in its destination. This severe unsteady flow in the pipelines can compromise the efficiency of the production and the entire system. In addition, it can cause the appearance of corrosion and pipeline fatigue, as pointed out by Fan (2017).

This work is primarily motivated by the demand for reliable numerical tools to assist the oil and gas industries when dealing with transient two-phase flow situations. The prediction of two-phase flows has always been an important issue to be addressed in the design stage of gas-liquid pipelines and during their operation. The intermittent flow pattern occurs in a wide range of liquid and gas flowrates, and it has fundamentally

complex dynamics with unsteady behavior. The challenging prediction of the slug flow characteristics has motivated the development of several works in the open literature. However, the problem is still far from having a complete numerical model that can accurately predict the unsteady flow variables and their space distribution along the pipe, as well as the main slug characteristics, such as slug length, slug frequency, translational velocity and pressure drop.

Therefore, it is crucial to predict the onset and evolution of such flow pattern along the line aiming to decrease costs and avoid unnecessary waste of the resources. Since the formation of an intermittent flow has a non-steady nature, a transient numerical simulation that can represent the physics of such flow will give a more accurate and complete information regarding its behavior.

1.2 Present Contribution

The numerical simulation of slug flows can be tackled in many ways, including the slug capturing approach, where the onset and evolution of the slug flow is numerically calculated. The analysis of the problem from a numerical viewpoint involves the use of a transient one-dimensional mathematical model comprised of a set of governing nonlinear partial differential equations that is able to describe the physics of the flow combined with a robust numerical technique that will accurately solve the system of equations.

The contribution of this work lies on the development of a numerical model that can predict the intermittent flow in horizontal and inclined pipelines through slug capturing numerical simulations. This study contributes to the area of two-fluid-model slug simulation since it offers two numerical models, comprised of two formulations – the 5E2P and the unprecedented 7E2P models – combined with the AUSM-family of numerical methods and the approximate Riemann solver Roe. This work presents a systematic study of the implemented models and methods in order to analyze their behavior when reproducing benchmark problems solutions and a slug capturing simulation that is described in the literature. The numerical results indicate that the combination of the 5E2P model with the AUSMDV method provides the most promising numerical model to simulate the intermittent flow. The capability of the numerical model in predicting the slug flow is also verified when the simulated results are compared with experimental data acquired during an experimental campaign carried out throughout this

work. This comparison includes a wide range of flow scenarios, varying from horizontal to 30° of inclination, and for low and high viscosity fluids.

1.3 Objectives

The general objective of this work is to develop a numerical model based on the transient one-dimensional two-fluid model to simulate the onset and evolution of the intermittent flow pattern using the approach referred to in the literature as slug capturing. The model is a combination of a one-dimensional mathematical model with a robust and accurate numerical method that must allow the unsteady fields of the flow variables and the main slug characteristics, such as slug frequency, translational velocity, pressure drop, to be calculated.

Specifically, this work has four objectives. The first is to implement two different mathematical approaches of the transient gas-liquid one-dimensional two-fluid model. The first mathematical model has five partial differential equations with two pressures (one for each phase), the 5E2P model, which is comprised of one mass and one momentum equation for each phase (gas and liquid), in addition to one evolution equation for the void fraction. The other model has seven equations and two pressures (one for each phase), the 7E2P model, and assumes the presence of two additional phases, bubbles in the liquid phase and droplets in the gas phase. Therefore, the seven-equation model has fours mass conservation equations, one for each phase, two momentum equations, one for the mixture gas and droplets and another for liquid and bubbles. The last equation is the evolution of the gas and droplets volume fractions. Those two approaches are herein tested and the differences between them are addressed.

The second specific objective of this work is to test and compare different numerical methods to simulate the slug capturing. Numerical methods are analyzed, such as the approximate Riemann solver of Roe and the AUSM-type of methods, and the best scheme is selected based on studies performed with benchmark problems well described in the literature. Advantages and disadvantages are pointed out in order to select the most applicable method for the desired application.

This work also aims to obtain slug flow data by performing an experimental campaign at North Campus's experimental facilities at the University of Tulsa, in Tulsa, Oklahoma, USA. In this experimental campaign, two experimental facilities are used to run two-phase tests. The 4-inch facility is supplied with water and air and can be inclined, while

the 2-inch facility is filled up with synthetic oil and air and is in the horizontal condition. This part of the work was encouraged by CAPES under the PDSE program.

The last objective of this work is to compare the numerical results with the experimental data to verify if the proposed numerical model accurately predicts the desired flow dynamics and main slug characteristics.

1.4 Structure of the Work

In chapter 2, a literature review is presented, showing publications that were relevant to the development of this work.

Chapter 3 is dedicated to describing the mathematical models that are used in the numerical simulations of this study.

In chapter 4, the numerical methods are presented in detail, as well as the discretization techniques.

In chapter 5, the experimental campaign is detailed, showing the experimental facilities schematics and instrumentation.

Chapter 6 is devoted to present all the results obtained with the benchmark problems study encompassing the mathematical models and numerical methods. In addition, an accuracy check of the selected numerical method is performed.

The slug capturing results and the comparison with experiments are presented in chapter 7.

Finally, the conclusions of the work are presented with comments and future work recommendations in chapter 8.

At the end of the text, Appendix A presents more details regarding the Roe scheme. Appendix B shows the single-phase tests that were run at the experimental facilities and Appendix C brings the uncertainty analysis.

2. Literature Review

In this chapter, a literature review based on articles and publications that were relevant in the development of this work are presented. In addition, important information regarding two-phase flow is also described.

2.1 Two-Phase Flow Patterns

In gas-liquid two-phase flow in pipelines, the simultaneous transport of gas and liquid phases presents remarkable physical phenomena characterized by a variety of flow patterns that can be formed due to the development a gas-liquid interface. Consequently, the two-phase flow in a pipe is much more complex than its single-phase counterpart and is categorized according to its topological features and flow parameters. According to Taitel and Dukler (1976), in horizontal and slightly inclined pipelines, two-phase flow can be classified as stratified flow, dispersed bubble flow, annular flow and intermittent flow, as illustrated in Fig.1.

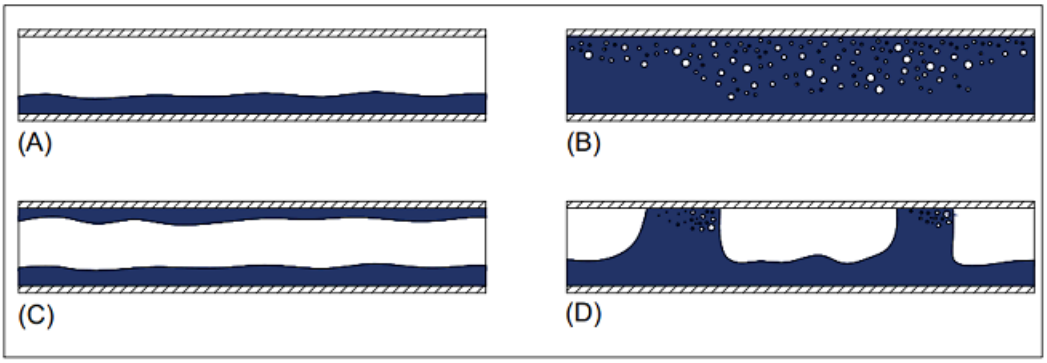

Figure 1: Two-phase flow patterns for horizontal and slightly inclined pipelines. (A) Stratified Flow, (B) Dispersed Bubble Flow, (C) Annular Flow and (D) Intermittent Flow.

In horizontal pipelines, at low flow rates, the gas phase spontaneously moves on top of the liquid film, configurating the stratified flow pattern. An increase of gas flow rate at constant liquid flow rate causes the stratified flow to form small waves at the interface. As the liquid speeds up, these waves can grow and bridge the top of the pipe and the intermittent flow appears. For higher gas flow rates, the annular flow appears with the liquid phase tending to form a ring around the pipe wall. Finally, at higher liquid flow

rates, the dispersed bubble flow may occur in the pipe, in which the gas bubbles tend to concentrate in the upper part of the pipe due to buoyancy.

Since classification and description of the flow distributions into different patterns are subjective by visual observation, some authors, such as Shoham (2006) subcategorize the intermittent flow into slug and elongated bubble flow. When the liquid slug body is almost free of gas bubbles, the plug flow or elongated bubble flow is achieved, whereas the slug flow is found at higher gas velocities in the presence of entrained gas bubbles. There is also a pseudo-slug flow, in which there are large surges of liquid that do not fill the whole pipe cross section, as detailed by Lin and Hanratty (1987).

2.2 Average Procedure of the Governing Equations

The usage of the complete set of three dimensional Navier-Stokes equations to characterize two-phase flow in long pipes is still not practical due to the time constraint and the computational power that is demanded. The presence of a deformable interface between the phases constitutes an additional and complex matter, as pointed out by Ishii and Hibiki (2006). To mitigate this difficulty, averaging procedures are used in the equations, turning the problem into the one-dimensional context and, thus, reducing the computational cost involved in solving those equations (Drew and Passman, 1999).

From a physical viewpoint, especially when transient events become relevant, the one-dimensional formulation is the most suitable approach since long pipelines with lengths far greater than their diameters are considered. In the work of Ishii and Hibiki (2006), the authors show that one-dimensional equations can be obtained using an area-averaging procedure derived from the full three-dimensional Navier-Stokes equations. This one-dimensional approach is extensively used to model such flows.

2.3 Two-Phase Flow Mathematical Models

In the two-phase flow literature, there are three main frameworks to approach the modeling of one-dimensional two-phase flows: homogeneous equilibrium model (HEM), drift-flux model (DFM) and the two-fluid model (TFM).

The first model, HEM, is the one with the less complex system of equations, which is similar to a single-phase formulation. This model consists of one mass, one momentum and one energy equations. According to this formulation, gas and liquid phases are

considered as a mixture where the physical properties of the dominant phase prevail. Moreover, in this model, it is assumed that the velocity, pressure and temperature are equal for both phases. Clerc (2000) uses the HEM model to simulate two-phase flow and concludes that this is not the best model when it is desired to contemplate kinetic or thermodynamic non-equilibrium effects, where more equations are required.

The second model, the DFM, uses a single pressure and a single temperature for the gas and liquid phases. However, the velocities of the fluids are assumed to be different. This mathematical model is comprised of one momentum equation that relates the differences in the phase velocities, two equations of conservation of mass and one equation of conservation of energy for the mixture. Supplementary relations are required to obtain the necessary information for determining the motion of each phase separately. These relations are often referred as the drift velocity equations. Some authors, such as Masella *et al*. (1998), Ishii and Hibiki (2003) and Santim and Rosa (2015) used this model to simulate two-phase flows in pipes. In the work of Munkejord (2005), the author analyzes the behavior of different numerical methods when solving benchmark problems concerning two-phase isothermal flows formulated using the DFM and the TFM. The DFM showed to be a simpler model and more easily derived if compared to the TFM, due to its reduced number of equations. However, it is important to state that this model is not suitable to perform slug capturing simulations, since the interface terms are suppressed from the momentum equations.

The third model, the TFM, is known as the most robust model for two-phase flows since both phases are described independently which means that each phase has its own kinematics and therefore separate mass and momentum equations. For that reasons, the TFM is the one used in the present work. Some authors in the literature, such as Fabre and Peresson (1989) and Munkejord (2005), to name a few, also used this type of modeling in their work as a better way to describe the physics of the flow.

2.4 Different Approaches of the Two-Fluid Model (TFM)

The TFM can be written in many ways, depending on the desired application of the model and on the flow hypotheses that are assumed in the solution. The most commonly used assumption for this model is the isothermal flow, in which thermal effects are not considered and the energy equation(s) is (are) neglected. In the work of Ransom and Hicks (1984), the authors used a particular nomenclature to distinguish the types of

modeling for the TFM. Therefore, following this nomenclature, the mathematical model that disregards the energy equation(s) has two mass and two momentum equations, one for each phase, and is referred as 4E1P for short, in allusion to four equations and one common pressure for the phases. The 4E1P model has been used by many authors such as Issa and Kempf (2003), Omgba-Essama (2004), Figueiredo *et al.* (2017) for different applications.

Whenever thermal effects between the phases and/or the environment are relevant, the 4E1P model is no longer suitable and the energy equation(s) must be included. The simplest way is to write only one energy equation for both phases as a mixture. This strategy admits as a basic assumption that the phases are always in thermal equilibrium and, thus, share the same temperature. The energy equation written for the mixture was used by Abbaspour *et al.* (2010), Sondermann (2016) and is implemented in the commercial software OLGA (Schlumberger). When there is no thermal equilibrium between the phases and the phases temperatures are different, two energy equations are necessary, as presented by Simões *et al.* (2014).

According to Prosperetti (2007), Figueiredo *et al.* (2017), Azizi *et al.* (2018) and Sondermann *et al.* (2019), the above-mentioned models are conditionally hyperbolic, which means that they may render complex eigenvalues that turn the model ill-posed and, consequently, non-physically representative. The mathematical model's capability of representing the correct physics of the flow is directly related to well-posedness of the problems.

Ransom and Hicks (1984), investigating hyperbolic two-pressure models for two-phase flow, proposed the isothermal five-equation and a non-isothermal eight-equation models, with two local distinct pressures, one for each phase. Later, Baer and Nunziato (1986), motivated by the deflagration-to-detonation transition problem in two-phase mixtures and inspired by Ransom and Hicks (1984), suggested a seven-equation model. The five-equation model, called 5E2P for short, consists of one mass and one momentum equation for each phase, in addition to one evolution equation for the void fraction, which is assumed to be advected throughout the domain by an interfacial velocity. The eight-equation model has the same 5E2P model's equations with the addition of one energy equation for each phase and one transverse momentum balance equation. Besides, the seven-equation model have the same mass, momentum and energy equations for each phase and the void fraction evolution equation, but it does not take into account the transverse momentum balance equation. The two-pressure models have been widely used

by several different researchers, such as Saurel and Abgrall (1999), Munkejord (2007), Munkejord *et al.* (2009) and Furfaro and Saurel (2015). The great advantage of the 5E2P model, over the 4E1P model, in particular, is the analytical and always real eigenvalues, derived from a fifth-order polynomial equation. The 5E2P model is unconditionally hyperbolic, which means that the model is well-posed and able to provide results that are representative of the physics of the flow.

The TFM includes even more sophisticated models, by adding more equations to the existing ones. For instance, if gas bubbles and/or liquid droplets phases are introduced in the physical modeling, equations to characterize the dynamics of the new phases must be also accounted for. It is worth mentioning that the hyperbolicity of the models must be checked every time a new equation is inserted in the formulation.

2.5 Previous Work on Intermittent Flow

Several studies on two-phase flow, especially in intermittent flow pattern, have been conducted over the years and the most important ones are reported in this section.

2.5.1 Hydrodynamic Slug Formation Mechanism

Slug flow appears in horizontal, inclined and also vertical pipes for a large span of liquid and gas flow rates. In horizontal and nearly horizontal pipes, the slug flow can be generated from stratified flow by either the natural growth of hydrodynamic instabilities or liquid accumulation at the valleys of irregular pipelines. According to Issa and Kempf (2003), the specific transition generally occurs due to the continuous growth of interface instabilities, which develop into small-amplitude long waves. In such cases, small perturbations of short waves that increase naturally may grow into larger waves on the surface of the liquid. These instabilities are calculated by means of the Kelvin-Helmholtz instability theory, which has been frequently used to determine whether a smooth stratified flow is stable or unstable to generate slug flow.

Barnea and Taitel (1993, 1994) used stability analysis for two-phase flow to determine the inviscid (IKH – Inviscid Kelvin Helmholtz) and viscous (VKH – Viscous Kelvin Helmholtz) conditions in which perturbation of the equilibrium generates disturbance that grow into waves that evolve into slug flow. This relation is expressed as

$$(u_G - u_L) < K \sqrt{(\rho_L \alpha_G + \rho_G \alpha_L) \frac{\rho_L - \rho_G}{\rho_L \rho_G} g \cos\theta \frac{A}{\frac{dA_L}{dh_L}}}, \tag{2.1}$$

where for the inviscid case (IKH) K=1 and for the viscous case (VKH), K is expressed as

$$K = \sqrt{1 - \frac{(C_V - C_{IV})^2}{\frac{\rho_L - \rho_G}{\frac{\rho_L}{\alpha_L} + \frac{\rho_G}{\alpha_G}} g \cos\theta \frac{A}{\frac{dA_L}{dh_L}}}}, \tag{2.2}$$

where θ is the pipeline inclination angle with the horizontal direction and C_V and C_{IV} are the critical wave velocity for the inviscid and viscous analysis, respectively. The variable ρ_k is the density, α_k represents the volume fraction of each phase k, liquid or gas, A is the cross-section area and h_L is the liquid height. According to Issa and Kempf (2003) if Eq. (2.1) is not satisfied (right-hand side, RHS, greater than LHS, left-hand side) for the IKH analysis, the model loses hyperbolicty. If Eq. (2.1) is satisfied for the VKH analysis (LHS lower than RHS) the flow is stable and the stratified flow exists in the pipe. On the other hand, if Eq. (2.1) is not satisfied, (LHS greater than RHS) for the VKH analysis, the flow is unstable and the transition from stratified to intermittent flow occurs.

The slug flow can also be formed due to the pipeline inclination which may result in retardation followed by accumulation of liquid, for example in "V" section pipes. This is known as terrain-slugging and an extreme situation can occur when a cyclic production of long liquid slugs is formed, the so-called severe-slugging. According to Taitel *et al*. (1990) and Nieckele *et al.* (2013) the length of a severe slug can overtake the pipeline.

There are three classical approaches in intermittent flow modeling: the unit cell, the slug tracking and the slug capturing. The unit cell approach was thoroughly discussed in the works of Dukler and Hubbard (1975), Taitel and Barnea (1990), Zhang *et al.* (2003), Gonçalves *et al*. (2018) and Soedarmo *et al.* (2018). The unit cell approach assumes fully developed pipe flow and the intermittent two-phase flow is considered to be a succession of identical unit cells composed by a liquid slug and a gas bubble, treating the inherently transient slug pattern in a steady-state manner.

When more rigorous modeling approach is needed to incorporate details of the slug characteristics, the slug tracking and capturing techniques are recommended. In the slug

tracking approach, the slug is tracked in an individual way along the pipeline, in which the location of each slug front and bubble nose is calculated based on the conservation laws. This methodology follows a Lagrangian approach in which every slug and bubble are considered as distinct objects that are distributed along the line. This can result in an increase in computational efficiency if compared to the slug capturing. Some authors, such as Nydal and Barnejee (1996) and Rosa *et al*. (2015), carried out slug-tracking simulations for two-phase flows in a pipe. Within this technique it is necessary to set slug conditions at the beginning of the simulation or where the flow faces a different pipeline inclination. It means that the slugs are not generated automatically from the dynamic of the flow, or from the stratified pattern. Other authors used a hybrid version of a slug tracking, incorporating a slug capturing approach into a tracking model to generate the slug from the stratified flow through the growth of instabilities. (Renault, 2007; Kjeldby *et al*., 2013; Almeida *et al*., 2017). The commercial software OLGA (Schlumberger) also has an approach that is similar to the hybrid one, in which the Eulerian OLGA code and a slug tracking option are integrated.

Lastly, the slug capturing is based on a Eulerian frame and the slugs are formed due to the dynamics of the flow, in which the initiation and development of the intermittent pattern are a result of the solution of the governing equations instead of being determined by imposing specific relationships. Many authors developed numerical algorithms based on the two-fluid model (TFM) that are able to capture the evolution of waves in the gas-liquid interface and the transition from one flow pattern to another.

2.5.2 Slug Capturing Approach Using the TFM

Issa and Kempf (2003) were particularly interested in investigating the capability of the two-fluid model in predicting the formation and development of the slug flow due to its importance in practical applications. In this work, the authors were able to verify that the model can simulate the natural growth of instabilities, which generated the slug flow and the intermittent behavior of this flow pattern. The stratified flow, slug flow and the transition were modeled with one-dimensional conservation equations of mass and momentum. Issa and Kempf (2003) assumed an isothermal flow, disregarding the energy equation(s), and the remaining equations were discretized on a staggered grid using a finite volume method where the upwind difference scheme was applied to the spatial derivatives and the Euler implicit scheme for the temporal integration. The authors used

an artificial strategy to avoid a singularity in the gas momentum in the slug body, in which the liquid holdup reaches unity, and the void fraction becomes zero. It is worth mentioning that the control of the gas velocity in the slug body is essential to obtain well-formed slugs. This strategy consisted of setting the gas velocity to zero in the slug body region. This work is considered an important initial point in the slug capturing simulation performed with the two-fluid model. It emphasized the capability of the one-dimensional two-fluid model in predicting the growth of instabilities at the gas-liquid interface that initiated the slug flow formation.

Subsequently, Bonizzi and Issa (2003) also performed studies on the transient one-dimensional two-fluid model to simulate slug flow regime using the slug capturing approach. However, the gas entrainment effect was added to the model. The objectives of this work were to implement and validate the numerical model to simulate the phenomenon of gas bubble entrainment in two-phase flow. The entrainment model was based on the solution of the continuity and momentum equations for the gas phase, mass and momentum equations for the gas-liquid mixture and the scalar transport equation for the determination of the gas bubble fraction in the slug body. The most important contribution of this work was the formulation and implementation of a model that accounts for the gas entrainment in the slug flow. The gas bubble velocity is calculated according to a relation that balances the pressure and drag forces on a steady motion bubble. According to the authors, the results obtained with the aerated slug flow were compared to experiments with good accuracy. The gas-entrainment effect was most felt in the case of a V-section pipeline, while the horizontal cases had marginal differences if compared to unaerated simulations.

Based on Issa and Kempf (2003), Ortega Malca (2004), also performed slug capturing simulations. In order to analyze the stability and the hyperbolicity of the 4E1P model, two different ways of writing the governing equations of the flow were considered: the conservative and the non-conservative forms. The non-conservative formulation was used to try to minimize the problems derived from the singularity present in the gas momentum equation when gas phase vanishes, and the liquid slug fulfills the entire section of the pipe. Moreover, different ways of discretization of the conservation equations and the velocity-pressure coupling were tested, such as PISO and PRIMER algorithms. With the results obtained, the author emphasized some weaknesses in the model such as the gas momentum equation issue in the slug body and the use of empirical correlations for the

calculation of the friction factors that could influence the results and sensibility of the model.

In the work of Nieckele *et al.* (2013), the authors also studied the onset and development of the slug flow in a horizontal pipe solving the transient one-dimensional two-fluid model. The set of equations is comprised by two mass and momentum equations, one for each phase, and neglected the energy equation(s) under the hypothesis of isothermal flow. The conservation equations were discretized with the finite volume method where the convective terms were solved with the upwind approximation while the temporal integration was solved with the fully implicit Euler scheme. It is worth mentioning that the authors followed Issa and Kempf's (2003) recommendation, setting the gas phase velocity to zero when that phase vanishes. In addition, a statistical analysis was performed in order to help the interpretation of the results, by using probability density functions (PDF) of the experimental and numerical data, confirming, once again, the capability of the model in predicting the slug flow.

Ansari and Daramizadeh (2012) presented a numerical strategy for modeling the dynamics and the transient behavior of the slug initialization and development in horizontal pipes. In this study, the authors used the hyperbolic five-equation two-fluid model, the 5E2P. This model has two mass and two momentum equations, one for each phase, and one equation for the evolution of the void fraction. In the referred work, the numerical method AUSMDV in association with a MUSCL-HANCOCK reconstruction was used, achieving a second order space accuracy. The authors run numerical tests for benchmark cases as validation of the code, such as shock tube and water faucet problems, showing that the numerical model behaved well in the presence of discontinuities. Regarding the slug flow simulations, the results were compared to experiments performed with a rectangular cross-section and presented good agreement revealing physical characteristics of the slug flow regime. Even though the strategy to avoid singularity in the gas momentum equation was not mentioned, this work was important to show that the numerical methodology used is capable to predict the physics of different slug flow cases with good accuracy, even without requiring the solution of the associated Riemann problem or any previous knowledge of the eigenstructure of the model.

Another work that conducted slug capturing numerical simulations was Ferrari *et al.* (2017), also using the 5E2P model. A finite volume discretization of the hyperbolic equations and the use of the appropriate closure relations resulted in a numerical code developed to simulate two-phase air-water flows in pipelines. The system of equations

was solved explicitly using a finite volume method based on the approximate Riemann solver of Roe. This work adopted similar procedure as Issa and Kempf (2003) when the liquid volume fraction grows and tends to unity and, therefore, the gas volume fraction becomes zero, avoiding the solution of the gas momentum equation. However, differently from Issa and Kempf (2003), Ferrari *et al.* (2017) did not arbitrarily set the gas velocity to zero, stating that the abrupt modification of the gas velocity value introduces numerical oscillations. Thus, they defined a function that gradually approaches the gas velocity to zero in regions where the gas volume fraction falls in a certain range. The results obtained were divided into two parts: validation of the code and numerical method's robustness through benchmark problems and the slug capturing simulation itself. In the first part, the authors used the water faucet, the large relative velocity shock tube, the separation and the oscillating manometer problems. All of them presented good results when compared to the respective analytical solutions or reference results in the literature. For the slug capturing simulations, the code was successfully used to simulate the slug growth and development from the stratified flow in a horizontal pipeline and presented a grid independence when a grid refinement study was conducted. The work was able to show that the two-pressure model, the 5E2P, is a good option to simulate the slug flow without being concerned about the hyperbolicity of the model.

Recently, Ferrari *et al.* (2019) extended the previous work, Ferrari *et al.* (2017), that had been tested only for air-water flows in horizontal pipes. In the most recent work, the same numerical was adopted and validated for unconventional scenarios. First, they tested the slug capturing technique with the pair air and high viscosity oil and then, air and non-Newtonian fluids. In addition, different complex geometries were also studied. This work reinforced the capability of this numerical model to simulate the intermittent flow, not only for air-water flows, but also, for unconventional scenarios that are present in the daily activities of the oil and gas industries.

The present work contributes to the area of two-fluid-model by offering two mathematical models, the 5E2P and the 7E2P, in association with different numerical methods, the approximate Riemann solver of Roe and AUSM-type methods, to perform slug capturing simulations. Moreover, different strategies to avoid the singularity in the gas momentum equation are implemented, such as instantaneous velocity relaxation and a separate closure equation to model the gas phase in the slug body. This work also presents a more complete study, encompassing various slug flow scenarios that includes low and high viscosity fluids, as well as, horizontal and up to 30° of pipeline inclination.

3. Mathematical Model

In this chapter, the governing equations of the gas-liquid two-fluid models used to simulate the intermittent flow are presented, as well as the closure relations of the proposed models.

3.1 Hypotheses for the Two-Fluid Model (TFM)

The one-dimensional two-phase flow formulation adopted in this work is subject to some simplifications to better represent the physics of the flow, in addition to the assumptions that are intrinsic to the TFM itself. These hypotheses are described as follows:

- the cross-section area of the pipeline is constant;
- there is no mass transfer between the phases, nor chemical reaction is considered;
- the molecular and turbulent diffusive viscous effects in the axial direction are neglected;
- fluids properties, such as viscosities, are considered as constant;
- an isothermal flow is assumed, which means that the energy equation(s) is(are) neglected.

3.2 Two-Phase Flow Governing Equations

In the present work, two different approaches of the TFM, that represent two ways of writing the governing equations, are used. The first one is the 5E2P model and the second, is the herein called 7E2P. The 5E2P model, as mentioned in Chapter 2, is comprised of two mass and two momentum equations, one for each phase, and one equation for the evolution of the void fraction. The new model, the 7E2P, is proposed in this work as an extension of the 5E2P that encompasses the presence of dispersed bubbles and droplets phases in the formulation, adding more physics to the problem.

It is well known that the two-fluid model has some limitations regarding the disappearance of one of the phases during the development of the flow, for instance, when the liquid slug is formed, and the gas phase vanishes. When this happens, the void fraction becomes zero in the slug body region, creating a singularity in the gas momentum

equation. Thus, it is necessary to guarantee that the phase volume fractions keep their values greater than zero and lower than one, which makes the problem artificially controlled. The 7E2P model was first idealized in this work as an attempt to enrich the physics in the problem and avoid this artificial control, by keeping the concentration of bubbles and droplets sufficiently small to automatically guarantee that the liquid and gas phases would not cease to exist, even if it is coexisting in another phase. In other words, the inclusion of bubbles in the liquid phase and droplets in the gas phase would eliminate the occurrence of the singularity. However, even with a better physical modeling, there is no mathematical guarantee that these extra equations will be enough to produce values of the liquid and gas volume fractions within the correct range during the numerical calculation.

In this context, bubbles are dispersed in the liquid phase and droplets are dispersed in the gas phase for the 7E2P model. Both ways of representing the flow, with the 5E2P or the 7E2P, comprise, a priori, different pressures for the main phases and strictly hyperbolic mathematical models. One of the main concerns in using the two-fluid model is related to the loss of hyperbolicity and, consequently, an ill-posed model that do not represent the flow correctly. As already mentioned, the 4E1P model, comprised of two mass and two momentum equations, one for each phase that share the same pressure, is conditionally hyperbolic. Tests performed in the present work with the 4E1P model for slug capturing simulations returned complex eigenvalues, leading to a non-hyperbolic scenario. That was the main reason for not using this model. The 5E2P and the 7E2P models do not have this problem, since they are unconditionally hyperbolic with analytical eigenvalues that are always real.

3.2.1 5E2P Model

The 5E2P model is composed of the partial differential conservation equations listed below.

- Evolution of the gas volume fraction

$$\frac{\partial}{\partial t}(\alpha_G) + u_I \frac{\partial}{\partial x}(\alpha_G) = r_P(p_G - p_L). \tag{3.1}$$

- Equations of conservation of mass for the gas and liquid phases

$$\frac{\partial}{\partial t}(\rho_G \alpha_G) + \frac{\partial}{\partial x}(\rho_G \alpha_G u_G) = 0, \tag{3.2}$$

$$\frac{\partial}{\partial t}(\rho_L \alpha_L) + \frac{\partial}{\partial x}(\rho_L \alpha_L u_L) = 0. \tag{3.3}$$

In the above equations, α_k is the volume fraction, u_k is the velocity, ρ_k is the fluid density of each phase *k*, where *k* can assume *G* or *L*, related to the phase gas or liquid, respectively. The variable u_I stands for the interfacial velocity, which corresponds to the velocity of the center of mass of the two-fluid mixture. In Eq. (3.1), r_P is the relaxation parameter associated to the time needed for the phases to achieve the local thermodynamic equilibrium, and consequently, the same pressure value.

- Equations of conservation of momentum for the gas and liquid phases

$$\frac{\partial(\rho_G \alpha_G u_G)}{\partial t} + \frac{\partial(\rho_G \alpha_G u_G^2 + \alpha_G p_G)}{\partial x} = \left(p_G - \Delta p_{I,G}\right)\frac{\partial \alpha_G}{\partial x} + B_{fG} + T_I + T_{Gw}, \tag{3.4}$$

$$\frac{\partial(\rho_L \alpha_L u_L)}{\partial t} + \frac{\partial(\rho_L \alpha_L u_L^2 + \alpha_L p_L)}{\partial x} = (p_L - \Delta p_{I,L})\frac{\partial \alpha_L}{\partial x} + B_{fL} - T_I + T_{Lw}, \tag{3.5}$$

where p_k is the fluid pressure, B_{fk} stands for the body forces, T_I is the interfacial drag force per unit volume and T_{kw} is the drag force between the fluid and the wall per unit volume, for each phase *k*. The term $\Delta p_{I,k}$ is the pressure correction term. All these terms are detailed in the closure relation's section in this chapter.

The liquid volume fraction, α_L, and the gas volume fraction, α_G, also known as the holdup and the void fraction, respectively, are defined as the ratio of the volume occupied by each phase to the total cylindrical volume of fluid taken as a reference. However, for long pipelines, a common approach is to integrate the three-dimensional equations of motion over a cross-section of the pipe to obtain a suitable one-dimensional two-fluid model that is comprised of an area-averaged set of governing equations (Ishii and Hibiki, 2006). Therefore, the variables become averaged quantities based on the cross-section area of the pipe, *A*, and the volume fractions reduce to a ratio of areas, according to

$$\alpha_L \equiv \frac{A_L}{A_L + A_G}, \tag{3.6}$$

$$\alpha_G \equiv \frac{A_G}{A_L + A_G}, \tag{3.7}$$

where A_k is the area occupied by the phase *k*, that can be interpreted as *L*, for the liquid phase, or *G*, for the gas phase. The volume fractions are also subject to the compatibility condition of

$$\alpha_L + \alpha_G = 1. \tag{3.8}$$

3.2.2 7E2P Model

The 7E2P model is composed of the system of partial differential conservation equations as follows.

- Evolution of the gas and droplets volume fractions

$$\frac{\partial}{\partial t}(\alpha_G + \alpha_D) + u_I \frac{\partial}{\partial x}(\alpha_G + \alpha_D) = r_P(p_G - p_L). \tag{3.9}$$

- Equations of conservation of mass for the gas, liquid, droplets, and bubbles

$$\frac{\partial}{\partial t}(\rho_G \alpha_G) + \frac{\partial}{\partial x}(\rho_G \alpha_G u_G) = 0, \tag{3.10}$$

$$\frac{\partial}{\partial t}(\rho_L \alpha_L) + \frac{\partial}{\partial x}(\rho_L \alpha_L u_L) = 0, \tag{3.11}$$

$$\frac{\partial}{\partial t}(\rho_D \alpha_D) + \frac{\partial}{\partial x}(\rho_D \alpha_D u_D) = 0, \tag{3.12}$$

$$\frac{\partial}{\partial t}(\rho_B \alpha_B) + \frac{\partial}{\partial x}(\rho_B \alpha_B u_B) = 0. \tag{3.13}$$

In the above equations, α_k is the volume fraction, u_k is the velocity, ρ_k is the fluid density of each phase *k*, where *k* can assume the references *G*, *L*, *D* or *B*, relating to the

phase gas, liquid, droplets, or bubbles, respectively. In addition, the droplets density is equal to the liquid phase and the bubbles density is the same as the gas phase. Since the droplets phase is immersed in the gas phase, they share the same pressure and velocity, *i.e.*, $u_D = u_G$, while the liquid and bubbles share the same pressure and velocity as well, *i.e.*, $u_B = u_L$.

- Equations of conservation of momentum for the mixture gas and droplets phases, and for the mixture liquid and bubbles phases

$$\frac{\partial[(\rho_G\alpha_G + \rho_D\alpha_D)u_G]}{\partial t} + \frac{\partial[(\rho_G\alpha_G + \rho_D\alpha_D)u_G^2 + (\alpha_G+\alpha_D)p_G]}{\partial x} = \left(p_G - \Delta p_{I,G}\right)\frac{\partial(\alpha_G + \alpha_D)}{\partial x} + B_{fG} + T_I + T_{Gw}\,, \tag{3.14}$$

$$\frac{\partial[(\rho_L\alpha_L + \rho_B\alpha_B)u_L]}{\partial t} + \frac{\partial[(\rho_L\alpha_L + \rho_B\alpha_B)u_L^2 + (\alpha_L+\alpha_B)p_L]}{\partial x} = \left(p_L - \Delta p_{I,L}\right)\frac{\partial(\alpha_L + \alpha_B)}{\partial x} + B_{fL} - T_I + T_{Lw}. \tag{3.15}$$

For the 7E2P model, the volume fractions are defined as

$$\alpha_L \equiv \frac{A_L}{A_L + A_G + A_D + A_B}, \tag{3.16}$$

$$\alpha_G \equiv \frac{A_G}{A_L + A_G + A_D + A_B}, \tag{3.17}$$

$$\alpha_D \equiv \frac{A_D}{A_L + A_G + A_D + A_B}, \tag{3.18}$$

$$\alpha_B \equiv \frac{A_B}{A_L + A_G + A_D + A_B}, \tag{3.19}$$

where A_k is the area occupied by the phase *k*, that can be interpreted as *L*, for the liquid phase, *G*, for the gas phase, *D*, for the droplets phase or *B* for the bubbles phase. The volume fractions are also subject to the compatibility condition of

$$\alpha_L + \alpha_G + \alpha_D + \alpha_B = 1. \tag{3.20}$$

3.3 Solution Procedure of the Models

To solve the 5E2P and 7E2P models it necessary to consider the source terms related to the pressure relaxation in Eqs. (3.1) and (3.9), which will lead to a two-step solution through an intermediate step of calculation.

The system of equations considers the phases as compressible, admitting different pressure values for each phase. In a one-dimensional formulation, it may be a problem, since a wave can propagate in each phase with different velocities and, consequently, distinct pressures. However, both fluids cannot sustain those pressure differences, leading to an equilibrium pressure in short time intervals. Since the models do not consider this process, a correction term must be added to recover the relaxation process.

The most common procedure is to impose an infinity pressure relaxation coefficient, $r_P \to \infty$, referred in the literature as instantaneous pressure relaxation, as stated by Saurel and Abgrall (1999) and Munkejord (2010), since its value is known to be large for small relaxation time scales, but it has not been physically or experimentally determined.

In this intermediate step of calculation, the first part consists of solving the system of hyperbolic partial differential equations, as described Eqs. (3.1) to (3.5) and Eqs. (3.9) to (3.15) using the pressure relaxation coefficient equal to zero. The solution of this hyperbolic part requires an appropriate numerical method that is discussed in the next chapter. Using as initial values the results already obtained from the hyperbolic solution, the second step is to solve the following ordinary differential equations:

- For the 5E2P model:

$$\frac{\partial}{\partial t}(\alpha_G) = r_P(p_G - p_L), \tag{3.21}$$

$$\frac{\partial}{\partial t}(\rho_G \alpha_G) = 0, \tag{3.22}$$

$$\frac{\partial}{\partial t}(\rho_L \alpha_L) = 0, \tag{3.23}$$

$$\frac{\partial(\rho_G \alpha_G u_G)}{\partial t} = 0, \tag{3.24}$$

$$\frac{\partial(\rho_L \alpha_L u_L)}{\partial t} = 0. \tag{3.25}$$

- For the 7E2P model:

$$\frac{\partial}{\partial t}(\alpha_G + \alpha_D) = r_P(p_G - p_L), \tag{3.26}$$

$$\frac{\partial}{\partial t}(\rho_G \alpha_G) = 0, \tag{3.27}$$

$$\frac{\partial}{\partial t}(\rho_L \alpha_L) = 0, \tag{3.28}$$

$$\frac{\partial}{\partial t}(\rho_D \alpha_D) = 0, \tag{3.29}$$

$$\frac{\partial}{\partial t}(\rho_B \alpha_B) = 0, \tag{3.30}$$

$$\frac{\partial[(\rho_G \alpha_G + \rho_D \alpha_D) u_G]}{\partial t} = 0, \tag{3.31}$$

$$\frac{\partial[(\rho_L \alpha_L + \rho_B \alpha_B) u_L]}{\partial t} = 0. \tag{3.32}$$

3.3.1 Instantaneous Pressure Relaxation for the 5E2P Model

In this procedure, described in Munkejord (2005) and based on the work of Saurel and Abgrall (1999), the parameter r_P is equal to infinity to guarantee the instantaneous pressure equilibrium between the phases at each time step. It is more efficient to solve the problem analytically than solving the system Eqs. (3.21) to (3.25). Thus, a second-order equation can be used to modify the pressure value of the phases and keep the terms $\rho_k \alpha_k$ and $\rho_k \alpha_k u_k$ constant during the relaxation step. This second-order equation is only applicable when linear equations of state are used, such as the ones adopted in this work detailed as follows

$$p_k = c_k^2(\rho_k - \rho_k^0), \tag{3.33}$$

where the reference density, ρ_k^0, and the speed of sound, c_k, are specific constants of each fluid for a given thermodynamic state with constant temperature.

In the relaxation procedure, both pressures are equalized

$$p = c_G^2(\rho_G - \rho_G^0) \equiv c_L^2(\rho_L - \rho_L^0). \tag{3.34}$$

Calculating the square of the pressure and using Eq.(3.8) ,

$$p^2 = c_G^2 c_L^2(\rho_G - \rho_G^0)(\rho_L - \rho_L^0)(\alpha_G + \alpha_L). \tag{3.35}$$

After some mathematical manipulation, the second order equation is obtained

$$\psi_1 p^2 + \psi_2 p + \psi_3 = 0, \tag{3.36}$$

where, $\psi_1 = 1$, $\psi_2 = c_G^2(\rho_G^0 - \alpha_G\rho_G) + c_L^2(\rho_L^0 - \alpha_L\rho_L)$, $\psi_3 = c_G^2 c_L^2(\rho_G^0\rho_L^0 - \alpha_G\rho_G\rho_L^0 - \alpha_L\rho_L\rho_G^0)$.

The objective is to obtain the positive root of Eq. (3.36) given by

$$p = \frac{-\psi_2 + \sqrt{\psi_2^2 - 4\psi_1\psi_3}}{2\psi_1}. \tag{3.37}$$

After the computation of the relaxed pressure, all densities are recalculated using the equation of state, Eq. (3.33), as well as the new volume fractions that are obtained to guarantee that the products $\rho_k\alpha_k$ and $\rho_k\alpha_k u_k$ keep a constant value from the hyperbolic step. Another way to derive the second-order equation is to modify the gas volume fraction, also maintaining the $\rho_k\alpha_k$ and $\rho_k\alpha_k u_k$ unmodified, as suggested by Munkejord (2010) and Ferrari *et al.* (2017).

3.3.2 Instantaneous Pressure Relaxation for the 7E2P Model

For the 7E2P model, a similar procedure is performed to obtain the corresponding second-order equation and avoid numerically expensive method to solve the system given by Eqs. (3.26) to (3.32).

$$p = c_G^2(\rho_G - \rho_G^0) \equiv c_L^2(\rho_L - \rho_L^0). \tag{3.38}$$

Calculating the square of the pressure and using Eq.(3.8),

$$p^2 = c_G^2 c_L^2(\rho_G - \rho_G^0)(\rho_L - \rho_L^0)(\alpha_G + \alpha_L + \alpha_D + \alpha_B). \tag{3.39}$$

The second-order equation is obtained

$$\psi_1 p^2 + \psi_2 p + \psi_3 = 0 \tag{3.40}$$

where, $\psi_1 = 1$, $\psi_2 = c_G^2[\rho_G^0 - (\alpha_G + \alpha_B)\rho_G] + c_L^2[\rho_L^0 - (\alpha_L + \alpha_D)\rho_L]$, $\psi_3 = c_G^2 c_L^2[\rho_G^0\rho_L^0 - (\alpha_G + \alpha_B)\rho_G\rho_L^0 - (\alpha_L + \alpha_D)\rho_L\rho_G^0]$.

The positive root of Eq. (3.40) is determined by

$$p = \frac{-\psi_2 + \sqrt{\psi_2^2 - 4\psi_1\psi_3}}{2\psi_1}. \tag{3.41}$$

As for the 5E2P, after the calculation of the relaxed pressure, all densities and volume fractions are recalculated in order to guarantee that the products $\rho_k\alpha_k$ and $\rho_k\alpha_k u_k$ keep a constant value from the hyperbolic step.

3.4 Closure Relations

In this section, the relations that close the above detailed system of equations for both models are presented.

3.4.1 Pressure Term in Momentum Equations

For the pressure correction term that appear in the momentum equations, the Bestion relation, described in Bestion (1990), is used, which is written for both mathematical models as

$$\Delta p_{I,k} \equiv p_k - p_{I,k} = \delta \frac{\alpha_G \alpha_L \rho_G \rho_L}{\alpha_G \rho_L + \alpha_L \rho_G} (u_G - u_L)^2. \tag{3.42}$$

This pressure correction term is commonly adopted in the literature, such as Munkejord (2010) and Freitas (2016). The parameter δ is dimensionless and, according to work of Evje and Flatten (2003), it is equal to $\delta = 1.2$.

3.4.2 Interfacial Velocity Term

Saurel and Abgrall (1999) proposed an estimation of the interfacial velocity, present in Eqs. (3.1) and (3.9), as a relation associated with the velocity of the center of mass

$$u_I = \frac{\Sigma \alpha_k \rho_k u_k}{\Sigma \alpha_k \rho_k}. \tag{3.43}$$

3.4.3 Body Force Term

The body forces terms account for the gravity effect and can be expressed as

$$B_{fk} = -\rho_k \alpha_k g \sin\theta, \tag{3.44}$$

where g is the gravity acceleration and θ is the inclination angle with the horizontal direction.

3.4.4 Friction Relations

The friction terms that appear in the momentum equations are calculated from the following relations

$$T_{kw} = -\frac{\tau_k S_k}{A}, \text{where}, \tau_k = \frac{1}{2} f_k \rho_k u_k |u_k|, \tag{3.45}$$

$$T_I = \frac{\tau_I S_I}{A}, \text{where}, \tau_I = \frac{1}{2} f_I \rho_G (u_G - u_L)|u_G - u_L|. \tag{3.46}$$

In Eq. (3.45), τ_k is the friction stress at the wall and f_k is the friction factor of each phase *k*. In Eq. (3.46), the variable τ_I is the friction stress at the interface and f_I is the friction factor at the interface. In order to determine which friction correlations suits better in the prediction of slug initiation and development, Issa and Kempf (2003) compared several correlations with experiments. This study is taken as reference and the same correlations adopted by Issa and Kempf (2003), are used.

For the gas friction at the wall, the Taitel and Dukler's (1976) correlation is implemented for turbulent flow and the Hagen-Poiseulle for laminar flow

$$f_G = \begin{cases} \dfrac{16}{\mathrm{Re}_G}, \text{if } \mathrm{Re}_G \leq 2100 \\ 0.046(\mathrm{Re}_G)^{-0.2}, \text{otherwise} \end{cases}, \tag{3.47}$$

where Re_G is the Reynolds number for the gas phase, defined as

$$\mathrm{Re}_G = \frac{\rho_G D_{h_G} |u_G|}{\mu_G}, \tag{3.48}$$

where μ_G is the gas viscosity and D_{h_G} is the hydraulic diameter related to the gas phase. For the liquid friction with the wall, the Spedding and Hand (1997) correlation is used

$$f_L = \begin{cases} \dfrac{24}{\mathrm{Re}_L}, \text{if } \mathrm{Re}_L \leq 2100 \\ 0.0262(\alpha_L \mathrm{Re}_{sL})^{-0.139}, \text{otherwise} \end{cases}, \tag{3.49}$$

where Re_L and Re_{sL} are the Reynolds number for the liquid phase related to the liquid velocity and to the superficial liquid velocity, respectively. These Reynolds number are defined as

$$\mathrm{Re}_L = \frac{\rho_L D_{h_L} |u_L|}{\mu_L}, \tag{3.50}$$

$$\mathrm{Re}_{sL} = \frac{\rho_L D |u_{sL}|}{\mu_L}. \tag{3.51}$$

The variable μ_L is the liquid viscosity, D is the pipeline diameter and D_{h_L} is the hydraulic diameter related to the liquid phase.

For the interfacial friction, the Taitel and Dukler (1976) relation is applied, which was already detailed in Eq. (3.47). However, the Reynolds number that is used to calculate the interfacial friction is the interfacial Reynolds number defined at the interface

$$\mathrm{Re}_I = \frac{\rho_G D_{h_G} |u_G - u_L|}{\mu_G}. \tag{3.52}$$

3.4.5 Geometric Relations

Some geometric relations are necessary to complement the mathematical models. The hydraulic diameter of each phase is calculated as

$$D_{hG} = 4\frac{A_G}{S_G + S_I}, \tag{3.53}$$

$$D_{hL} = 4\frac{A_L}{S_L}. \tag{3.54}$$

The variables A_G and A_L are the cross-section areas of the gas and liquid phases, respectively, given by

$$A_G = \alpha_G A, \tag{3.55}$$

$$A_L = \alpha_L A. \tag{3.56}$$

The wetted perimeters of each phase, S_G and S_L, are expressed as

$$S_L = D\left[\pi - \cos^{-1}\left(2\frac{h_L}{D} - 1\right)\right], \tag{3.57}$$

$$S_G = \pi D - S_L. \tag{3.58}$$

where h_L is the liquid height in the cross section of the pipe, and the wetted perimeter, S_I, is calculated as

$$S_I = D\sqrt{1 - \left(2\frac{h_L}{D} - 1\right)^2}. \tag{3.59}$$

The last equation that must be presented is the relation between the liquid volume fraction with the liquid height. It can be written as

$$\frac{dh_L}{d\alpha_L} = \frac{\pi D}{4}\frac{\sqrt{1-\varsigma^2}}{1-\varsigma^2}, \tag{3.60}$$

and

$$\alpha_L = \frac{1}{\pi}\left\{\pi - \cos^{-1}[\varsigma] + \varsigma\sqrt{(1-\varsigma^2)}\right\}, \tag{3.61}$$

where ς is defined as

$$\varsigma \equiv \frac{2h_L}{D} - 1. \tag{3.62}$$

3.4.6 Hyperbolicity Analysis

The hyperbolicity analysis of the two-fluid model plays an important role when choosing the ideal mathematical model to be used in a numerical simulation. The mathematical models are represented by the governing equations, that are, in general, non-linear hyperbolic partial differential equations. With combination of distinct flow

parameters, the models might turn to be ill-posed, resulting in numerical instabilities and non-physical results. For carrying out the hyperbolicity analysis, the characteristic polynomial equations for each model are accessed in this section. To obtain them, the two sets of equations given by Eqs. (3.1) to (3.5) and Eqs. (3.9) to (3.15) are written in the following form,

$$\mathbf{M_1}(\mathbf{W})\frac{\partial \mathbf{W}}{\partial t} + \mathbf{M_2}(\mathbf{W})\frac{\partial \mathbf{W}}{\partial x} = \mathbf{S}(\mathbf{W}), \tag{3.63}$$

where $\mathbf{M_1}$ and $\mathbf{M_2}$ are matrices that are expressed in terms of the primitive variables vector $\mathbf{W}$. The polynomial is obtained through the following expression

$$P(\lambda) \equiv \det(\mathbf{M_2} - \lambda\mathbf{M_1}) = 0. \tag{3.64}$$

The roots of Eq. (3.64) are the eigenvalues of the system of PDE's. Whenever the eigenvalues are real and their eigenvectors are linearly independent, the model is said to be hyperbolic; a necessary condition for rendering the model well-posed. Another important point is the sign of eigenvalues, when computed at the pipe inlet (x=0) and outlet (x=L). They determine the proper number of boundary conditions to be prescribed to ensure a well-posed problem. The number of positive eigenvalues at (x=0) and the number of negative eigenvalues at (x=L) indicate the number of boundary conditions to be provided at the pipe inlet and outlet, respectively (Jeffrey, 1976; Figueredo *et al.*, 2017).

- Eigenvalues for the 5E2P Model

For the 5E2P model, as the fluid pressures are different, the primitive variables vector is written as $\mathbf{W} \equiv [\alpha_G \quad p_G \quad p_L \quad u_G \quad u_L]^T$ and the polynomial associated with det ($\mathbf{B} - \lambda\mathbf{A}$) is

$$P_{\mathrm{5E2P}}(\lambda) = \frac{\rho_G {\alpha_G}^2 \rho_L {\alpha_L}^2}{{c_G}^2 {c_L}^2}(u_I - \lambda)[(u_G - \lambda)^2 - {c_G}^2][(u_L - \lambda)^2 - {c_L}^2] = 0. \tag{3.65}$$

Differently from the 4E1P model, the roots of the 5E2P model are trivial and easily calculated analytically. The roots are: $\lambda_1 = u_I$; $\lambda_2 = u_G + c_G$; $\lambda_3 = u_G - c_G$; $\lambda_4 = u_L +$

c_L; $\lambda_5 = u_L - c_L$. Moreover, they are always real, and the set of the corresponding eigenvectors are linearly independent, making this model unconditionally hyperbolic, as long as $(u_k - u_I)^2 - {c_k}^2 \neq 0$ for $k \in \{L,\ G\}$ for the liquid and gas phases. If $(u_k - u_I)^2 - {c_k}^2 = 0$, the k-phase that obeys this condition should have $-\Delta p_{Ik} + \rho_k {c_k}^2 = 0$ to be hyperbolic, as reported in Ransom and Hicks (1984). In this work, we mainly consider low-speed flows, so this restriction is not a concern, and the model is, in fact, unconditionally hyperbolic. It is worth mentioning that the eigenvalues do not depend on the pressure correction term, what gives this model more flexibility for dealing with different pressure correction terms in the simulations.

- Eigenvalues for the 7E2P Model

For the 7E2P model, the primitive variables vector is written as $\mathbf{W} = [\alpha_G \quad \alpha_B \quad \alpha_D \quad p_G \quad p_L \quad u_G \quad u_L]^T$ and the polynomial associated with det $(\mathbf{B} - \lambda\mathbf{A})$ is

$$\begin{aligned} P_{7E2P}(\lambda) = \frac{1}{{c_G}^4 {c_L}^4}(u_I - \lambda)(u_G - \lambda)(u_L \\ - \lambda)[(u_G - \lambda)^2(\alpha_G\rho_G + \alpha_D\rho_D)({c_G}^2\alpha_D\rho_G + {c_L}^2\alpha_G\rho_D) \\ - {c_G}^2{c_L}^2\rho_G\rho_D\,(\alpha_G + \alpha_D)^2][(u_L - \lambda)^2(\alpha_L\rho_L \\ + \alpha_B\rho_B)({c_G}^2\alpha_L\rho_B + {c_L}^2\alpha_B\rho_L) \\ - {c_G}^2{c_L}^2\rho_L\rho_B\,(\alpha_L + \alpha_B)^2] = 0. \end{aligned} \tag{3.66}$$

The roots are: $\lambda_1 = u_I$; $\lambda_2 = u_G$; $\lambda_3 = u_L$; $\lambda_4 = u_G - c_{G/D}$; $\lambda_5 = u_G + c_{G/D}$; $\lambda_6 = u_L - c_{L/B}$; $\lambda_7 = u_L + c_{L/B}$.

The wave speeds of the gas/droplet and liquid/bubble mixtures, $c_{G/D}$ and $c_{L/B}$ are defined as

$$c_{G/D} = \sqrt{\frac{{c_G}^2{c_L}^2\rho_G\rho_D\,(\alpha_G + \alpha_D)^2}{(\alpha_G\rho_G + \alpha_D\rho_D)({c_G}^2\alpha_D\rho_G + {c_L}^2\alpha_G\rho_D)}}, \tag{3.67}$$

$$c_{L/B} = \sqrt{\frac{{c_G}^2{c_L}^2\rho_L\rho_B\,(\alpha_L + \alpha_B)^2}{(\alpha_L\rho_L + \alpha_B\rho_B)({c_G}^2\alpha_L\rho_B + {c_L}^2\alpha_B\rho_L)}}. \tag{3.68}$$

The eigenvalues are always real and analytically determined if the fluid densities and volume fractions are positive, which is a standard physical condition of the flow. A similar analysis can be performed for the 7E2P, as Ransom and Hicks (1984) did for the

5E2P and considering that in this work, we mainly consider low-speed flows, the model is unconditionally hyperbolic.

In order to better characterize how the pressure and bubble volume fraction influence the liquid/bubble mixture wave speed, $c_{L/B}$, Fig. 2 illustrates the behavior of the ratio of the liquid/bubble mixture wave speed to the liquid wave speed, $c_{L/B}/c_L$, as a function of the pressure, for several values of the bubble volume fraction, for the air-water mixture. In this analysis, the liquid volume fraction is constant and equal to 50%, the droplet volume fraction is 10^{-7}. The gas volume fraction is the complement of the sum of all the remaining volume fractions and for each curve in the plot the bubble volume fraction is varying from 10^{-8} to 10^{-3}.

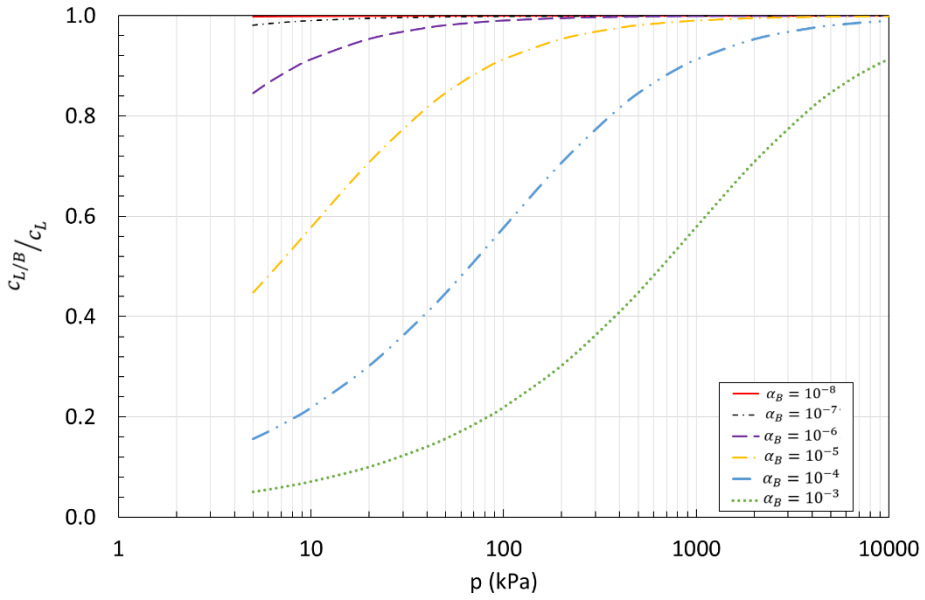

Figure 2: Dimensionless liquid-bubble mixture wave speed as a function of the pressure for several bubble volume fractions for the air-water mixture, with $\alpha_L = 0.5$ and $\alpha_D = 10^{-7}$.

The same analysis is performed for the gas-droplet mixture wave speed. In Fig. 3, the ratio $c_{G/D}/c_G$, that corresponds to the ratio of the gas/droplet mixture wave speed to the gas wave speed, is represented as a function of pressure for several droplet volume fraction for the air-water mixture. The gas volume fraction is constant and equal to 50%, the bubble volume fraction is 10^{-7} and the liquid volume fraction is the complement of all volume fractions. For each curve, the droplet volume fraction is changing from 10^{-8} to 10^{-3}.

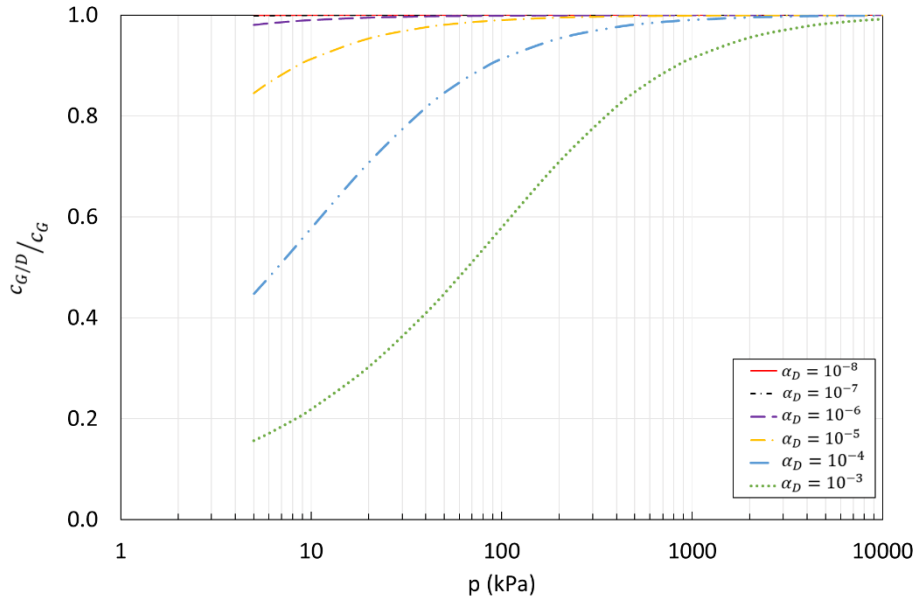

Figure 3: Dimensionless gas-droplet mixture wave speed as a function of the pressure for several droplet volume fractions for the air-water mixture, with $\alpha_G = 0.5$ and $\alpha_B = 10^{-7}$.

As it can be noticed, in both analyses, the mixture wave speeds in an air-water scenario are strongly influenced, in a non-linear way, by the pressure and by the bubble and droplet volume fractions. Considering the magnitude of the pressure and volume fractions, small variations in these variables cause significant changes in the mixture wave speeds. For higher pressures values and small volume fractions, bubbles or droplets, the mixture wave speeds approach the liquid or gas wave speed, respectively. However, for lower pressures and higher bubble or droplet volume factions in the mixture, the mixture wave speeds can achieve small values, distancing from the liquid or gas wave speed. For this reason, in the 7E2P model simulations, the bubble and droplet volume fractions considered as initial conditions are 10^{-7} to guarantee that the mixture wave speeds are as close as possible to the liquid or gas wave speeds, respectively.

3.4.7 Slug Body Modeling

The two-fluid model is subject to a singularity when one of the phases vanishes. In the slug flow, it happens when the liquid volume fraction tends to unity and the void fraction goes to zero. This phenomenon occurs even with the 7E2P model, where the gas

phase is present in the form of bubbles, and the void fraction may still approach zero asymptotically.

Physically, because there is no mass transfer between the phases, there is no mechanism that allows one phase to vanish. However, mathematically, there is nothing in the equations that prevent the volume fractions from being greater than one and less than zero during the numerical solution. During the numerical calculation, if the solution of the mathematical equations returns a holdup value greater than one or less than zero, the solution is non-physical, even if the simulation continues. Moreover, there is a necessity to control the gas velocity in the slug region to prevent it from reaching high values, which does not represent the real condition of the flow when it is filled with liquid. The gas velocity goes to high values in that region due to the throat that is formed between the liquid slug and the pipe wall when the pipe section is almost filled with liquid.

To avoid this mathematical issue, many authors in the literature, such as Issa and Kempf (2003) and Nieckele *et al.* (2013), consider that when the holdup approaches unity, within a certain range, the gas velocity is set to zero to avoid the solution of the gas momentum equation. This technique was implemented in this work, although more sophisticated solutions to deal with this issue were also tested and presented more physically consistent results.

In the slug body, the gas phase that is present has a void fraction in a range close to zero and can be interpreted as small bubbles. The velocity of these bubbles (gas phase) can be calculated in various forms.

Trying to model the phase appearance and disappearance, Paillère *et al*. (2003) bounded the velocity of the vanishing phase. They stated that from a physical point of view, this velocity tends to the velocity of the remaining phase and added a positive function to do that in a smooth way. In the case that the gas phase is the one that is vanishing, its velocity is calculated by

$$u_G = G(\alpha_G)u_G + [1 - G(\alpha_G)]u_L, \tag{3.69}$$

This form to bound the velocity of the vanishing phase is similar to a velocity relaxation, as studied by Munkejord (2005). The velocity relaxation is applied to consider no slip relation between the phases. The velocity relaxation term replaces the interfacial friction term and can be modeled analogously to the instantaneous pressure relaxation procedure. The instantaneous velocity relaxation procedure can be employed in the same

way as Saurel and Abgrall (1999), changing $\rho_k \alpha_k u_k$ while keeping $\sum \rho_k \alpha_k u_k$, $\rho_k \alpha_k$ and α_k constant, so that $u_G = u_L$ according to

$$u_G = u_L = \frac{\Sigma \alpha_k \rho_k u_{k0}}{\Sigma \alpha_k \rho_k}, \tag{3.70}$$

where the subscript 0 is related to the initial value given to the relaxation procedure.

Another approach to control the gas velocity in the slug body is by having a closure relation that calculates the gas velocity as a different phase, for example, bubbles. Assuming steady motion and considering the balance between pressure and drag forces, Bonizzi and Issa (2003) suggested the following equation for their gas entrainment model,

$$u_B = u_L - \sqrt{\frac{-4 d_B \left({}^{dp}/_{dx} \right)}{3 C_D \rho_L}}, \tag{3.71}$$

where the pressure term implies a negative pressure gradient and d_B is the bubble diameter that was assumed to be 1mm. The drag coefficient term, C_D, is calculated as

$$C_D = \frac{C_{DT}}{\sqrt{\alpha_L}}. \tag{3.72}$$

and

$$C_{DT} = max\left[\frac{24}{\mathrm{Re}_B} (1 + 0.15 \mathrm{Re}_B^{0.687}), \frac{8}{3} \frac{Eo}{Eo + 4} \right]. \tag{3.73}$$

The Reynolds, Re_B, and the Eötvös, Eo, numbers are given by

$$\mathrm{Re}_B = \frac{\rho_L d_B |u_L - u_B|}{\mu_L}, \tag{3.74}$$

$$Eo = \frac{g(\rho_L - \rho_G) d_B^2}{\sigma}, \tag{3.75}$$

where σ is the surface tension and g is the gravity acceleration.

An alternative is to calculate the gas velocity as the gas-bubble velocity in the slug, as presented in Shoham (2006), based on the drift velocity of the bubbles of Harmathy (1960).

$$u_G = c_0 u_m + 1.53 \left[\frac{g\sigma(\rho_L - \rho_G)}{{\rho_L}^2}\right]^{0.25} {\alpha_L}^{0.5} \sin\theta, \tag{3.76}$$

where, u_m is the mixture velocity and c_0 is the distribution coefficient that has the most probable value of $c_0 = 1.2$, and for horizontal and nearly horizontal flow, it is $c_0 = 1$.

4. Numerical Methods

Numerical simulation of two-phase flows is a problem of complex nature due to the non-linearity of the equations. Thus, the choice of the numerical method that will return accurate results for the solution of this problem is a crucial step that must be widely explored in the development of the numerical algorithm.

The evaluation, verification and validation of a numerical model are essential steps to ensure that the solutions generated are representative of the physics of the problem. In a general manner, there are no practical engineering problems of two-phase flow in pipelines that have a complete analytical solution. Nonetheless, there are widely used benchmark problems in the literature that have approximate analytical solutions that are obtained through assumptions or approximation based on well-known physical concepts.

Many works in the literature are focused on the numerical solution of these benchmark problems, such as the shock tube, the water faucet, the segregation problems, among others. These works serve as references for the selection of promising numerical techniques, as they point out advantages and disadvantages of each implemented methodology, such as their behavior close to discontinuities and sharp gradients, as well as the influence of diffusion and dispersion in the solution. Other works are focus on the verification and validation of their numerical models through comparison with experimental data (laboratory or field) or with software simulations that are widely used by the oil and gas industry.

4.1 Numerical Method Selection

Some literature works serve as a guide in the decision of the best numerical technique to be implemented. As a first example, in the work of Omgba-Essama (2004) several comparisons were made between centered numerical schemes, such as Lax-Friedrichs, Ritchmyer, FORCE, Flux-Corrected Transport (FCT), and some other techniques inspired in the characteristic's method, as Rusanov and TVD Lax-Friedrichs. The most notable characteristics of each methodology were observed through benchmark problems and the solution of the stratified flow in pipelines. In general, the FCT method was the one that presented the most accurate result for the tests performed by the authors, followed by TVD Lax-Friedrichs, Rusanov and FORCE methods. Moreover, the Lax-

Friedrichs method seemed to be the less accurate of all methods studied, presenting too much numerical diffusion. The Ritchmyer method, on the other hand, was too dispersive and presented oscillations near discontinuities, which do not provide confidence to the users for application in more complex problems, such as slug capturing. Further works with the FCT method also presented good results for the solution of two-phase flow problems, especially in the stratified flow pattern. Figueiredo *et al.* (2017) and Sondermann *et al.* (2019) compared the results with the commercial software OLGA for isothermal and non-isothermal stratified flow, respectively. Even though the FCT numerical method is robust and capable of dealing with the solution of hyperbolic partial differential equations, it was not able to generate the slug flow during the simulations tests that were performed herein. The FCT method presented intense diffusion that mitigated the growth of the waves and, consequently, the slug flow could not be generated in the pipeline during the numerical simulation. Other methods that were implemented during the development of this work are the TVD WAF (Total Variation Diminishing – Weighted Average Flux) and the approximate Riemann solver HLL (Harten, Lax and van Leer), according to Toro (1999). Both methods presented diffusive behavior, similar to the FCT, and could not generate the slug flow when tested for this type of flow conditions.

As an alternative to those methods, other types of numerical approaches were considered, taking as reference publications in the literature with a similar application scenario. In the work of Ferrari *et al.* (2017), the authors performed slug capturing numerical simulations, in which the mathematical model is solved by means of a high-resolution Roe solver (Roe, 1981) that consists of an approximate solution of the Riemann problem at the cell interface. The Roe method is accurate, specially near sharp gradients and discontinuities, which is a particularly good advantage in slug capturing simulations. The implementation of the method depends directly on the system of equations that is being solved. This method was also investigated by Munkejord (2007), that simulated benchmark problems, such as the shock tube and the water faucet, as a numerical validation, and to verify how the method behaves with different mathematical models.

In the work of Ansari and Daramizadeh (2012), the authors used another interesting numerical approach to simulate slug flow in pipelines. They used the AUSMDV method, which is a variation of the AUSM (Advection Upstream Splitting Method) that was initially presented by Liou and Steffen (1993). This method does not need any characteristic analysis of the system of equations, it has a low computational cost and a simpler numerical implementation, if compared to high-resolution methods, such as the

approximate Riemann solvers. Many authors studied this method more deeply, as Paillère *et al.* (2003), Evje and Flätten (2003). Other variations of the AUSM method can be implement, like the AUSM+ (Liou, 1996), AUSMV and AUSMD. The last two variations, AUSMV and AUSMD, are similar to a Flux Vector Splitting (FVS) and a Flux Difference Splitting (FDS), respectively. FVS methods tend to be more diffusive and simpler and the FDS, more complex and accurate. The AUSMDV method is a balance between these two methods (AUSMV and AUSMD), in which each of them is weighted to have an influence in the final solution. Although this means that the method has an adjustment/tunning parameter, which can be considered as loss of generality, it can also indicate greater control over the solution by highlighting the positive aspects of each of the methods involved. Loilier *et al.* (2005) and Coelho *et al.* (2010) used the AUSMDV in their simulations of benchmark problems to analyze the behavior of the method in those scenarios. The results confirmed that the AUSM-type methods are a great alternative if compared to the ones based on the Riemann solution. These AUSM-type methods are simple to implement and, at the same time, have excellent accuracy comparable to methods based on the solution of the Riemann problem. This fact is very encouraging, both in terms of simplicity and in terms of computational time.

Based on the literature review on numerical methods used to simulate the slug flow, the Roe and the AUSMDV methods are the ones that are implemented in this work. On the one hand, the Roe method gives the accuracy and the complex implementation of the approximate Riemann solver. On the other hand, the AUSMDV method shows the balance between the FVS and FDS methods with a simpler implementation and accurate results.

In the next sections, both methods are detailed separately. First, the AUSM-type methods based on the calculation of the intercell flux are described and, in the sequence, the Roe scheme, which has the Roe matrix solved by means of the determination of the Jacobian matrix.

4.2 AUSM-Type Methods

To obtain an approximate numerical solution of an initial and boundary value problem, the system of equations must be rewritten in a canonical form of the conservation law. In this form, **Q** is the conservative variables vector, **F** is the flux vector,

W is the primitive variables vector, **H** is the non-conservative matrix, **S** is the source term vector and **N** is the non-conservative vector.

As described in chapter 3 of this work, two different mathematical models are considered: the 5E2P (five equations and two pressures) and the 7E2P (seven equations and two pressures) models. They can be written in the canonical form as

$$\frac{\partial \mathbf{Q}}{\partial t} + \frac{\partial \mathbf{F}}{\partial x} = \mathbf{H}\frac{\partial \mathbf{N}}{\partial x} + \mathbf{S}, \tag{4.1}$$

where **Q, F, H, N S and W** are detailed differently for the two models:

- 5E2P model:

$$\mathbf{W} = \begin{bmatrix} \alpha_G \\ p_G \\ p_L \\ u_G \\ u_L \end{bmatrix}, \quad \mathbf{H} = \begin{bmatrix} u_I & 0 & 0 & 0 & 0 \\ 0 & 0 & 0 & 0 & 0 \\ 0 & 0 & 0 & 0 & 0 \\ 0 & 0 & 0 & \alpha_G & 0 \\ 0 & 0 & 0 & 0 & \alpha_L \end{bmatrix}, \mathbf{F} = \begin{bmatrix} 0 \\ \rho_G \alpha_G u_G \\ \rho_L \alpha_L u_L \\ \rho_G \alpha_G u_G^2 + \alpha_G \Delta p_{IG} \\ \rho_L \alpha_L u_L^2 + \alpha_L \Delta p_{IL} \end{bmatrix}, \tag{4.2}$$

$$\mathbf{N} = \begin{bmatrix} -\alpha_G \\ 0 \\ 0 \\ (\Delta p_{IG} - p_G) \\ (\Delta p_{IL} - p_L) \end{bmatrix}, \mathbf{Q} = \begin{bmatrix} \alpha_G \\ \rho_G \alpha_G \\ \rho_L \alpha_L \\ \rho_G \alpha_G u_G \\ \rho_L \alpha_L u_L \end{bmatrix}, \tag{4.3}$$

$$\mathbf{S} = \begin{bmatrix} r_p(p_G - p_L) \\ 0 \\ 0 \\ -\rho_G \alpha_G g \sin\beta - \dfrac{\tau_I S_I}{A_i} - \dfrac{\tau_G S_G}{A} \\ -\rho_L \alpha_L g \sin\beta + \dfrac{\tau_I S_I}{A_i} - \dfrac{\tau_L S_L}{A} \end{bmatrix}. \tag{4.4}$$

- 7E2P model:

$$\mathbf{W}=\begin{bmatrix}\alpha_G\\ \alpha_B\\ \alpha_D\\ p_G\\ p_L\\ u_G\\ u_L\end{bmatrix},\ \mathbf{H}=\begin{bmatrix}u_I & 0 & 0 & 0 & 0 & 0 & 0\\ 0 & 0 & 0 & 0 & 0 & 0 & 0\\ 0 & 0 & 0 & 0 & 0 & 0 & 0\\ 0 & 0 & 0 & \alpha_G+\alpha_D & 0 & 0 & 0\\ 0 & 0 & 0 & 0 & \alpha_L+\alpha_B & 0 & 0\\ 0 & 0 & 0 & 0 & 0 & 0 & 0\\ 0 & 0 & 0 & 0 & 0 & 0 & 0\end{bmatrix}, \tag{4.5}$$

$$\mathbf{F}=\begin{bmatrix}0\\ \rho_G\alpha_G u_G\\ \rho_L\alpha_L u_L\\ \rho_G\alpha_G u_G^2+\rho_L\alpha_D u_G^2+(\alpha_G+\alpha_D)\Delta p_{IG}\\ \rho_L\alpha_L u_L^2+\rho_G\alpha_B u_L^2+(\alpha_L+\alpha_B)\Delta p_{IL}\\ \rho_G\alpha_B u_L\\ \rho_L\alpha_D u_G\end{bmatrix},\ \mathbf{N}=\begin{bmatrix}-(\alpha_G+\alpha_D)\\ 0\\ 0\\ (\Delta p_{IG}-p_G)\\ (\Delta p_{IL}-p_L)\\ 0\\ 0\end{bmatrix}, \tag{4.6}$$

$$\mathbf{Q}=\begin{bmatrix}\alpha_G+\alpha_D\\ \rho_G\alpha_G\\ \rho_L\alpha_L\\ (\rho_G\alpha_G+\rho_L\alpha_D)u_G\\ (\rho_L\alpha_L+\rho_G\alpha_B)u_L\\ \rho_G\alpha_B\\ \rho_L\alpha_D\end{bmatrix},\mathbf{S}=\begin{bmatrix}r_p(p_G-p_L)\\ 0\\ 0\\ -\rho_G\alpha_G g\sin\beta-\dfrac{\tau_I S_I}{A_i}-\dfrac{\tau_G S_G}{A}\\ -\rho_L\alpha_L g\sin\beta+\dfrac{\tau_I S_I}{A_i}-\dfrac{\tau_L S_L}{A}\\ 0\\ 0\end{bmatrix}. \tag{4.7}$$

4.2.1 General Numerical Discretization

To discretize the 5E2P and 7E2P models, a uniform mesh of *N* computational cells along the pipe length, *L*, is considered. Each cell has a regular size Δx,

$$\Delta x \equiv x_{j+\frac{1}{2}}-x_{j-\frac{1}{2}}=\frac{L}{N} \tag{4.8}$$

where $x_{j-1/2}=(j-1)\Delta x$ and $x_{j+1/2}=j\Delta x$ are the left and right cell boundaries with $j=1,\ldots,N$. The cell center is located at the position $x_j=(j-\frac{1}{2})\Delta x$.

An explicit discretization of the numerical approximation is obtained to calculate the vector $\mathbf{Q}_j^{n+1}$, at the time instant $t^{n+1}=t^n+\Delta t$, through a general finite-difference form

$$\mathbf{Q}_j^{n+1} = \mathbf{Q}_j^n - \frac{\Delta t}{\Delta x}\left[\mathbf{F}^n_{j+\frac{1}{2}} - \mathbf{F}^n_{j-\frac{1}{2}}\right] + \Delta t\left(\mathbf{H}\frac{\partial \mathbf{N}}{\partial x}\right)_j^n + \Delta t\mathbf{S}_j^n \tag{4.9}$$

where $\mathbf{Q}_j^n$ is an approximation of $\mathbf{Q}$ at the position j and time instant t^n, Δt is the time step. The $\mathbf{F}^n_{j+1/2}$ and $\mathbf{F}^n_{j-1/2}$ terms account for the inter-cell flux vectors at $x_{j_{+1/2}}$ and $x_{j_{-1/2}}$, at time t^n.

For an explicit discretization, the CFL (Courant-Friedrichs-Lewy) condition must be considered in order to keep the numerical stability of the method. The time step, Δt, is calculated according to

$$\Delta t = \mathrm{CFL}\frac{\Delta x}{|\lambda|_{max}}, \tag{4.10}$$

where CFL is a positive number, less or equal to unity. The parameter $|\lambda|_{max}$ represents the largest eigenvalue of the flow domain in absolute value in each cell and each time step.

4.2.2 Discretization of the Flux Term

To calculate the flux term that appears in Eq. (4.9), numerical methods are required to obtain the left and right cell boundaries of the position *j*. For that, the AUSMDV method and consequently the AUSM-type methods (Advection Upstream Splitting Method) that compose the AUSMDV method, AUSMV and AUSMD, are detailed.

The AUSM method was first proposed by Liou and Steffen (1993) for single phase flow. Differently from the methods that employ approximate Riemann solvers, like the Roe method, the AUSM-type methods are considered as simple, because there is no need to obtain the Jacobian matrix, which adds considerable difficulty to the solution. In addition, the method aims to be accurate, robust and of low computational cost.

AUSM-type methods are considered as hybrid flux-splitting, *i.e.*, they present hybrid characteristics of two types of numerical schemes, FVS (flux vector splitting) and FDS (flux difference splitting). The main idea is to combine the efficiency of the FVS methods, whose flux is obtained through scalar calculations, with the accuracy of the FDS, whose flux is obtained by matrix calculations. FVS methods are easier to implement and more

efficient, but they are generally more diffusive than FDS methods, as confirmed by Evje and Flätten (2003). The flux term for AUSM-type numerical schemes is separated into convective flux term and pressure flux term, as given by

$$\mathbf{F}^{\text{AUSM}}_{j+\frac{1}{2}} = \mathbf{F}^{c}_{j+\frac{1}{2}} + \mathbf{F}^{p}_{j+\frac{1}{2}}. \tag{4.11}$$

For the 5E2P model

$$\mathbf{F}^{c} = \begin{bmatrix} 0 \\ \rho_G \alpha_G u_G \\ \rho_L \alpha_L u_L \\ \rho_G \alpha_G u_G^2 \\ \rho_L \alpha_L u_L^2 \end{bmatrix}, \mathbf{F}^{p} = \begin{bmatrix} 0 \\ 0 \\ 0 \\ \alpha_G \Delta p_{IG} \\ \alpha_L \Delta p_{IL} \end{bmatrix}. \tag{4.12}$$

And for the 7E2P model:

$$\mathbf{F}^{c} = \begin{bmatrix} 0 \\ \rho_G \alpha_G u_G \\ \rho_L \alpha_L u_L \\ \rho_G \alpha_G u_G^2 + \rho_L \alpha_D u_G^2 \\ \rho_L \alpha_L u_L^2 + \rho_G \alpha_B u_L^2 \\ \rho_G \alpha_B u_L \\ \rho_L \alpha_D u_G \end{bmatrix}, \mathbf{F}^{p} = \begin{bmatrix} 0 \\ 0 \\ 0 \\ (\alpha_G + \alpha_D)\Delta p_{IG} \\ (\alpha_L + \alpha_B)\Delta p_{IL} \\ 0 \\ 0 \end{bmatrix}. \tag{4.13}$$

In later work, Wada and Liou (1997), added some modifications to the original method, this time also for single phase flow, that inspired Evje and Flätten (2003) to improve the schemes known as AUSMV and AUSMD. The AUSMV method tends towards an FVS method, while the AUSMD tends towards an FDS. For both methods,

$$\tilde{V}^{\pm}(u_k, c, \chi^{L,R}) = \begin{cases} \chi^{L,R}\left[\pm\frac{1}{4c}(u_k \pm c)^2\right] + (1-\chi^{L,R})\frac{u_k \pm |u_k|}{2}, \text{if} |u_k| \le c \\ \frac{u_k \pm |u_k|}{2}, \text{otherwise,} \end{cases} \tag{4.14}$$

where

$$\chi^L = \frac{2(\rho/\alpha)^L}{(\rho/\alpha)^L + (\rho/\alpha)^R}, \qquad \chi^R = \frac{2(\rho/\alpha)^R}{(\rho/\alpha)^L + (\rho/\alpha)^R}. \tag{4.15}$$

The indexes *L* or *R* indicate the left and right cells, respectively. The subscript *k* represents the phase, gas, liquid, droplets, or bubbles, depending on the mathematical model that is considered. The parameter *c* in Eq. (4.14) is the speed of sound for the mixture that can be modeled in several ways. In this work, this term is calculated as an average of the speeds of sound of the gas and liquid phases in order to obtain a common speed of sound, as in the work of Kitamura and Liou (2012). Even though the choice of this term may allow the exact capturing of a stationary shock, as stated by Wada and Liou (1997), this study is not the focus of this work and it is not discussed here. The term u_k is the fluid velocity of the phase *k*.

For the calculation with the AUSMV, considering the components of the vector **Q** in Eq. (4.3) for the 5E2P model, the convective flux is defined as

$$\mathbf{F}^c_{j+\frac{1}{2}} = \begin{bmatrix} 0 \\ \mathbf{Q}_{2,j}\tilde{V}^+\left((u_G)_j, c_{j+\frac{1}{2}}, \chi^L_G\right) + \mathbf{Q}_{2,j+1}\tilde{V}^-\left((u_G)_{j+1}, c_{j+\frac{1}{2}}, \chi^R_G\right) \\ \mathbf{Q}_{3,j}\tilde{V}^+\left((u_L)_j, c_{j+\frac{1}{2}}, \chi^L_L\right) + \mathbf{Q}_{3,j+1}\tilde{V}^-\left((u_L)_{j+1}, c_{j+\frac{1}{2}}, \chi^R_L\right) \\ \mathbf{Q}_{4,j}\tilde{V}^+\left((u_G)_j, c_{j+\frac{1}{2}}, \chi^L_G\right) + \mathbf{Q}_{4,j+1}\tilde{V}^-\left((u_G)_{j+1}, c_{j+\frac{1}{2}}, \chi^R_G\right) \\ \mathbf{Q}_{5,j}\tilde{V}^+\left((u_L)_j, c_{j+\frac{1}{2}}, \chi^L_L\right) + \mathbf{Q}_{5,j+1}\tilde{V}^-\left((u_L)_{j+1}, c_{j+\frac{1}{2}}, \chi^R_L\right) \end{bmatrix}. \tag{4.16}$$

For the 7E2P model, considering the vector **Q** in Eq. (4.7) and defining the following terms to simplify the convective flux,

$$\begin{aligned} \mathbf{F}^c_{G,QML} \equiv\ & \mathbf{Q}_{2,j}(u_G)_j\tilde{V}^+\left((u_G)_j, c_{j+\frac{1}{2}}, \chi^L_G\right) \\ & + \mathbf{Q}_{2,j+1}(u_G)_{j+1}\tilde{V}^-\left((u_G)_{j+1}, c_{j+\frac{1}{2}}, \chi^R_G\right), \end{aligned} \tag{4.17}$$

$$\begin{aligned} \mathbf{F}^c_{L,QML} \equiv\ & \mathbf{Q}_{3,j}(u_L)_j\tilde{V}^+\left((u_L)_j, c_{j+\frac{1}{2}}, \chi^L_L\right) \\ & + \mathbf{Q}_{3,j+1}(u_L)_{j+1}\tilde{V}^-\left((u_L)_{j+1}, c_{j+\frac{1}{2}}, \chi^R_L\right), \end{aligned} \tag{4.18}$$

to obtain

$$\mathbf{F}^{c}_{j+\frac{1}{2}} = \begin{bmatrix} 0 \\ \mathbf{Q}_{2,j}\tilde{V}^{+}\left((u_G)_j, c_{j+\frac{1}{2}}, \chi^{L}_{G}\right) + \mathbf{Q}_{2,j+1}\tilde{V}^{-}\left((u_G)_{j+1}, c_{j+\frac{1}{2}}, \chi^{R}_{G}\right) \\ \mathbf{Q}_{3,j}\tilde{V}^{+}\left((u_L)_j, c_{j+\frac{1}{2}}, \chi^{L}_{L}\right) + \mathbf{Q}_{3,j+1}\tilde{V}^{-}\left((u_L)_{j+1}, c_{j+\frac{1}{2}}, \chi^{R}_{L}\right) \\ \mathbf{F}^{c}_{G,QML} + \mathbf{Q}_{7,j}(u_G)_j\tilde{V}^{+}\left((u_G)_j, c_{j+\frac{1}{2}}, \chi^{L}_{D}\right) + \mathbf{Q}_{7,j+1}(u_G)_{j+1}\tilde{V}^{-}\left((u_G)_{j+1}, c_{j+\frac{1}{2}}, \chi^{R}_{D}\right) \\ \mathbf{F}^{c}_{L,QML} + \mathbf{Q}_{6,j}(u_L)_j\tilde{V}^{+}\left((u_L)_j, c_{j+\frac{1}{2}}, \chi^{L}_{B}\right) + \mathbf{Q}_{6,j+1}(u_L)_{j+1}\tilde{V}^{-}\left((u_L)_{j+1}, c_{j+\frac{1}{2}}, \chi^{R}_{B}\right) \\ \mathbf{Q}_{6,j}\tilde{V}^{+}\left((u_L)_j, c_{j+\frac{1}{2}}, \chi^{L}_{B}\right) + \mathbf{Q}_{6,j+1}\tilde{V}^{-}\left((u_L)_{j+1}, c_{j+\frac{1}{2}}, \chi^{R}_{B}\right) \\ \mathbf{Q}_{7,j}\tilde{V}^{+}\left((u_G)_j, c_{j+\frac{1}{2}}, \chi^{L}_{D}\right) + \mathbf{Q}_{7,j+1}\tilde{V}^{-}\left((u_G)_{j+1}, c_{j+\frac{1}{2}}, \chi^{R}_{D}\right) \end{bmatrix}. \quad (4.19)$$

For the calculation with the AUSMD, also considering the components of the vector **Q** in Eq. (4.3) for the 5E2P model, the convective flux is defined as

$$\mathbf{F}^{c}_{j+\frac{1}{2}} = \begin{bmatrix} 0 \\ \mathbf{Q}_{2,j}\tilde{V}^{+}\left((u_G)_j, c_{j+\frac{1}{2}}, \chi^{L}_{G}\right) + \mathbf{Q}_{2,j+1}\tilde{V}^{-}\left((u_G)_{j+1}, c_{j+\frac{1}{2}}, \chi^{R}_{G}\right) \\ \mathbf{Q}_{3,j}\tilde{V}^{+}\left((u_L)_j, c_{j+\frac{1}{2}}, \chi^{L}_{L}\right) + \mathbf{Q}_{3,j+1}\tilde{V}^{-}\left((u_L)_{j+1}, c_{j+\frac{1}{2}}, \chi^{R}_{L}\right) \\ 0.5\left\{\left(\mathbf{F}^{c}_{j+1/2}\right)_2\left[(u_G)_j + (u_G)_{j+1}\right] - \left|\left(\mathbf{F}^{c}_{j+1/2}\right)_2\right|\left[(u_G)_{j+1} - (u_G)_j\right]\right\} \\ 0.5\left\{\left(\mathbf{F}^{c}_{j+1/2}\right)_3\left[(u_L)_j + (u_L)_{j+1}\right] - \left|\left(\mathbf{F}^{c}_{j+1/2}\right)_3\right|\left[(u_L)_{j+1} - (u_L)_j\right]\right\} \end{bmatrix}. \quad (4.20)$$

For the 7E2P model, considering the vector **Q** in Eq. (4.7),

$$\mathbf{F}^{c}_{j+\frac{1}{2}} = \begin{bmatrix} 0 \\ \mathbf{Q}_{2,j}\tilde{V}^{+}\left((u_G)_j, c_{j+\frac{1}{2}}, \chi^{L}_{G}\right) + \mathbf{Q}_{2,j+1}\tilde{V}^{-}\left((u_G)_{j+1}, c_{j+\frac{1}{2}}, \chi^{R}_{G}\right) \\ \mathbf{Q}_{3,j}\tilde{V}^{+}\left((u_L)_j, c_{j+\frac{1}{2}}, \chi^{L}_{L}\right) + \mathbf{Q}_{3,j+1}\tilde{V}^{-}\left((u_L)_{j+1}, c_{j+\frac{1}{2}}, \chi^{R}_{L}\right) \\ 0.5\left\{\left[\left(\mathbf{F}^{c}_{j+1/2}\right)_2 + \left(\mathbf{F}^{c}_{j+1/2}\right)_7\right]\left[(u_G)_j + (u_G)_{j+1}\right] - \left[\left|\left(\mathbf{F}^{c}_{j+1/2}\right)_2\right| + \left|\left(\mathbf{F}^{c}_{j+1/2}\right)_7\right|\right]\left[(u_G)_{j+1} - (u_G)_j\right]\right\} \\ 0.5\left\{\left[\left(\mathbf{F}^{c}_{j+1/2}\right)_3 + \left(\mathbf{F}^{c}_{j+1/2}\right)_6\right]\left[(u_L)_j + (u_L)_{j+1}\right] - \left[\left|\left(\mathbf{F}^{c}_{j+1/2}\right)_3\right| + \left|\left(\mathbf{F}^{c}_{j+1/2}\right)_6\right|\right]\left[(u_L)_{j+1} - (u_L)_j\right]\right\} \\ \mathbf{Q}_{6,j}\tilde{V}^{+}\left((u_L)_j, c_{j+\frac{1}{2}}, \chi^{L}_{B}\right) + \mathbf{Q}_{6,j+1}\tilde{V}^{-}\left((u_L)_{j+1}, c_{j+\frac{1}{2}}, \chi^{R}_{B}\right) \\ \mathbf{Q}_{7,j}\tilde{V}^{+}\left((u_G)_j, c_{j+\frac{1}{2}}, \chi^{L}_{D}\right) + \mathbf{Q}_{7,j+1}\tilde{V}^{-}\left((u_G)_{j+1}, c_{j+\frac{1}{2}}, \chi^{R}_{D}\right) \end{bmatrix}. \quad (4.21)$$

For the calculation of the pressure flux, both methods, AUSMV and AUSMD, follow the same steps of solution. The pressure-weighted factor value is defined as

$$P^{\pm}(u_k, c) = \begin{cases} \left[\pm\frac{1}{4c}(u_k \pm c)^2\right]\frac{1}{c}\left(\pm 2 - \frac{u_k}{c}\right), if\ |u_k| \le c \\ \frac{u_k \pm |u_k|}{2u_k}, \text{otherwise.} \end{cases} \tag{4.22}$$

For the 5E2P,

$$\mathbf{F}^{p}_{j+\frac{1}{2}} = \begin{bmatrix} 0 \\ 0 \\ 0 \\ P^{+}\left(u_G, c_{j+1/2}\right)(\alpha_G \Delta p_{IG})_j + P^{-}\left(u_G, c_{j+1/2}\right)(\alpha_G \Delta p_{IG})_{j+1} \\ P^{+}\left(u_L, c_{j+1/2}\right)(\alpha_L \Delta p_{IL})_j + P^{-}\left(u_L, c_{j+1/2}\right)(\alpha_L \Delta p_{IL})_{j+1} \end{bmatrix}. \tag{4.23}$$

And for the 7E2P,

$$\mathbf{F}^{p}_{j+\frac{1}{2}} = \begin{bmatrix} 0 \\ 0 \\ 0 \\ P^{+}\left(u_G, c_{j+1/2}\right)[(\alpha_G + \alpha_D)\Delta p_{IG}]_j + P^{-}\left(u_G, c_{j+1/2}\right)[(\alpha_G + \alpha_D)\Delta p_{IG}]_{j+1} \\ P^{+}\left(u_L, c_{j+1/2}\right)[(\alpha_L + \alpha_B)\Delta p_{IL}]_j + P^{-}\left(u_L, c_{j+1/2}\right)[(\alpha_L + \alpha_B)\Delta p_{IL}]_{j+1} \\ 0 \\ 0 \end{bmatrix}. \tag{4.24}$$

The AUSMDV method is a balance between the previous defined methods, AUSMV and AUSMD. Thus, the convective fluxes are weighted by a parameter, *ss*, as follows

$$\mathbf{F}^{\text{AUSMDV},c}_{j+\frac{1}{2}} = ss\mathbf{F}^{\text{AUSMV},c}_{j+\frac{1}{2}} + (1 - ss)\mathbf{F}^{\text{AUSMD},c}_{j+\frac{1}{2}}. \tag{4.25}$$

It is worth mentioning that the pressure flux remains the same for the AUSMDV method, calculated according to Eqs. (4.22), (4.23) and (4.24). According to Evje and Flätten (2003), the parameter *ss* can be defined in many ways and depends on the problem that is being solved. For single phase cases, for instance, Wada and Liou (1997) suggested that this parameter was a function of the local pressure. For two-phase flow, other

possibilities could be adopted, however, as this is a problem-dependent parameter, it will be left open to be determined in the results section of this work.

4.2.3 Discretization of the Non-Conservative Term

The non-conservative term in Eq. (4.9) is discretized using a particular numerical scheme, called second-order Minmod that was proposed by Harten (1983) and used by Omgba-Essama (2004), Figueiredo *et al*. (2017) and Sondermann *et al*. (2019). This methodology can be expressed as

$$\left(\mathbf{H}\frac{\partial \mathbf{N}}{\partial x}\right)_j^n = \frac{\mathbf{H}_j^n}{\Delta x} m(\mathbf{x},\mathbf{y},\mathbf{z}), \tag{4.26}$$

where $\mathbf{H}_j^n = \mathbf{H}(\mathbf{W}_j^n)$ and the $m(\mathbf{x},\mathbf{y},\mathbf{z})$ is the Minmod function defined as

$$m(\mathbf{x},\mathbf{y},\mathbf{z}) \equiv \begin{cases} s\min\{|\mathbf{x}|,|\mathbf{y}|,|\mathbf{z}|\}, & \text{if } \operatorname{sgn}(\mathbf{x}) = \operatorname{sgn}(\mathbf{y}) = \operatorname{sgn}(\mathbf{z}) = s \\ 0, & \text{otherwise,} \end{cases} \tag{4.27}$$

with

$$\boldsymbol{x} \equiv 2(\mathbf{N}_{j+1}^n - \mathbf{N}_j^n), \boldsymbol{y} \equiv \frac{1}{2}(\mathbf{N}_{j+1}^n - \mathbf{N}_{j-1}^n), \boldsymbol{z} \equiv 2(\mathbf{N}_j^n - \mathbf{N}_{j-1}^n). \tag{4.28}$$

All terms in the equations above must be interpreted componentwise. Other simpler forms of discretization can also be implemented, such as centered discretization, according to Paillère *et al*. (2003), or even the first order Minmod as suggested by Coquel *et al.* (1997), although less accurate.

4.3 Roe Method

The Roe method has a different structure from the other methods detailed in the previous section. It is widely reported in the literature for being an approximate Riemann solver and for presenting interesting results when capturing discontinuities and showing

accuracy in the solution, although it requires a longer computational time than the other methods already presented.

4.3.1 General Formulation of the Roe Method

To solve the system of partial differential equations using the Roe method, it is necessary to write it in a conservative form,

$$\frac{\partial \mathbf{Q}}{\partial t} + \frac{\partial \mathbf{F}(\mathbf{Q})}{\partial x} = \mathbf{S}(\mathbf{Q}), \tag{4.29}$$

where, as already described, **Q** is the conservative variables vector, **F(Q)** is the flux vector and **S(Q)** is the source term vector. Unfortunately, for the models studied in this work, it cannot be done due to the pressure terms in the momentum equations, Eqs. (3.4 – 3.5) and Eqs. (3.14 – 3.15), as also pointed out by Munkejord (2005) and Ferrari *et al.* (2017). It is worth mentioning that for the AUSM-type methods, those terms are considered non-conservative terms, as presented in Eq. (4.1). However, with the Roe method, these terms must be incorporated in the conservative form, as Eq. (4.29). Therefore, to use the Roe method, the systems of equations must be rewritten in quasi-linear form

$$\frac{\partial \mathbf{Q}}{\partial t} + \mathbf{A}(\mathbf{Q})\frac{\partial \mathbf{Q}}{\partial x} = \mathbf{S}(\mathbf{Q}). \tag{4.30}$$

Appendix A of this work presents a detailed calculation procedure to obtain the matrix **A**. It can be written, for the 5E2P model, as

$$\mathbf{A}(\mathbf{Q}) = \begin{bmatrix} u_I & 0 & 0 & 0 & 0 \\ 0 & 0 & 0 & 1 & 0 \\ 0 & 0 & 0 & 0 & 1 \\ \Delta p_{IG} - \rho_G c_G^2 & c_G^2 - u_G^2 & 0 & 2u_G & 0 \\ -\Delta p_{IL} + \rho_L c_L^2 & 0 & c_L^2 - u_L^2 & 0 & 2u_L \end{bmatrix}. \tag{4.31}$$

The eigenvalues are analytical expressions, given by: $\lambda_1 = u_I$, $\lambda_2 = u_G - c_G$, $\lambda_3 = u_G + c_G$, $\lambda_4 = u_L - c_L$ e $\lambda_5 = u_L + c_L$. The eigenvectors of matrix **A**, with the right

eigenvectors, **R**, in columns, and matrix $\mathbf{R^{-1}}$, the inverse matrix of **R**, are also presented in Appendix A.

For the 7E2P model, the same calculation procedure is performed, returning larger matrices, that are also detailed in Appendix A. Defining $X \equiv c_G^2\alpha_D\rho_G + c_L^2\alpha_G\rho_L$, $Y \equiv c_G^2\alpha_L\rho_G + c_L^2\alpha_B\rho_L$, $Z \equiv c_G^2c_L^2(\alpha_D + \alpha_G)$ and $K \equiv c_G^2c_L^2(\alpha_B + \alpha_L)$ the Jacobian matrix for the 7E2P model is obtained

$$\mathbf{A(Q)} = \begin{bmatrix} u_I & 0 & 0 & 0 & 0 & 0 & 0 \\ 0 & \frac{\alpha_D u_G \rho_L}{\alpha_G\rho_G + \alpha_D\rho_L} & 0 & \frac{\alpha_G\rho_G}{\alpha_G\rho_G + \alpha_D\rho_L} & 0 & 0 & -\frac{\alpha_G u_G \rho_G}{\alpha_G\rho_G + \alpha_D\rho_L} \\ 0 & 0 & \frac{\alpha_B u_L \rho_G}{\alpha_L\rho_L + \alpha_B\rho_G} & 0 & \frac{\alpha_L\rho_L}{\alpha_L\rho_L + \alpha_B\rho_G} & -\frac{\alpha_L u_L \rho_L}{\alpha_L\rho_L + \alpha_B\rho_G} & 0 \\ \Delta p_{IG} - \frac{Z\rho_L\rho_G}{X} & \frac{Z\rho_L}{X} - u_G^2 & 0 & 2u_G & 0 & 0 & \frac{Z\rho_G}{X} - u_G^2 \\ -\Delta p_{IL} + \frac{K\rho_L\rho_G}{Y} & 0 & \frac{K\rho_G}{Y} - u_L^2 & 0 & 2u_L & \frac{K\rho_L}{Y} - u_L^2 & 0 \\ 0 & 0 & -\frac{\alpha_B u_L \rho_G}{\alpha_B\rho_G + \alpha_L\rho_L} & 0 & \frac{\alpha_B\rho_G}{\alpha_B\rho_G + \alpha_L\rho_L} & \frac{\alpha_L u_L \rho_L}{\alpha_B\rho_G + \alpha_L\rho_L} & 0 \\ 0 & -\frac{\alpha_D u_G \rho_L}{\alpha_G\rho_G + \alpha_D\rho_L} & 0 & \frac{\alpha_D\rho_L}{\alpha_G\rho_G + \alpha_D\rho_L} & 0 & 0 & \frac{\alpha_G u_G \rho_G}{\alpha_G\rho_G + \alpha_D\rho_L} \end{bmatrix}. \quad (4.32)$$

The eigenvalues of the matrix **A** are: $\lambda_1 = u_I$, $\lambda_2 = u_G, \lambda_3 = u_L, \lambda_4 = u_G - \sqrt{\frac{c_G^2c_L^2(\alpha_D+\alpha_G)^2\rho_L\rho_G}{(\alpha_G\rho_G+\alpha_D\rho_L)X}}$, $\lambda_5 = u_G + \sqrt{\frac{c_G^2c_L^2(\alpha_D+\alpha_G)^2\rho_L\rho_G}{(\alpha_G\rho_G+\alpha_D\rho_L)X}}$, $\lambda_6 = u_L - \sqrt{\frac{c_G^2c_L^2(\alpha_B+\alpha_L)^2\rho_L\rho_G}{(\alpha_B\rho_G+\alpha_L\rho_L)Y}}$ *e* $\lambda_7 = u_L + \sqrt{\frac{c_G^2c_L^2(\alpha_B+\alpha_L)^2\rho_L\rho_G}{(\alpha_B\rho_G+\alpha_L\rho_L)Y}}$.

With the determination of the matrices **A** for the 5E2P and 7E2P models, an explicit discretization of Godunov's method with a high-resolution extension is written, according to LeVeque (2004), as follows

$$\mathbf{Q}_j^{n+1} = \mathbf{Q}_j^n - \frac{\Delta t}{\Delta x}\left[\sum_{p=1}^{m}(\lambda_{j+1/2}^p)^-\boldsymbol{w}_{j+1/2}^p + \sum_{p=1}^{m}(\lambda_{j-1/2}^p)^+\boldsymbol{w}_{j-1/2}^p\right] - \frac{\Delta t}{\Delta x}\left[\tilde{\mathbf{F}}_{j+\frac{1}{2}}^n - \tilde{\mathbf{F}}_{j-\frac{1}{2}}^n\right]. \quad (4.33)$$

where p is the number of eigenvalues, $1 \leq p \leq$ m, for a given hyperbolic system and m is total number of eigenvalues, which is equals to the number of equations of the mathematical model. The components of the vector $\boldsymbol{w}_{j-1/2}^p$ represents the waves crossing

the cell's interface and $\lambda_{j-1/2}^{p}$ are the characteristic velocities of the wave of number *p*, in which

$$\boldsymbol{w}_{j-1/2}^{p} = \beta_{j-1/2}^{p} \boldsymbol{r}_{j-1/2}^{p}. \tag{4.34}$$

where $\boldsymbol{r}_{j-1/2}^{p}$ are the right eigenvectors written as columns and the term $\beta_{j-1/2}^{p}$ is defined as

$$\beta_{j-1/2}^{p} = \mathbf{R}_{j-1/2}^{-1}(\mathbf{Q}_{j} - \mathbf{Q}_{j-1}). \tag{4.35}$$

The term $(\lambda_{j-1/2}^{p})^{\pm}$ with positive or negative indexes in Eq. (4.33) is interpreted according to

$$(\lambda_{j-1/2}^{p})^{\pm} = \frac{1}{2}\left(\lambda_{j-1/2}^{p} \pm \left|(\lambda_{j-1/2}^{p})\right|\right). \tag{4.36}$$

The flux vector, $\tilde{\mathbf{F}}_{j-\frac{1}{2}}^{n}$, is the high-resolution correction, as defined by LeVeque (2004), and it is a function of the eigenstructure of **A** and of the flux limiter $\phi(\Psi_{j-1/2}^{p})$,

$$\tilde{\mathbf{F}}_{j-\frac{1}{2}}^{n} = \frac{1}{2}\sum_{p=1}^{m}\left|(\lambda_{j-1/2}^{p})\right|\left(1 - \frac{\Delta t}{\Delta x}\left|(\lambda_{j-1/2}^{p})\right|\right)\phi(\Psi_{j-1/2}^{p})\boldsymbol{w}_{j+1/2}^{p}. \tag{4.37}$$

The high-resolution term is a way to guarantee accuracy and, at the same time, avoid numerical oscillations to be introduced in the solution. The flux limiter can be defined, according to LeVeque (2004), based on the following expression

$$\Psi_{j-\frac{1}{2}}^{p} = \frac{\beta_{J-1/2}^{p}}{\beta_{j-1/2}^{p}}, \text{ with } \mathrm{J} = \begin{cases} j-1 \; se \; \lambda_{j-\frac{1}{2}}^{p} > 0 \\ j+1 \; se \; \lambda_{j-\frac{1}{2}}^{p} < 0 \end{cases}. \tag{4.38}$$

The function ϕ can be calculated by the van Leer (1974) limiter, as an example, as used by Santim and Rosa (2015),

$$\phi(\Psi) = \frac{\Psi + |\Psi|}{1 + |\Psi|}. \tag{4.39}$$

4.3.2 Roe Linearization

The Roe linearization is detailed in LeVeque (2004) to define the approximate Riemann solution. The quasi-linear form described by Eq. (4.30) is replaced by a linearized problem defined at each cell interface.

$$\frac{\partial \widehat{\mathbf{Q}}}{\partial t} + \widehat{\mathbf{A}}_{j-1/2} \frac{\partial \widehat{\mathbf{Q}}}{\partial x} = 0. \tag{4.40}$$

The Roe matrix, $\widehat{\mathbf{A}}_{j-1/2}$ is an approximation of the matrix **A** at the cell interface ($\mathbf{Q}_{j-1}$ and $\mathbf{Q}_j$) that must satisfy the following conditions, according to LeVeque (2004)

- it must be diagonalizable with real eigenvalues to guarantee hyperbolicity;
- $\widehat{\mathbf{A}}_{j-\frac{1}{2}}(\mathbf{Q}_{j-1}, \mathbf{Q}_j) \rightarrow \mathbf{A}(\overline{\mathbf{Q}})$ as $\mathbf{Q}_{j-1}, \mathbf{Q}_j \rightarrow \overline{\mathbf{Q}}$ to make the method consistent with the original conservation law, Eq. (4.30);
- $\widehat{\mathbf{A}}_{j-\frac{1}{2}}\left(\mathbf{Q}_{j-1}, \mathbf{Q}_j\right) = \mathbf{F}\left(\mathbf{Q}_j\right) - \mathbf{F}\left(\mathbf{Q}_{j-1}\right)$ to ensure that the method is conservative.

The matrix $\widehat{\mathbf{A}}_{j-1/2}$ must be defined satisfying the above conditions, such that

$$\widehat{\mathbf{A}}_{j-1/2} = \mathbf{A}\left(\widehat{\mathbf{Q}}_{j-\frac{1}{2}}\right), \tag{4.41}$$

where $\widehat{\mathbf{Q}}_{j-1/2}$ is an average between $\mathbf{Q}_{j-1}$ and $\mathbf{Q}_j$. Munkejord (2005) and Evje and Flätten (2003) and Ferrari *et al.* (2017) used the average state of $\widehat{\mathbf{Q}}_{j-1/2}$ and proved that the above conditions are satisfied. This average state is defined as

$$\hat{u} = \frac{u_{j-1}\sqrt{(\alpha\rho)_{j-1}} + u_j\sqrt{(\alpha\rho)_j}}{\sqrt{(\alpha\rho)_{j-1}} + \sqrt{(\alpha\rho)_j}}, \tag{4.42}$$

$$\hat{\alpha} = \frac{1}{2}(\alpha_{j-1} + \alpha_j), \tag{4.43}$$

$$\hat{\rho} = \frac{1}{2}(\rho_{j-1} + \rho_j), \tag{4.44}$$

$$\widehat{\Delta p} = \frac{1}{2}(\Delta p_{j-1} + \Delta p_j), \tag{4.45}$$

$$\widehat{u_I} = \frac{1}{2}\left(u_{I\,j-1} + u_{I\,j}\right). \tag{4.46}$$

The Eqs. (4.42 – 4.46) are used as coefficients of the matrix in Eq. (4.31) for the 5E2P model and Eq. (4.32) for the 7E2P model and, consequently, in matrices $\mathbf{R}$ and $\mathbf{R^{-1}}$, that are detailed in Appendix A. The linearized Roe matrices and their respective eigenvalues and eigenvectors are used in the Godunov method for the solution of the problem.

4.4 Imposition of Boundary Conditions

As reported in chapter 3, a hyperbolicity analysis of the mathematical model under the flow conditions is necessary in order to determine the number of boundary conditions that should be prescribed in each boundary at every time step in an initial-boundary-value problem. According to Jeffrey (1976), the hyperbolicity analysis is local in each boundary and the number of prescribed conditions is a function of the number of characteristics that emanate from the boundary into the domain. For the 5E2P model, five characteristics are obtained from the hyperbolicity analysis, whereas for the 7E2P, they are seven. In both mathematical models, two negative characteristics are derived in each boundary and the remaining ones are positive. At the inlet, the positive characteristics emanate into the domain and, therefore, three, or five, boundary conditions are imposed, for the 5E2P and

7E2P models, respectively. On the other hand, the two negative characteristics at the outlet are the ones that emerge into the domain and, consequently, prescribed at the outlet.

For cases simulated in this work, boundary conditions of the Dirichlet type for both inlet (x=0) and outlet (x=L) are considered. It is common in the literature, as described in Figueiredo *et al.* (2017) and Sondermann *et al.* (2019), to impose the pressure at the outlet and the other flow variables at the inlet. Therefore, fluid pressures are prescribed as outlet boundary conditions for the two mathematical models herein studied, while fluid velocities and liquid volume fraction are imposed at the inlet. For the 7E2P, as two more boundary conditions at the inlet are required, bubbles and droplets volume fractions are also prescribed. The boundary conditions are imposed at ghost cells that are added to the left and right boundaries. The non-prescribed values in each boundary are replications of the calculated values in the nearest discretized inner cell in the previous time step. The values set as boundary conditions at the initial time step are taken as initial conditions throughout the discretized domain.

5. Experimental Facilities

An experimental campaign was performed at the TUFFP facilities (Tulsa University Fluid Flow Projects) located at the University of Tulsa in Tulsa, Oklahoma, USA. Two different experimental facilities were used: the 4-in air-water facility and the 2-in high viscosity oil-air facility. The experimental data acquired in this campaign is used as a validation of the results obtained with the numerical simulations.

5.1 4-in Facility

This experimental facility was also used in the previous works of Roullier (2017) and Zhu (2019). Roullier (2017) studied the existence of slug flow in air-water two-phase flow in vertical pipes, whereas Zhu (2019) investigated the effect of the inclination angle of the pipe on the transition from slug flow to churn/pseudo-slug flows. The test section of this facility is made of polycarbonate and consists of a loop that has an upward and a downward pipe connected. This flow loop can be inclined ranging from horizontal to almost 90° and the fluids used in the system are water and air that are mixed at the inlet of the flow loop. Pictures of the 4-in facility are presented in Fig. 4.

Figure 4: Pictures of the 4-in facility.

The liquid delivery system of this facility is composed of two centrifugal pumps, running in parallel, that drives the water from a water tank, a mass flowmeter, pressure and temperature transmitters, and an automatic control valve to adjust the flow rate with a bypass, controlled by a manual valve, that is used to empty the system whenever it is necessary. The gas delivery system has a similar configuration. The air, however, is delivered by a centralized air compressor (Gardner Denver with discharge pressure at 100 psig), whose pressure is measured before enters the system. At the inlet of the test section, both delivery systems are connected, and the fluids are mixed. At the end of the test section, there is a U-shape hose that bridges the upward (test section) and downward (returning section) of the flow loop. The test section has three trapping segments separated by quick closing valves (QCVs, for short) and instrumented with differential pressure transducers. In the first trap section there are a pair of conductivity sensors and a temperature transmitter, whereas in the second one, there are another pair of conductivity sensor and a pressure transmitter. In the third and last trap, the Wire-Mesh sensor is installed, to guarantee that the flow is fully developed. At the very outlet of the test section, there is a pressure transmitter to monitor the pressure and, consequently, keep it under control by an automatic control valve. The return section of this flow loop is made of steel, there is no instrumentation, and the diameter has 3-in.

5.1.1 Flow Loop Instrumentation

The test section of the flow loop is equipped with measuring instruments that are able to provide the necessary information to obtain the flow parameters. Figure 5 presents the schematic of the experimental facility, not in full-scale, indicating the main instrumentation in the test section.

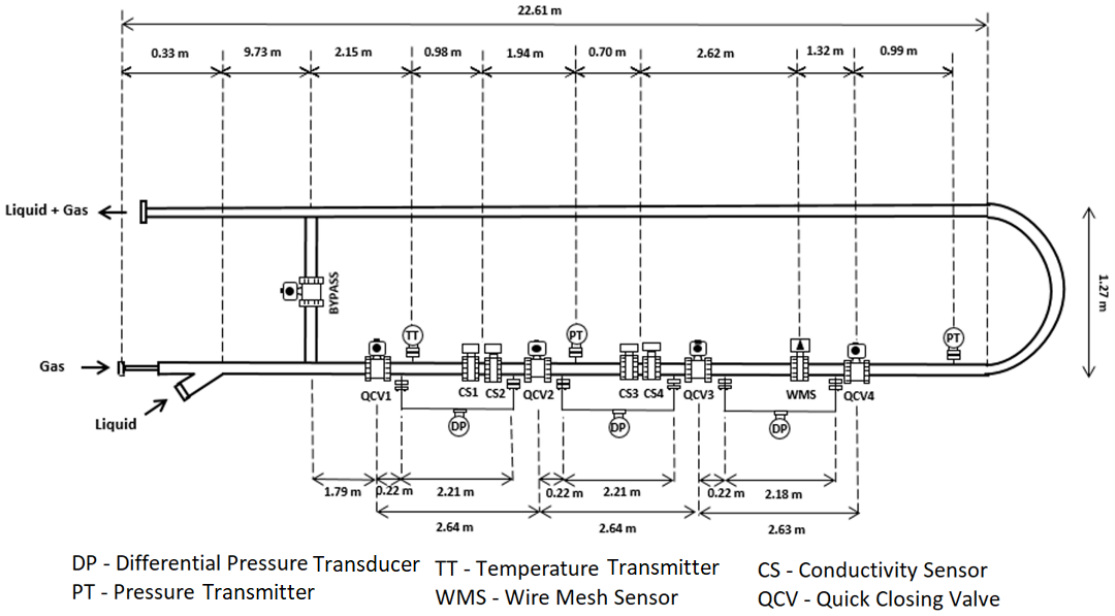

Figure 5: Schematic of the 4-inch facility.

The basic instrumentation is detailed as follows.

- Differential Pressure Transducer (DP):

The DP sensors are used to measure the pressure drop during the tests. There are three DPs in the test section, one in each trap. The trap sections are located between the Quick Closing Valves (QVC) that are used to quickly retain the flow whenever is needed. For pressure drop measurements on each trap,

$$\mathrm{DP} = (\mathrm{DP}_{test} - \mathrm{DP}_{empty}), \tag{5.1}$$

and

$$\frac{dp}{dL}\Big)_{each\ DP} = \frac{\mathrm{DP}}{L_{DP}}, \tag{5.2}$$

where DP is the corrected pressure difference in Pa, DP_{test} is the pressure difference acquired from data recorded with the LabVIEW under continuous flow conditions, already converted to Pa, and DP_{empty} is the pressure difference that is measured when the pipe is empty with the same inclination angle of the test. L_{DP} is the length of the DP sensor. The sample frequency is 5Hz and the DP range for each inclination angle is

detailed in Table 1. Verification of the DP sensors in single-phase flow are presented in Appendix B.

Table 1: DP span for each inclination angel.

Angle (°)	DP span (inH_2O)
2	-10 to 10
5	-15 to 10
15	-30 to 10
20	-40 to 10
30	-50 to 10

To calculate the average pressure gradient, it is necessary to use the information of all the trap sections, according to the following expression

$$\frac{dp}{dL}\Big)_{av} = \frac{1}{3}\sum \frac{dp}{dL}\Big)_{each}. \tag{5.3}$$

- Pressure and Temperature Transmitters (PT/TT):

Two pressure and one temperature sensors are installed to measure pressure and temperature along the pipeline. The PTs are located in the second trap and at the end of the test section, while the TT is in the first trap, as illustrated by Fig. 5.

- Flowmeter:

Two Coriolis flowmeters (E-H™ Promass 83F) are installed in the liquid and gas deliveries systems to measure the gas and liquid mass flow rates, respectively. With that information, in addition to pressure and temperature values, the superficial velocities can be calculated.

- Conductivity Sensors (CS):

Two pairs of conductivity sensors are installed in order to obtain the slug flow characteristics. The measurement is based on the conductivity difference of the fluids, which means that whenever the sensor is submerged in water, the conductivity data furnishes the maximum voltage, V_{max}, while with an empty pipe it has its minimum

voltage, V_{min}. The data acquisition frequency of these sensors is 1000 Hz. The normalized output voltage, V_{norm}, is calculated as

$$V_{norm} = \frac{V_{test} - V_{min}}{V_{max} - V_{min}}, \tag{5.4}$$

where V_{test} is the data obtained when the fluids are flowing. In the case of slug flow, for example, the conductivity data can be used to obtain slug characteristics, such as slug frequency and translational velocity.

- Wire Mesh Sensor (WMS)

The WMS is an intrusive instrumentation that measures the instantaneous distributions of the phases in two-phase flows. It consists of two planes of wire electrodes, transmitter and receiver planes. The wires on each plane are parallel to each other and separated by a few millimeters whereas the wires of the two planes cross each other perpendicularly. The number of wire-crossing points may vary, and for this study it is 32x32. The measurements of the phase distributions are taken at these crossing points by measuring the electrical conductivity for conducting fluids and permittivity for non-conducting fluids. The WMS used in this study, constructed by HZDR in Germany, has a pair of 32x32 conductivity wires and the data acquisition frequency was 2500 Hz. In the work of Fan (2017), more information on the WMS is provided. This sensor is capable of offering the liquid holdup measurement, and this information can be used to calculate slug characteristics.

5.1.2 Test Matrix

The test matrix combines all the experimental campaign performed in the 4-in facility. Five inclination angles were investigated from 2° to 30° under a pressure of 65 psig measured close to the end of the test section. Several inclinations and superficial gas and liquid velocities were tested, as presented in Table 2.

Table 2: Test Matrix for the 4-in facility.

Inclination Angles	2°, 5°, 15°, 20° and 30°
u_{SL}	0.05 m/s
u_{SG}	From 0.27 m/s to 1.08m/s
Pressure	65 psig

5.2 2-in Facility

The test section of this flow loop has an internal diameter of 2-in and is located in an indoor facility where room temperature is controlled by an air conditioning system to minimize the heat transfer with the environment. Figure 6 is a picture of the experimental facility.

Figure 6: Picture of the 2-in facility.

The fluids present in this facility are a high viscosity oil (Synthetic oil – ISO VG 320) and air. The oil is stored in a tank and its viscosity is controlled by adjusting the liquid temperature inside the tank with a 20-kW Chromalox heater. The oil temperature is measured during the experiments to keep the desired temperature and viscosity. The liquid system is pumped by a 20HP screw pump and the gas is delivered by the same air compressor that was used in the 4-in facility. This flow loop is fixed in the horizontal position for this study and the fluids are mixed at a "Y-2" tee junction before entering the test section, as can be seen in Fig. 7. An acrylic plate is located at one-quarter of the pipe

diameter from the top to guarantee that both fluids are separated in the beginning of the pipe. More information regarding the mixing entrance of the fluids in this facility are presented by Kim (2019) and Brito (2012). The return pipe of this flow loop has 3-in of internal diameter and is connected by a flexible hose. At the end of the pipeline, the fluids are separated by gravity, and the liquid is stored in the tank and the air is vented to the atmosphere.

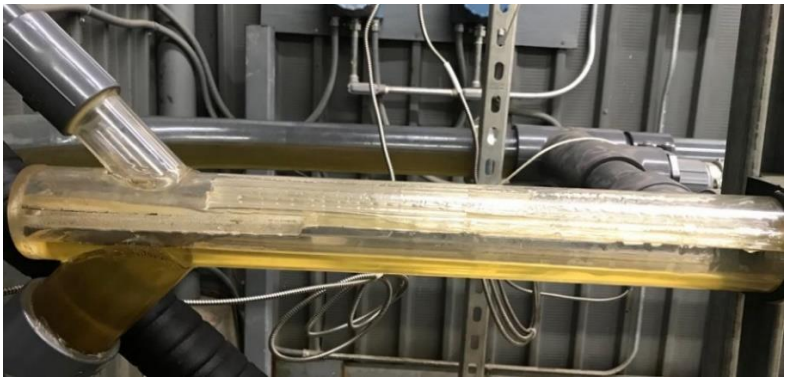

Figure 7: Picture of the inlet of the 2-in facility.

5.2.1 Flow Loop Instrumentation

The instrumentations present in this experimental facility are like the ones in the 4-in facility, as can be verified in the schematic in Fig. 8. The temperature (measured by Resistance Temperature Detectors - RTD), pressure and DP's sensors have data acquisition frequency of 25 Hz. The DP range is -50 to 250 inH_2O and the single-phase test verification of the instrumentation is presented in Appendix B. The flow loop is equipped with mass flow meters (Micro Motion™) and three pairs of capacitance sensors and quick closing valves. Capacitance sensors, with 2000 Hz of data sampling frequency, are used to analyze the slug characteristics in the same way that the conductive sensors already detailed in the previous section.

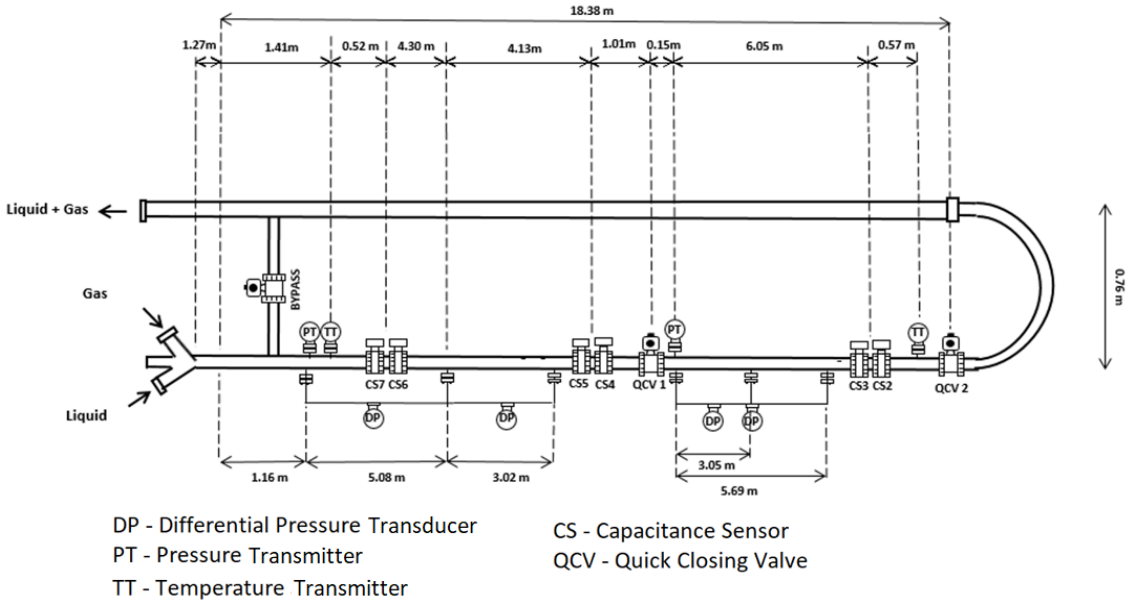

Figure 8: Schematic of the 2-inch facility.

5.2.2 Test Matrix

The experiments that were run in the 2-in facility aim at investigating the flow behavior in a horizontal pipeline under laminar conditions using high viscosity oil and air. This high viscosity oil is operated at a temperature of 70°F with viscosity of 0.68 Pa.s. The oil tank is open to the atmosphere and the oil density is 849.92 kg/m³, as previous studies performed by Kim (2019). Table 3 summarizes the flow conditions that were investigated.

Table 3: Test Matrix for the 2-in indoor facility.

Inclination Angles	Horizontal
u_{SL}	From 0.1 m/s to 0.4 m/s
u_{SG}	From 0.08 m/s to 0.6 m/s
Pressure	Open to atmosphere
Temperature	70°F

6. Numerical Results for Benchmark Problems

The results of this work are divided into two chapters. The first chapter presents the results of several numerical simulations of classical benchmark problems performed to validate the algorithm and the code here developed to simulate slug flows. The second one describes the numerical results of the slug-capturing simulations and a comparison with the experiments carried out at the TUFFP facilities, at the University of Tulsa.

In this first chapter, a numerical study based on the numerical solution of three benchmark problems is presented to analyze the behavior of the mathematical models and numerical methods in different flow scenarios. Then, an accuracy check of the AUSM-type method is performed for a stratified flow simulation for both mathematical models, the 5E2P and the 7E2P.

6.1 Benchmark Problems

This section is dedicated to present the solution of three benchmark problems that are commonly used in two-phase flow simulations: the water faucet, the large relative-velocity shock tube, and the segregation problems. Each problem has its own particularity, although all present a discontinuity in the flow.

6.1.1 The Water Faucet Problem

The water faucet, also called gravity dominated flow, is a benchmark initial-boundary value problem that was first described by Ramson (1987). It consists of a vertical pipe that is filled with gas-liquid two-phase flow. Figure 9 is a schematical representation of the evolution of the flow through time. Figure 9(a) illustrates the initial condition that consists of a uniform flow, in which all the flow variables are constant and equal to the boundary conditions. With the gravitational effect, a discontinuity appears, which grows and travels from the inlet towards the outlet, as in Fig. 9(b). When this discontinuity leaves the pipe, the steady state is reached, as in the illustration in Fig. 9(c).

This benchmark problem has an analytical solution that is used to verify the performance of numerical models with respect to their capability to reproduce the physics of the two-phase flow. It evaluates how well the numerical methods capture and transports

the discontinuity due to the interactions between the body force and advective terms in the conservation equations, since in this problem, there is no wall and interfacial friction forces, and the flow is treated as isothermal.

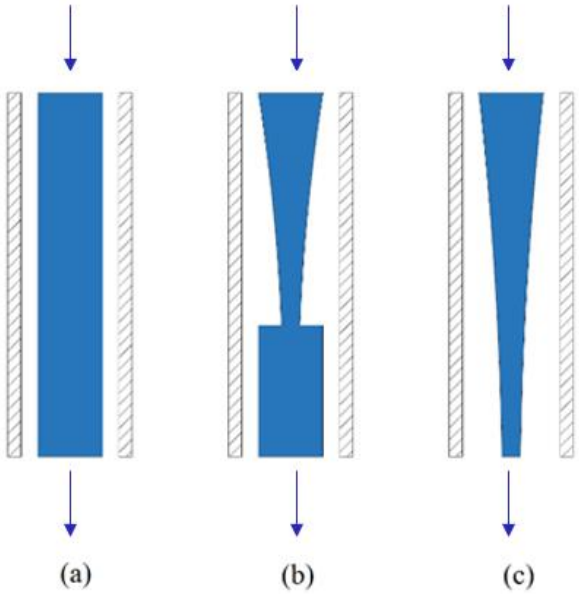

Figure 9: Water faucet problem schematic. (a) Initial uniform condition. (b) Flow snapshot sometime between initial and steady-state condition. (c) Steady-state condition.

The simulation set up for the water faucet is displayed in Table 4 and the boundary conditions for this problem are detailed in Table 5. The initial conditions are equal to the boundary condition uniformly replicated throughout the domain.

Table 4: Simulation set up for the water faucet problem.

Parameter	Value
Gravity	9.81 m/s²
Sound speed in the liquid	1000 m/s
Sound speed in the gas	316.2 m/s
Reference gas density	0 kg/m³
Reference liquid density	1000 kg/m³
Pipe length	12 m
Time (snapshot)	0.6 s
CFL number (AUSM-type/Roe)	0.45/0.9

Table 5: Inlet and outlet boundary conditions for the water faucet benchmark.

Flow Variable	Value
p at outlet ($x=L$)	10^5 Pa
u_G at inlet ($x=0$)	0 m/s
u_L at inlet ($x=0$)	10 m/s
α_G at inlet ($x=0$)	0.2 (-)

The analytical solution, according to Ramson (1987) and Coquel *et al*. (1997), for the void fraction and liquid velocity are

$$\alpha_G(x,t) = \begin{cases} 1 - \dfrac{(\alpha_L u_L)_{x=0}}{\sqrt{2gx + (u_L^2)_{x=0}}}, & \text{if } x \le x_d \\ 1 - (\alpha_L)_{x=0}, & \text{otherwise.} \end{cases} \tag{6.1}$$

$$u_L(x,t) = \begin{cases} \sqrt{(u_L^2)_{x=0} + 2gx}, & \text{if } x \le x_d \\ (u_L)_{x=0} + gt, & \text{otherwise.} \end{cases} \tag{6.2}$$

where the discontinuity location, x_d, is given by $x_d \equiv (u_L)_{x=0}t + \frac{1}{2}gt^2$.

Originally, this problem had no analytical solution for the gas velocity and the pressure fields. The pressure variation was neglected, that is, the pressure was considered to be constant along the line. In the recent work of Zou *et al.* (2016), the authors complemented the analytical study of this problem that was first carried out by Ramson (1987) obtaining the analytical solution for the remaining variables, pressure and gas velocity, that are written as

$$u_G(x,t) = \begin{cases} 0 & \text{, if } x \le x_d \\ -\dfrac{1 - (\alpha_G)_{x=0}}{(\alpha_G)_{x=0}}gt, & \text{otherwise.} \end{cases} \tag{6.3}$$

$$p(x,t) = \begin{cases} (p)_{x=L} - \dfrac{\rho_G g(L-x_d)}{(\alpha_G)_{x=0}} + \dfrac{1}{2}\rho_G \left(\dfrac{1-(\alpha_G)_{x=0}}{(\alpha_G)_{x=0}} gt\right)^2 + \\ \rho_G \dfrac{1-(\alpha_G)_{x=0}}{(\alpha_G)_{x=0}} gt((u_L)_{x=0} + gt) - \rho_G g(x_d - x), \text{ if } x \le x_d \\ (p)_{x=L} - \dfrac{\rho_G g(L-x)}{(\alpha_G)_{x=0}}, \qquad \text{otherwise.} \end{cases} \tag{6.4}$$

In this more recent solution, additional assumptions were made to obtain the analytical solution for the remaining variables. The authors considered that the pressure distribution was deduced from the gas perspective, since the liquid phase is in free fall motion and the pressure gradient in the liquid phase was neglected, assuming that the pressures for both phases can be different. Moreover, the gas phase was treated as incompressible, and the interfacial pressure was neglected. However, for the simulation performed in this work, the interfacial pressure terms are taken into consideration, keeping the consistency of the mathematical models that are herein being studied. Therefore, there is a slight difference between the assumptions adopted in the derivation of the analytical solution and the ones used to obtain the numerical results.

The following graphs present the results for the void fraction along the distance that were obtained with the 5E2P model in combination with the AUSMV, AUSMD, AUSMDV and Roe methods for different mesh sizes to verify how the mesh discretization impacts the solution. The void fraction represents the main flow variable in this problem, and it is the most affected by the grid refinement. The numerical simulation with the Roe method is divided in first and second order in spatial accuracy, with or without the high-resolution correction term, as presented by Eq. (4.37). In addition, as mentioned in chapter 4, the AUSMDV method has a parameter, *ss*, Eq. (4.25), that can be tuned to provide the best solution for each problem, and for this mesh study, *ss*=0.8 was chosen. Among all the benchmark problems, the water faucet problem was selected for the grid refinement study because it is the one that the mesh variation impact can be better visualized graphically.

Figures 10 to 13 show results with 100, 500, 1000, 2000, 5000, 8000 and 10000 cells for the AUSMDV, AUSMV, Roe first and second orders, respectively. The CFL number is 0.45 for the AUSM-type methods and 0.9 for the Roe simulation. Based on these graphs, it can be noticed that the physics of the void fraction in the water faucet problem

is well described, since a discontinuity is formed at the inlet, as gravity is felt by the flow, and travels towards the outlet as time evolves. From the numerical perspective, there is no doubt that the coarser meshes have more difficulty in representing the discontinuity. Even though the results present a diffusive effect, as the mesh is refined the discontinuity is captured more accurately.

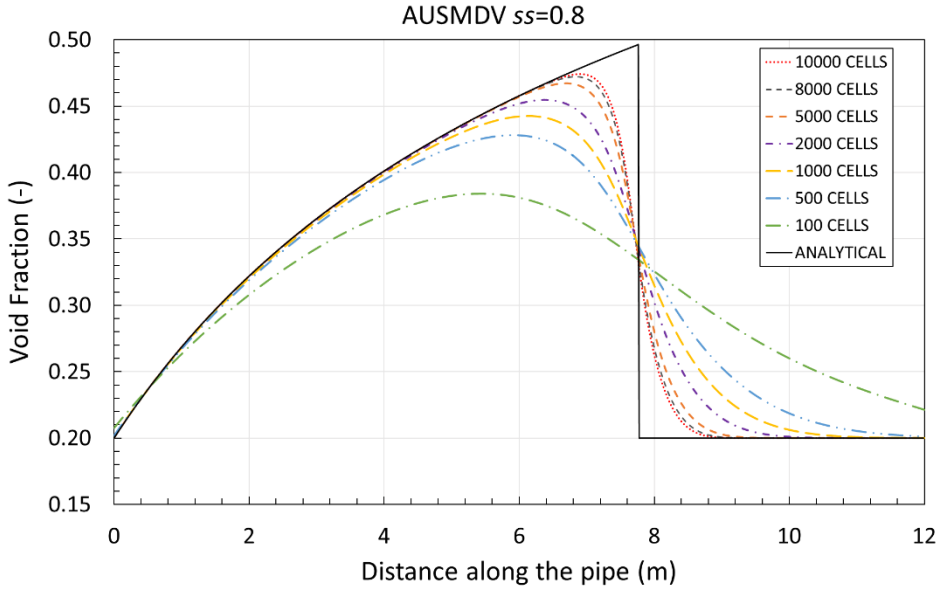

Figure 10: Void fraction distribution along the line for the 5E2P model for the grid refinement study of the water faucet problem at t=0.6s with the AUSMDV 0.8 method.

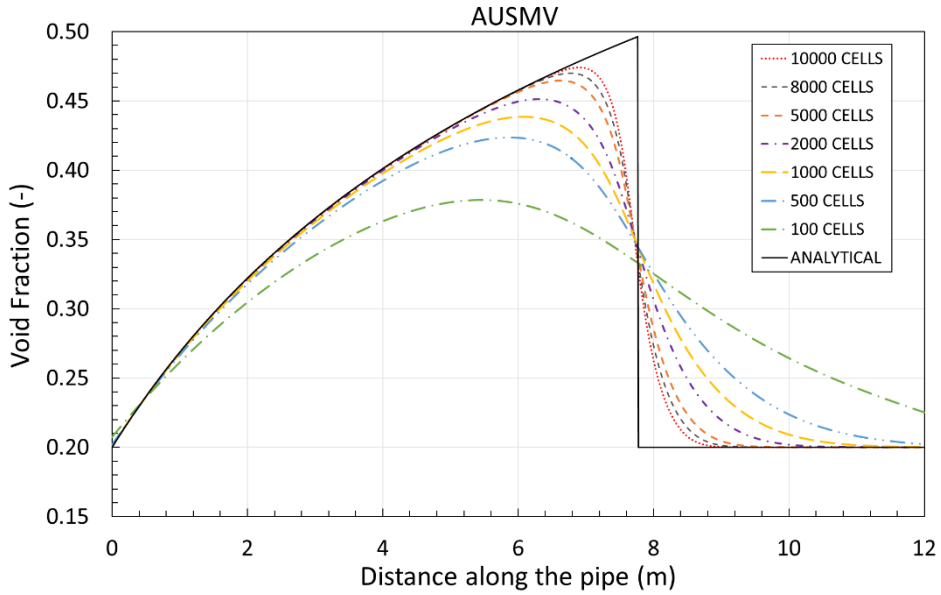

Figure 11: Void fraction distribution along the line for the 5E2P model for the grid refinement study of the water faucet problem at t=0.6s with the AUSMV method.

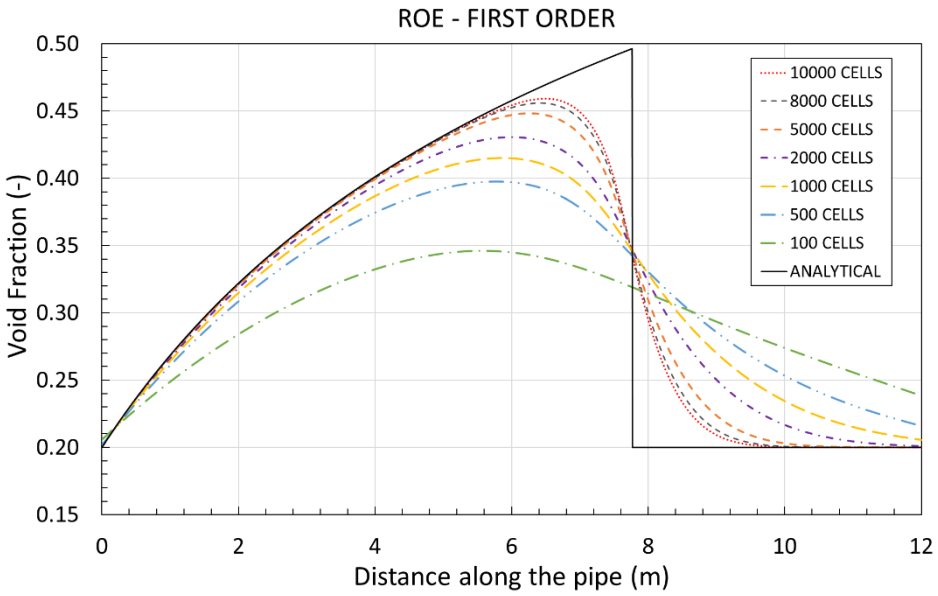

Figure 12: Void fraction distribution along the line for the 5E2P model for the grid refinement study of the water faucet problem at t=0.6s with the Roe first order method.

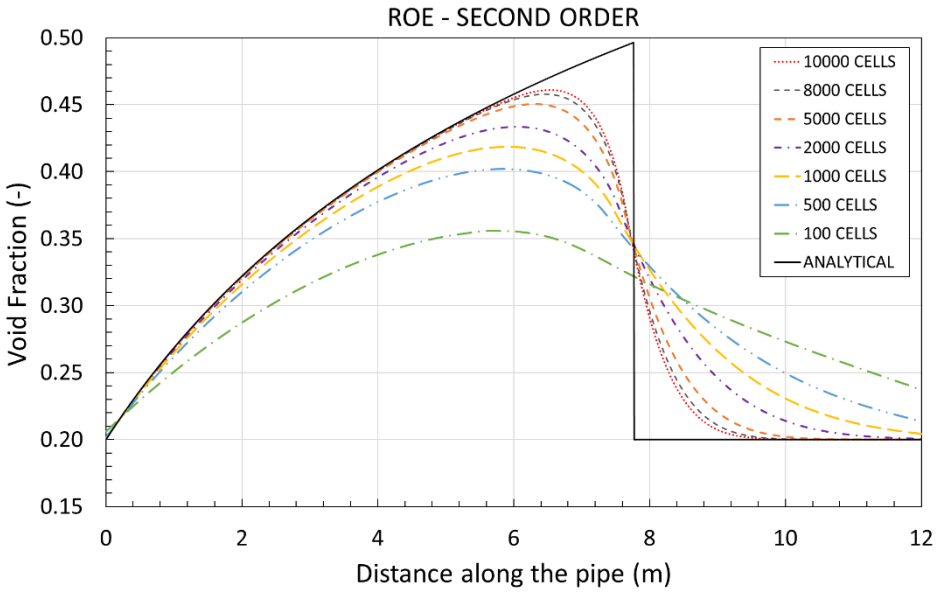

Figure 13: Void fraction distribution along the line for the 5E2P model for the grid refinement study of the water faucet problem at t=0.6s with the Roe second order method.

Taking as an example Fig. 10, AUSMDV solution, the highest void fraction value obtained with 10000 cells is 4.6% away from the analytical solution. Following the same calculation, with 8000 cells is 5.03%, 5000 cells is 6.03% and 2000 is 8.65% away from the reference solution. All other meshes are more than 10% distant from the analytical solution: 11.06% with 1000 cells, 13.88% with 500 cells and 23.7% with 100 cells.

Solutions with 10000, 8000 and 5000 cells are accurate and computationally expensive, especially with the Roe method. On the other hand, solutions with 2000 cells are also accurate and not so much computationally demanding, which are important facts to be considered in simulations that require longer time duration, such as slug capturing. Thus, to have accurate results in less time, all the simulations are performed with 2000 cells from this point on.

To analyze the water faucet problem in a systematic way, all the flow variables are examined by means of the 5E2P model for each numerical method in Figs. 14 to 17. The AUSMDV tuning parameter quantifies how close to the AUSMV and the AUSMD methods the solution is to have an optimized balance of both techniques. The values of 0.2, 0.5 and 0.8 are analyzed for the *ss* parameter. With $ss = 0.2$ the solution approaches AUSMD, with $ss = 0.8$ the solution goes towards AUSMV, and $ss = 0.5$ is in the middle of both methods.

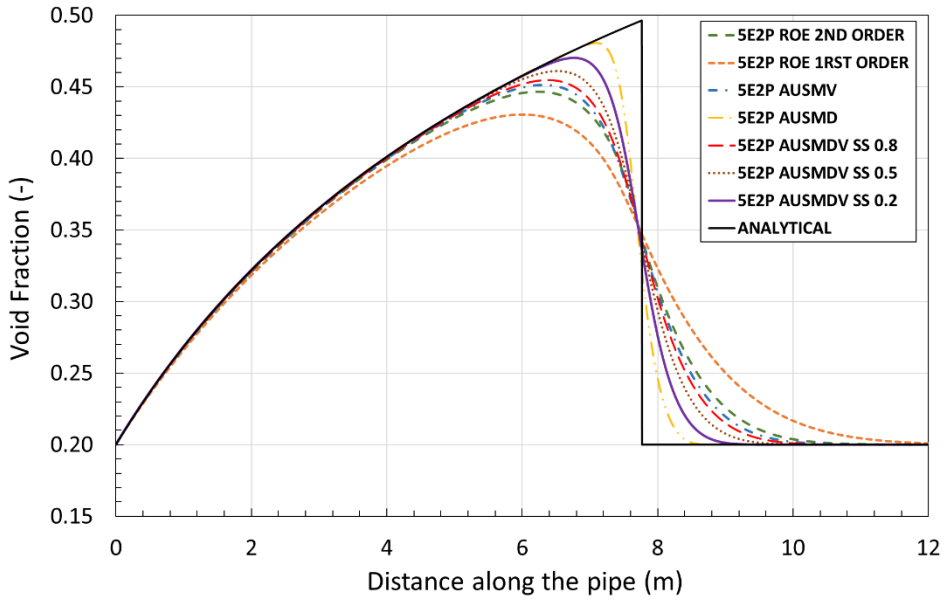

Figure 14: Void fraction distribution along the line for the 5E2P model for the water faucet problem at *t*=0.6s.

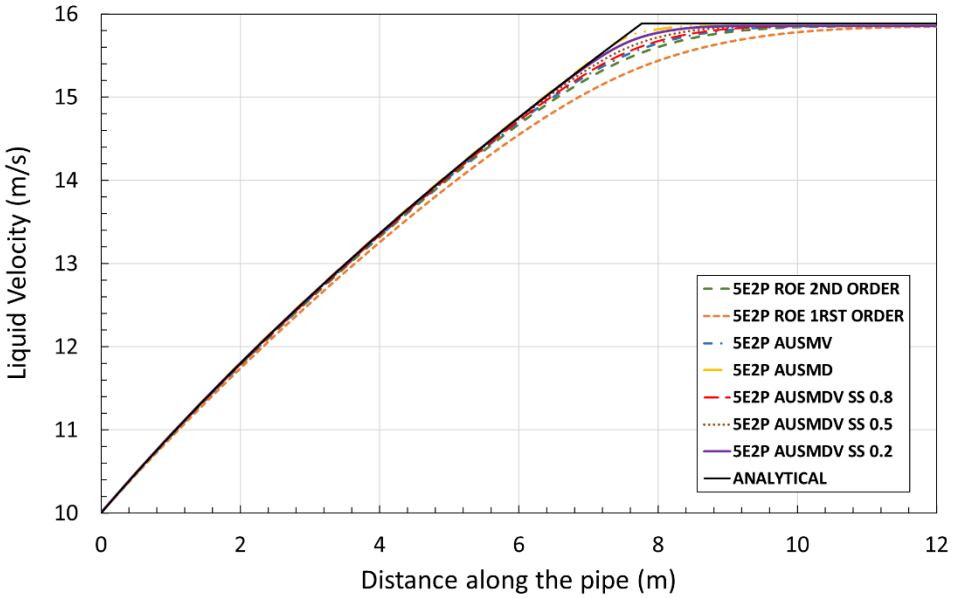

Figure 15: Liquid velocity distribution along the line for the 5E2P model for the water faucet problem at t=0.6s.

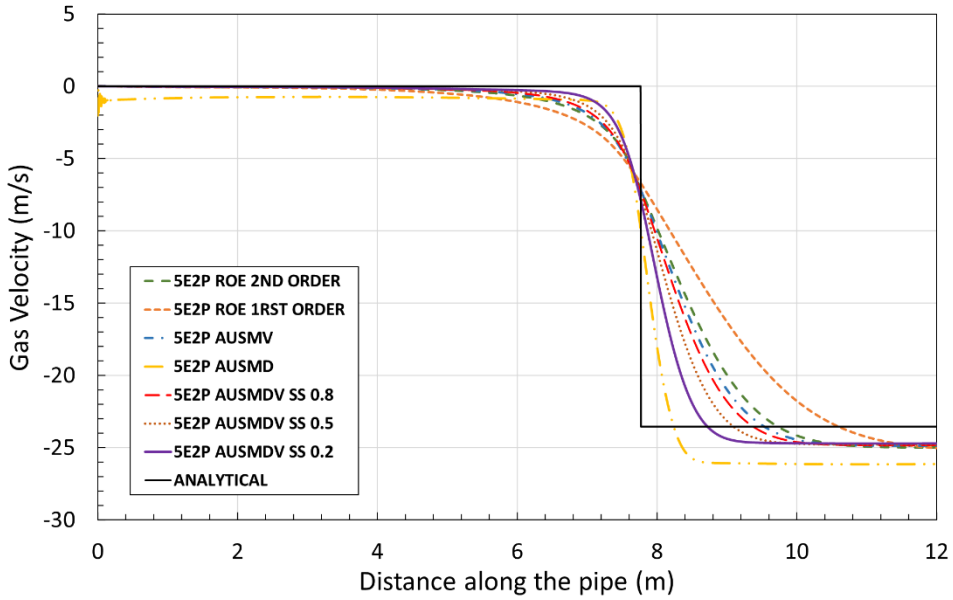

Figure 16: Gas velocity distribution along the line for the 5E2P model for the water faucet problem at t=0.6s.

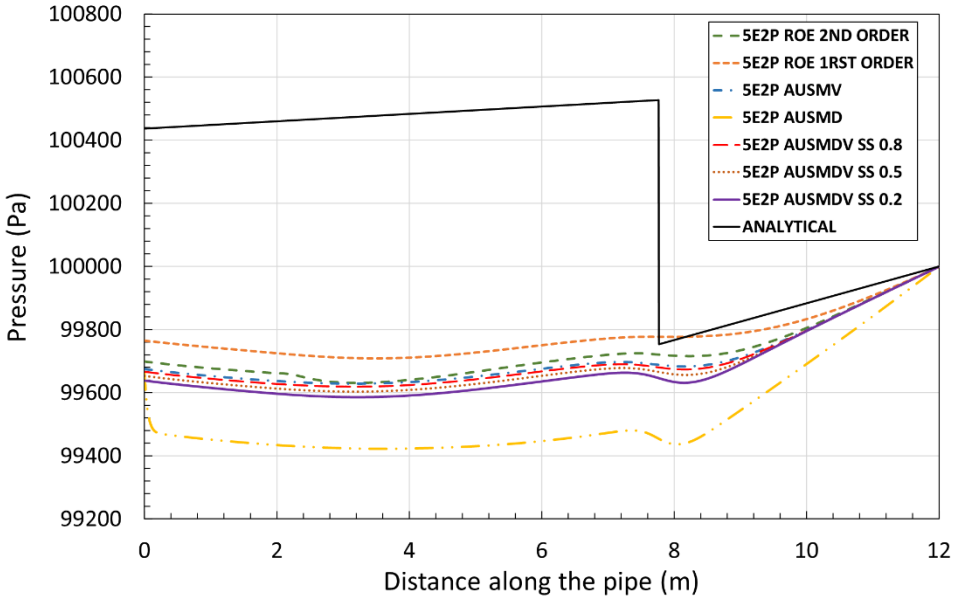

Figure 17: Pressure distribution along the line for the 5E2P model for the water faucet problem at t=0.6s.

Figures 14 to 17 present graphs for the void fraction, liquid and gas velocities, and pressure respectively, plotted against the distance along the pipe and compared to the analytical solution. In Fig. 14, the void fraction graph shows the discontinuity at time 0.6s. The initial condition is propagated along the line downstream of the discontinuity, separating this part of the flow from the upstream flow that seeks to accommodate in a steady-state condition. As the liquid is accelerated due to the action of gravity, as shown in Fig. 15, the liquid holdup decreases to conserve mass and, therefore, the void fraction increases upstream of the discontinuity. Again, in order to conserve mass, gas flows from the outlet towards the inlet (Fig. 16). This expected behavior can be verified in Fig. 16, where the gas velocity is negative downstream of the discontinuity. The pressure distribution, on the other hand, shows a hydrostatic increase downstream of the discontinuity and a smoother increase upstream of the discontinuity, as depicted in Fig.17, due to the gas phase. Even though there are small discrepancies in the pressure results, they are explained by the differences that exist in the model and in the assumptions made to get the analytical solution. It is worth mentioning that the differences are very small, representing 1% relative error for the AUSMD (furthest curve) in comparison with the analytical solution in the highest pressure value upstream of the discontinuity.

The same study was performed with the 7E2P model in combination with the previously mentioned numerical methods. For the 7E2P model, two more variables need specification: the bubbles and droplets volume fraction. These variables are set at the inlet

as boundary conditions and are equal to 10^{-7}, which means that small concentration of bubbles and droplets are being considered, and similar results from the 5E2P model are expected. The results are displayed in the form of graphs, according to Figs. 18 to 21.

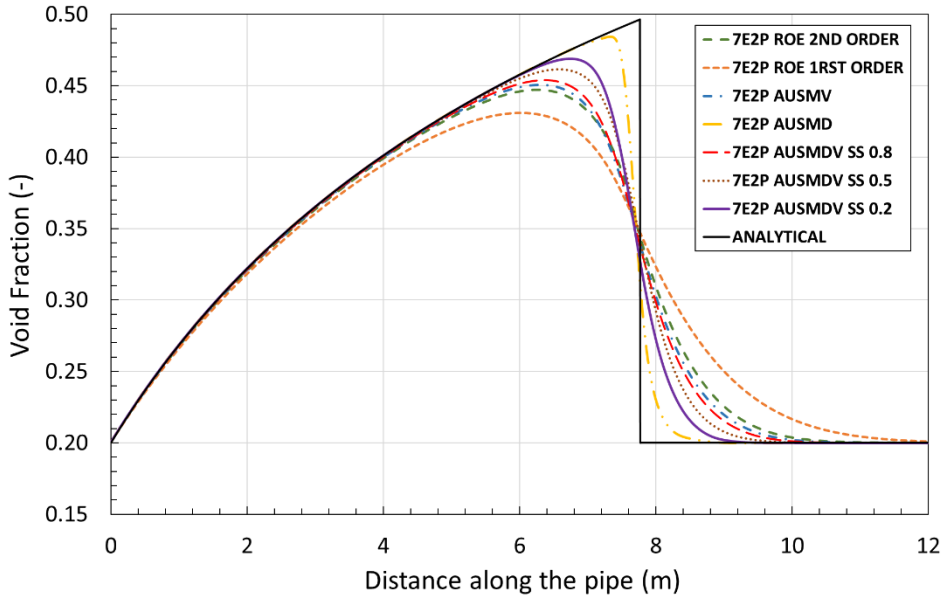

Figure 18: Void fraction distribution along the line for the 7E2P model for the water faucet problem at t=0.6s.

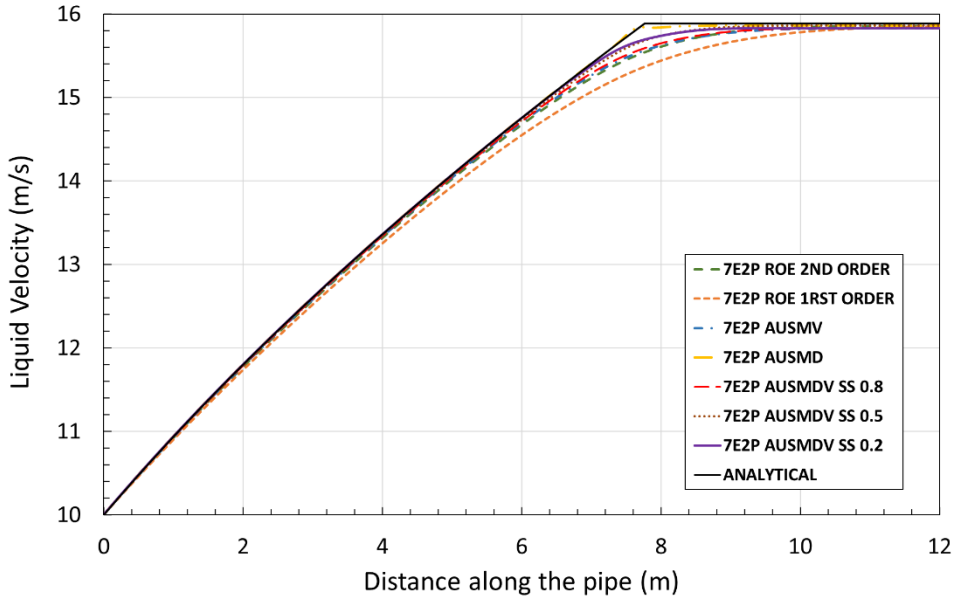

Figure 19: Liquid velocity distribution along the line for the 7E2P model for the water faucet problem at t=0.6s.

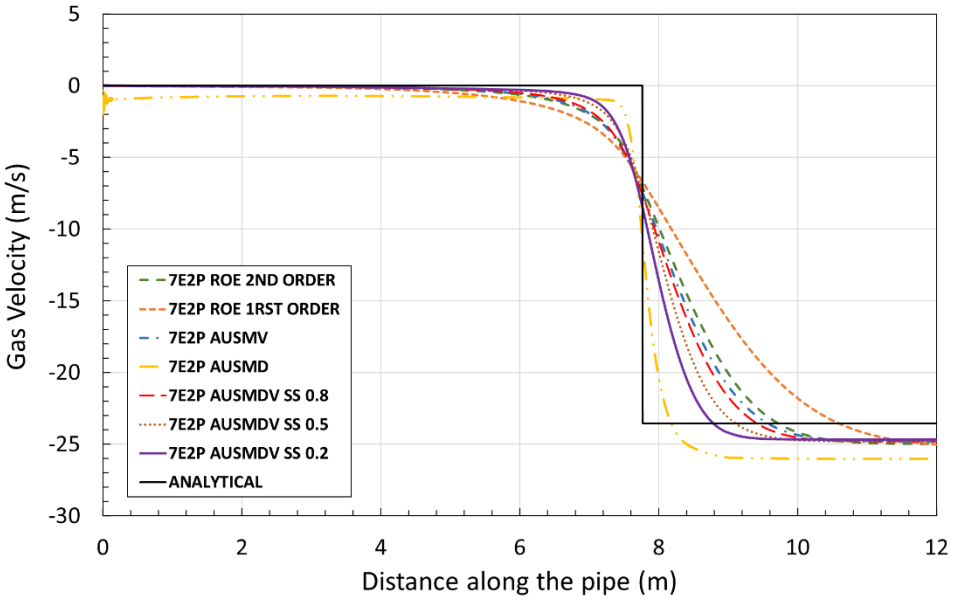

Figure 20: Gas velocity distribution along the line for the 7E2P model for the water faucet problem at t=0.6s.

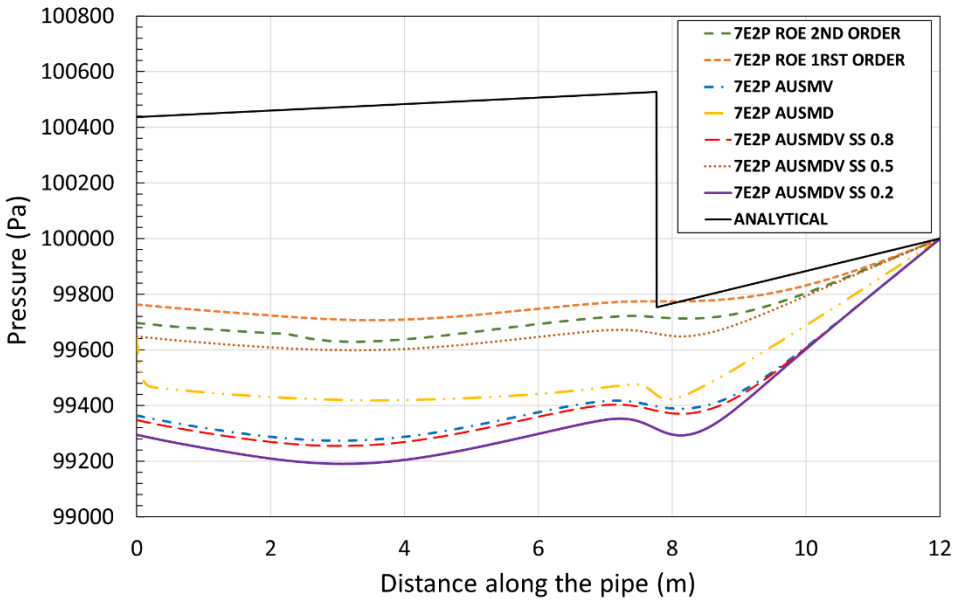

Figure 21: Pressure distribution along the line for the 7E2P model for the water faucet problem at t=0.6s.

Since the bubbles and droplets volume fraction are small, similar results to the 5E2P model are expected and the same conclusions can be inferred. Regarding the numerical method comparison, the AUSMD seems to have the better agreement with the analytical solution, if the void fraction plot is considered. However, oscillations appear close to the inlet due to numerical dispersion, as can be verified in gas velocity graphs previously presented. The AUSMV solution is smooth and numerical oscillations were not observed.

The AUSMDV method, approaching the AUSMV tends to be smoother, for instance AUSMDV with *ss* = 0.5 or 0.8. The closer to the AUSMD method, more accurate seems to be the solution for the void fraction, however, the observed dispersive behavior near the inlet may cause numerical issues when used in the slug capturing simulations, whereas the smother ones can be a better alternative.

6.1.2 The Shock Tube Problem: The Large Relative Velocity

The large relative-velocity shock tube problem is a classic numerical test that was also investigated by many authors, such as Evje and Flätten (2003) and Ferrari *et al*. (2017). It consists of an initial-value problem in the presence of a discontinuity and is appropriate to determine the capability of the numerical technique to deal with initial-value problems that are suddenly imposed to a different state. For this case, the discontinuities are located at the middle of the pipe and they are associated with the gas velocity and the volume fraction. The simulations are carried out with a large relative velocity between phases at the left and right of the discontinuity, as detailed in Table 6, and the simulation set up is described in Table 7. This benchmark problem also has no friction terms.

Table 6: Initial condition for the large relative-velocity shock tube benchmark.

Flow Variable	Value
p - at left	265000 Pa
u_G - at left	65 m/s
u_L - at left	1 m/s
α_G - at left	0.29 (-)
p - at right	265000 Pa
u_G - at right	50 m/s
u_L - at right	1 m/s
α_G - at right	0.3 (-)

Table 7: Simulation set up for the large relative velocity shock tube benchmark.

Constant	Value
Pipe length	100 m
Sound speed in the liquid	1000 m/s
Sound speed in the gas	316.2 m/s
Reference gas density	0 kg/m³
Reference liquid density	1000 kg/m³
Discontinuity initial location	50 m
Pipe inclination	0 º
Time (snapshot)	0.1 s
CFL number (AUSM-type/Roe)	0.45/0.9
Mesh size	2000 cells

For the large-relative velocity shock tube problem, the same values for the tuning parameter, *ss*, of the AUSMDV method is used. The following graphs show a comparison of the results of the numerical simulation with the reference solution of Evje and Flätten (2003), which is also a numerical since there is no analytical solution for the shock tube problem in two-phase isothermal flow. Figure 22 shows the liquid volume fraction plot at t=0.1s.

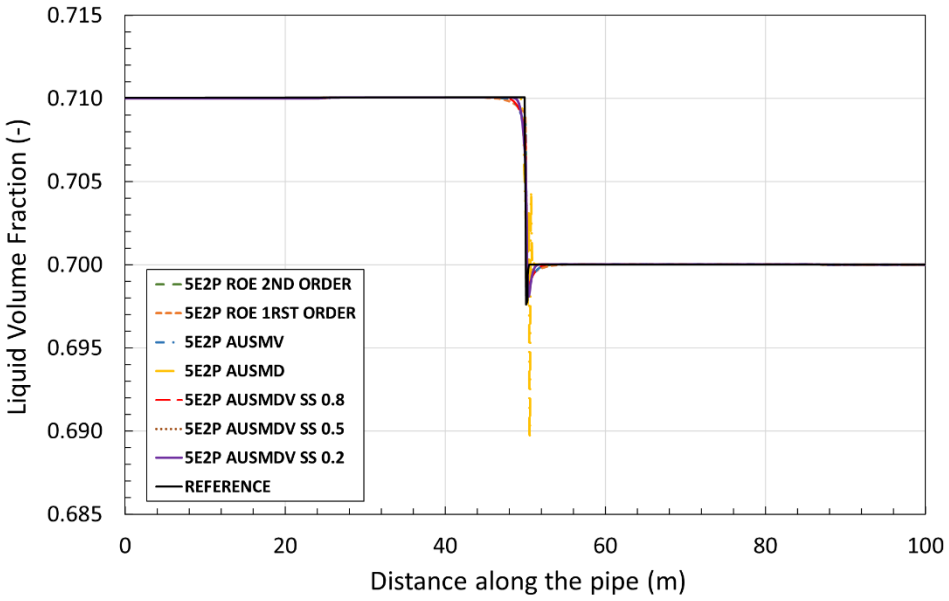

Figure 22: Liquid volume fraction (holdup) distribution along the line for the 5E2P model for the shock tube problem at t=0.1s.

The AUSMD solution presents overshoots due to dispersive behavior in the vicinity of the discontinuity. Removing the AUSMD result from the holdup plot and reducing the x-axis scale, Fig. 23 is obtained.

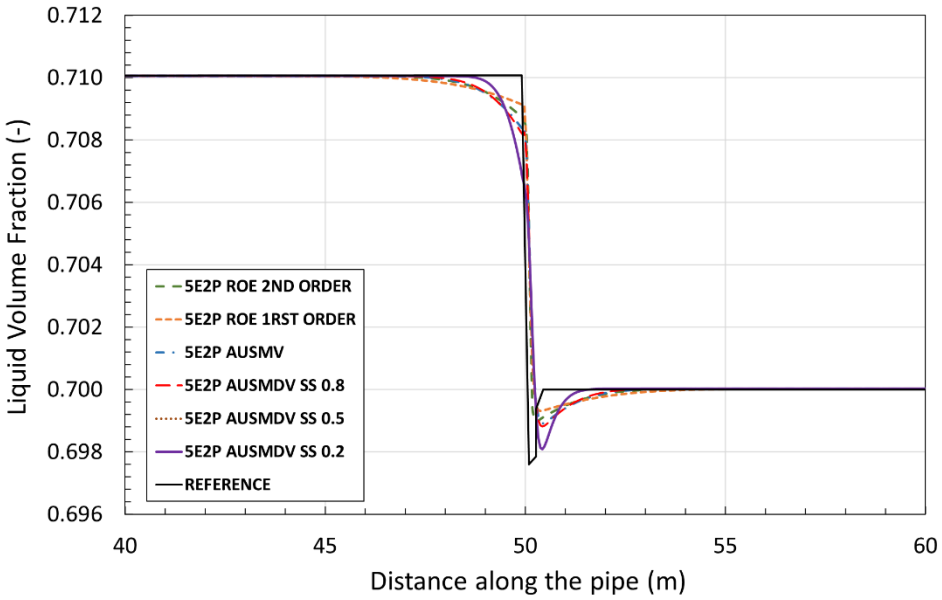

Figure 23: Eliminating AUSMD solution and amplifying x-axis scale for the liquid volume fraction (holdup) distribution along the line for the 5E2P model for the shock tube problem at t=0.1s.

The liquid velocity plots are presented in Figs. 24 and 25, removing the solution with AUSMD in the last one.

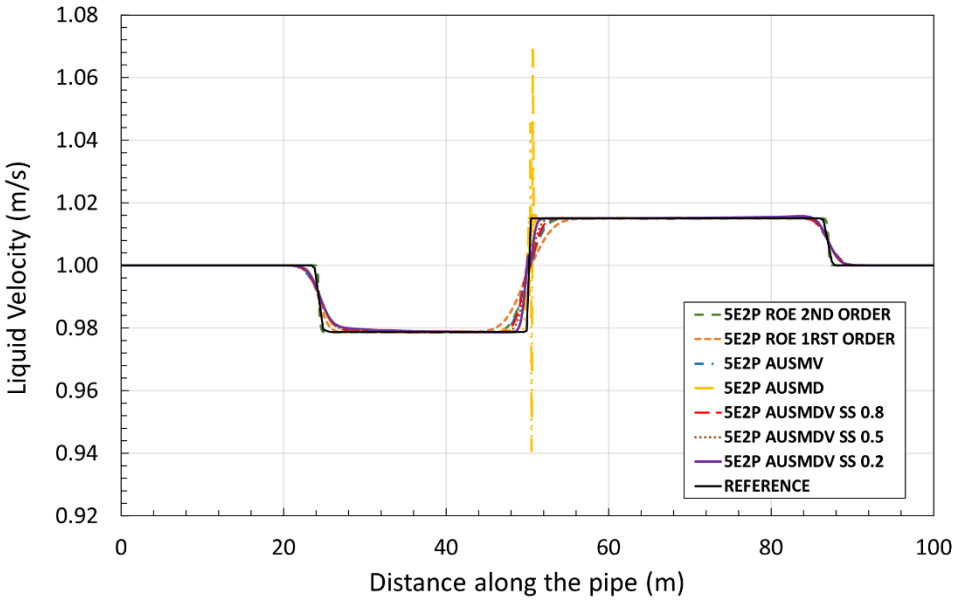

Figure 24: Liquid velocity distribution along the line for the 5E2P model for the shock tube problem at t=0.1s.

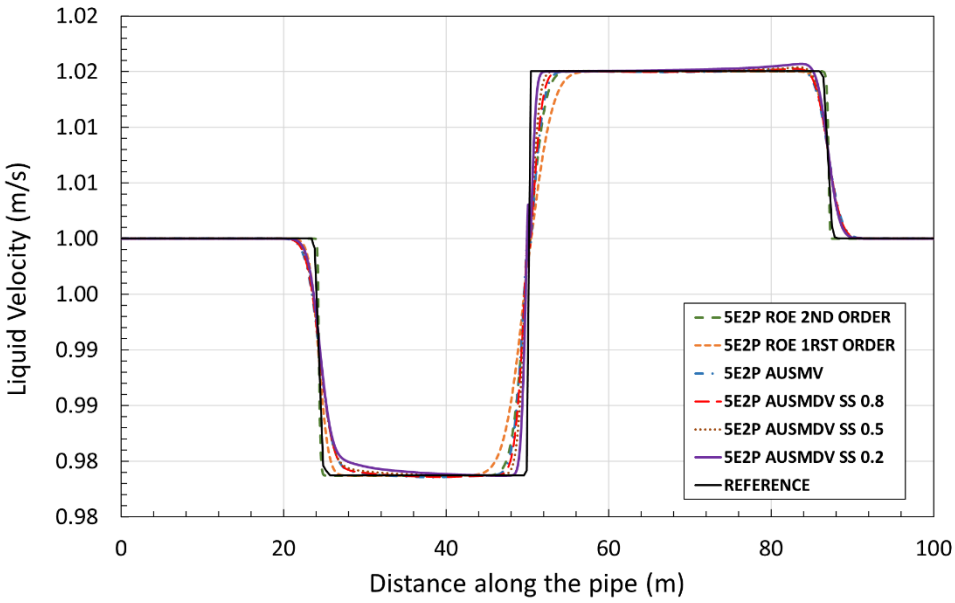

Figure 25: Eliminating AUSMD solution and amplifying x-axis scale for the liquid velocity distribution along the line for the 5E2P model for the shock tube problem at t=0.1s.

The gas velocity and the pressure are depicted in Figs. 26 and 27, as follows

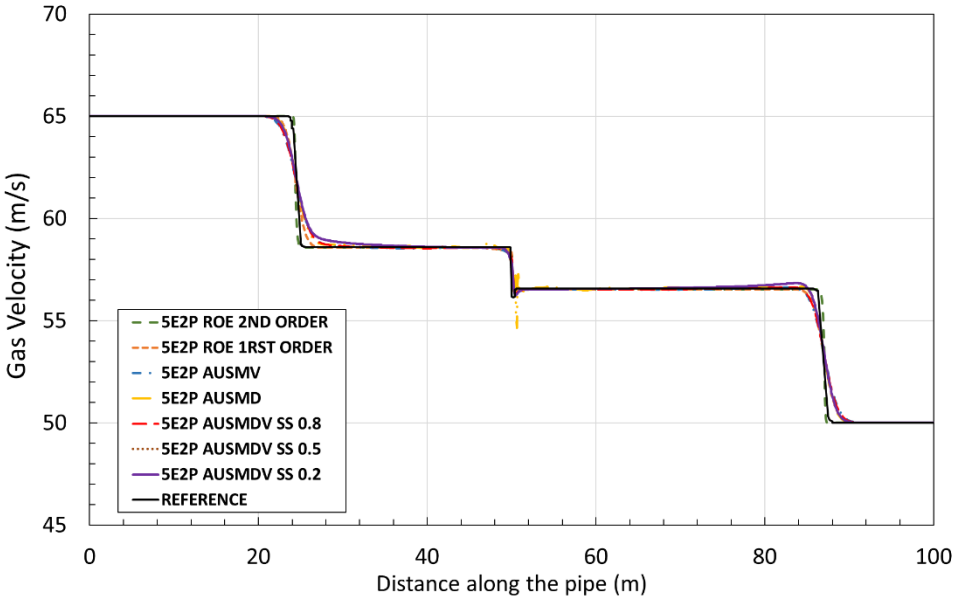

Figure 26: Gas velocity distribution along the line for the 5E2P model for the shock tube problem at t=0.1s.

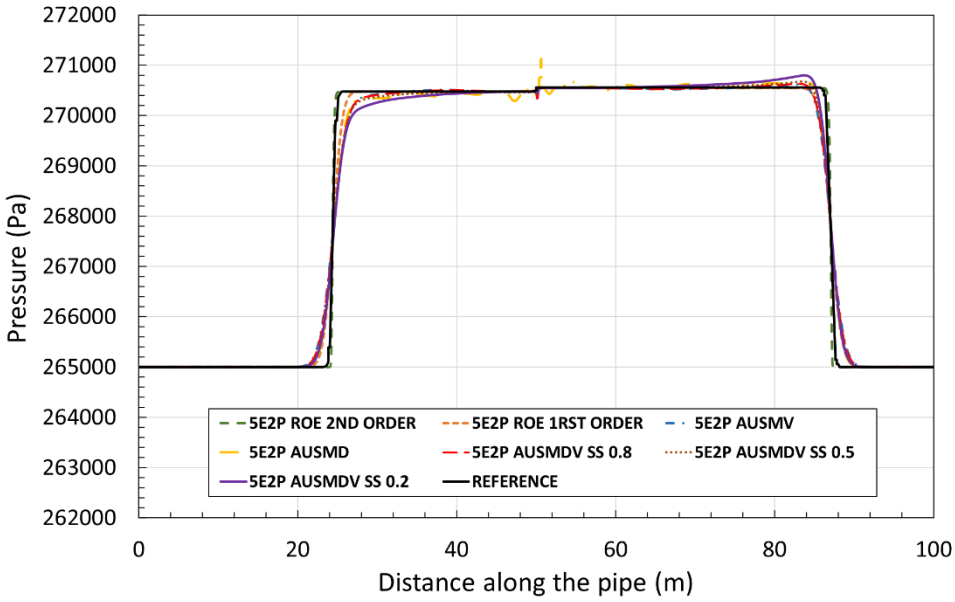

Figure 27: Pressure distribution along the line for the 5E2P model for the shock tube problem at t=0.1s.

Despite the result with AUSMD method, that presents a dispersive behavior in the region close to the discontinuity, those graphs reveal how well the AUSMV, AUSMDV and Roe numerical approaches succeed in correctly reproducing the expected physical behavior of the flow in the presence of sharp gradients and discontinuities. As previously observed for the water faucet problem, as close the AUSMDV method gets to the AUSMD (smaller *ss* value), more dispersion in introduced in the solution.

For the shock tube problem, the 7E2P model in combination with the numerical methods is simulated and the results for holdup, liquid velocity, gas velocity and pressure are presented in Figs. 28 to 33, respectively. Once again, two more variables need specification: the bubbles and droplets volume fraction. These variables are set at the inlet as boundary conditions and are equal to 10^{-7} getting similar results if compared to the 5E2P model. Figures 29 and 31 are the plots for holdup and liquid velocity without the AUSMD method in order to eliminate the dispersive solution and the x-axis has a zoomed scale for the first one.

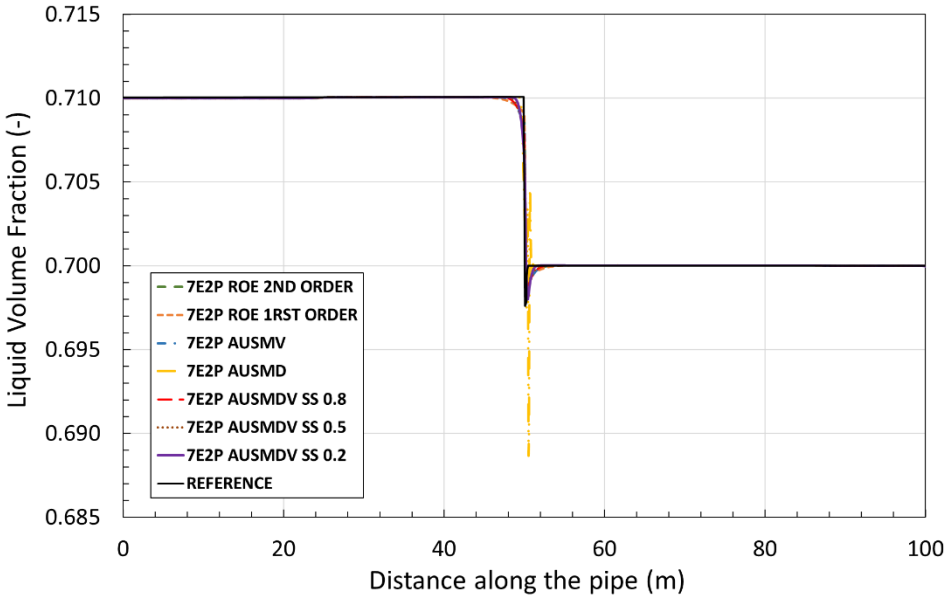

Figure 28: Liquid volume fraction (holdup) distribution along the line for the 7E2P model for the shock tube problem at t=0.1s.

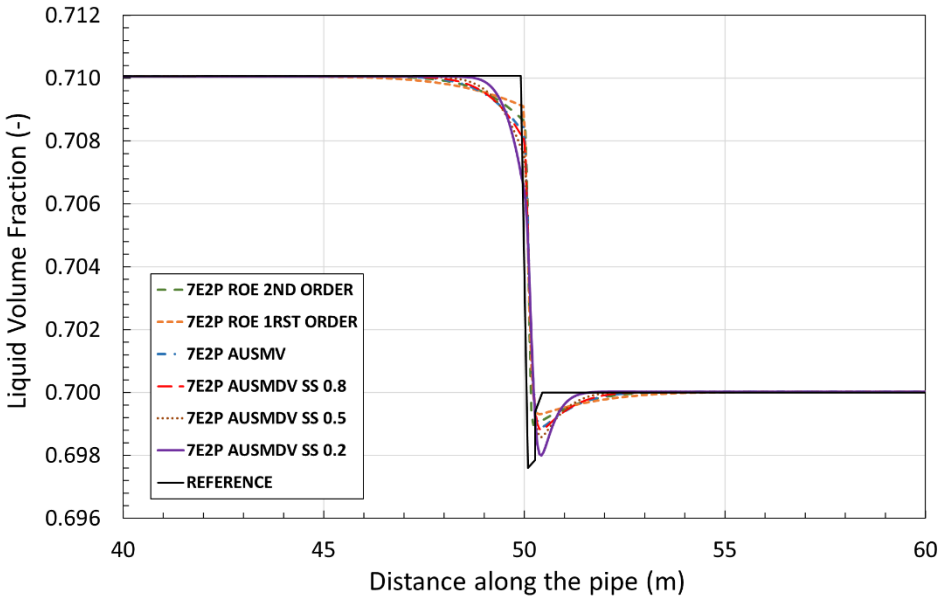

Figure 29: Eliminating AUSMD solution and amplifying x-axis scale for the liquid volume fraction (holdup) distribution along the line for the 7E2P model for the shock tube problem at t=0.1s.

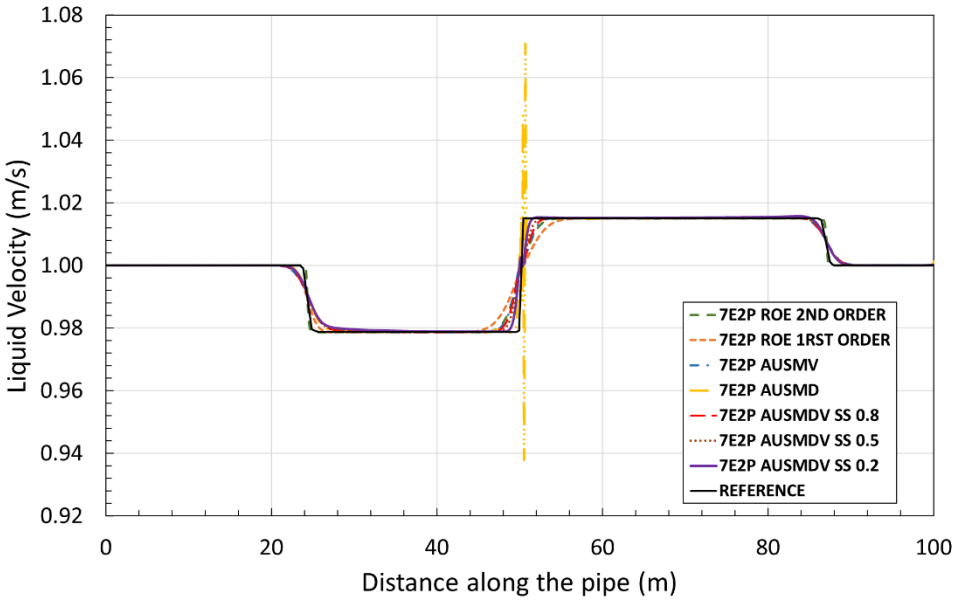

Figure 30: Liquid velocity distribution along the line for the 7E2P model for the shock tube problem at t=0.1s.

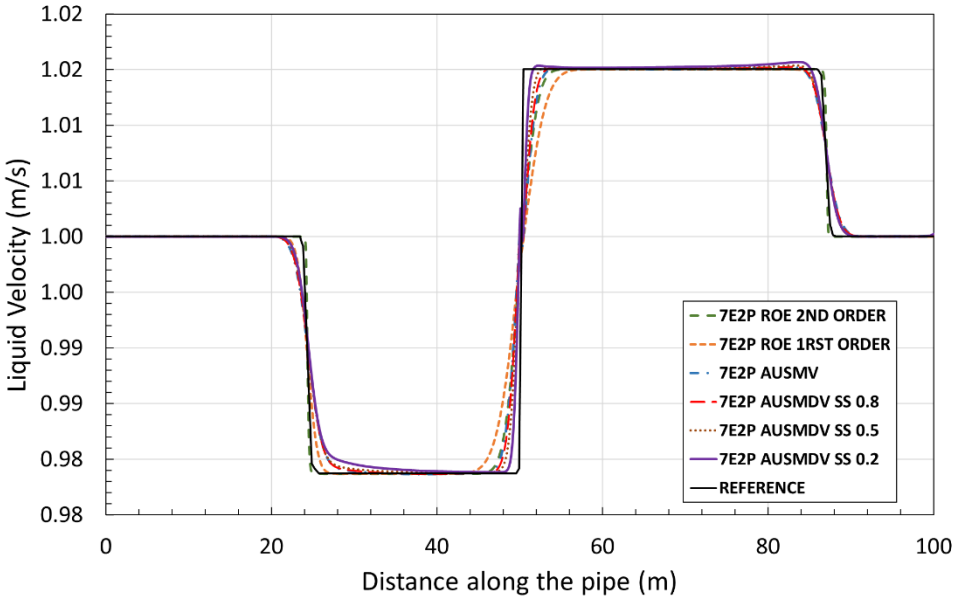

Figure 31: Eliminating AUSMD solution and amplifying x-axis scale for the liquid velocity distribution along the line for the 7E2P model for the shock tube problem at t=0.1s.

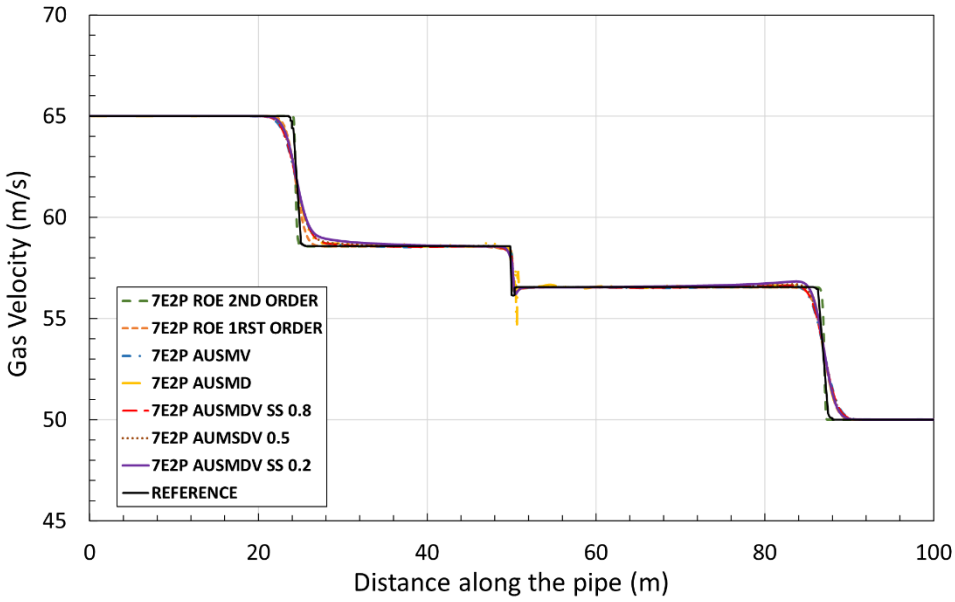

Figure 32: Gas velocity distribution along the line for the 7E2P model for the shock tube problem at t=0.1s.

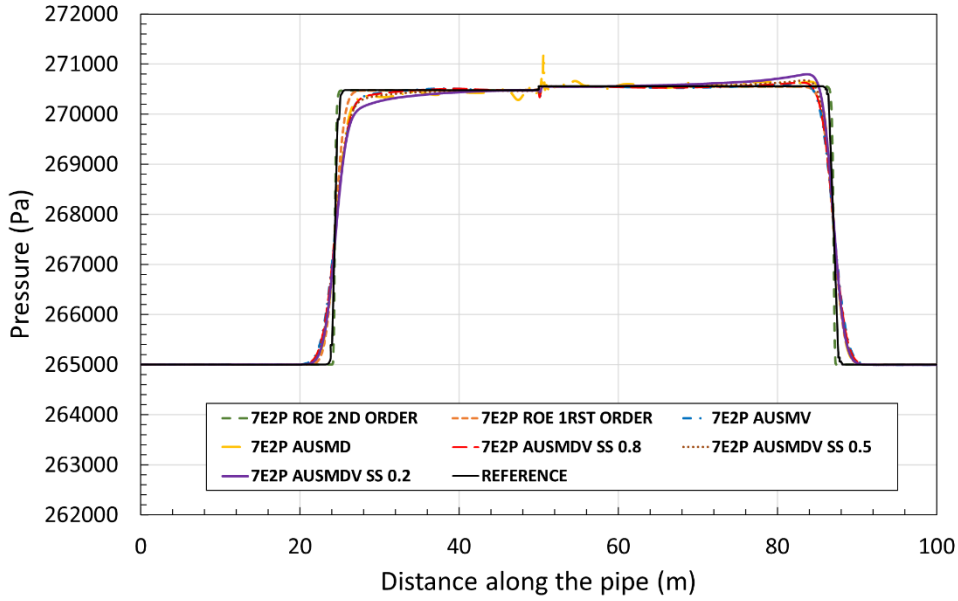

Figure 33: Pressure distribution along the line for the 7E2P model for the shock tube problem at t=0.1s.

It can be inferred from the results that all the numerical methods and mathematical models presented good results for the benchmark problems so far studied. The Roe method and the AUSM-type of methods are accurate and successfully represented the proposed problems. The AUSMDV deserves a more detailed study regarding the tuning parameter, *ss*. Thus, the next benchmark problem is run to better understand the impact that this parameter has in the solution.

6.1.3 The Separation Problem

This benchmark problem was described in Coquel *et al*. (1997) and it consists of a vertical pipe that is closed at both ends. In this problem, there is no wall and interfacial friction forces, and the flow is treated as isothermal. Figure 34(a) illustrates the initial condition, in which the pipe is filled uniformly with liquid and gas and all the flow variables are equal and constant in all the domain. With the gravitational effect, the fluids tend to go separate ways, as can be seen in a snapshot in time in Fig. 34(b): the liquid accumulates at the bottom of the pipe and the gas, in the upper part. When both fluids are completely separated, as represented by Fig. 34(c), the steady state is reached.

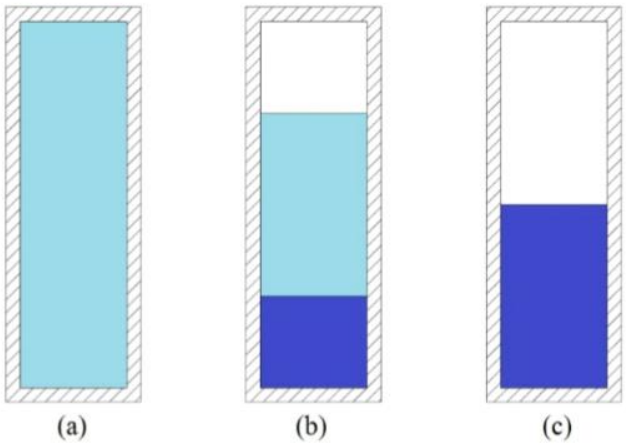

Figure 34: Separation problem schematic. (a) Initial uniform condition. (b) Flow snapshot sometime between initial and steady-state condition. (c) Steady-state condition.

The pipe configuration for this problem is described in the following Table 8.

Table 8: Simulation set up for the separation benchmark.

Configuration	Value
Fluids	Water and Air
Pipeline Length	7.5 m
Liquid Reference Density	1000 kg/m³
Speed of Sound in Liquid	1000 m/s
Speed of Sound in Gas	316.2 m/s
Reference gas density	0 kg/m³
Reference liquid density	1000 kg/m³
CFL number (AUSM-type/Roe)	0.45/0.9
Mesh size	2000 cells
Initial gas velocity	0 m/s
Initial liquid velocity	0 m/s
Initial holdup	0.5 (-)

The expected behavior for this problem at the steady state condition is to have both fluids separated, which means that the liquid volume fraction has the value of one from the middle to the bottom of the pipe, and zero from the top to the middle of the pipe due to the gas presence in this region. The pressure profile at the steady state should present an increase in the liquid region since the hydrostatic column has an effect in the pressure.

The results for the flow variables at the steady-state condition with the 5E2P model are displayed in Figs. 35 and 36. It is worth mentioning that the simulations of the separation problem with the AUSMD method could not be performed, since the dispersion took over the solution. In addition, with the Roe method, the dispersion close to the discontinuity was also an issue, presenting overshoots when the holdup value approached one. To be able to get a solution with this method, the CFL number had to be very small and some artificial control to keep the holdup value lower than one was needed. The artificial limitation consisted in recalculate all the flow variables, in every time the holdup value passed unity, based on the holdup limit number, implying in violation of mass conservation. Hence, the solution with Roe is not presented in the following graphs. As the AUSMDV ss=0.2 is closer to the AUSMD than the AUSMV, it presented very dispersive behavior in the pressure variable, compromising the solution, therefore, it is also not illustrated in the pressure graph.

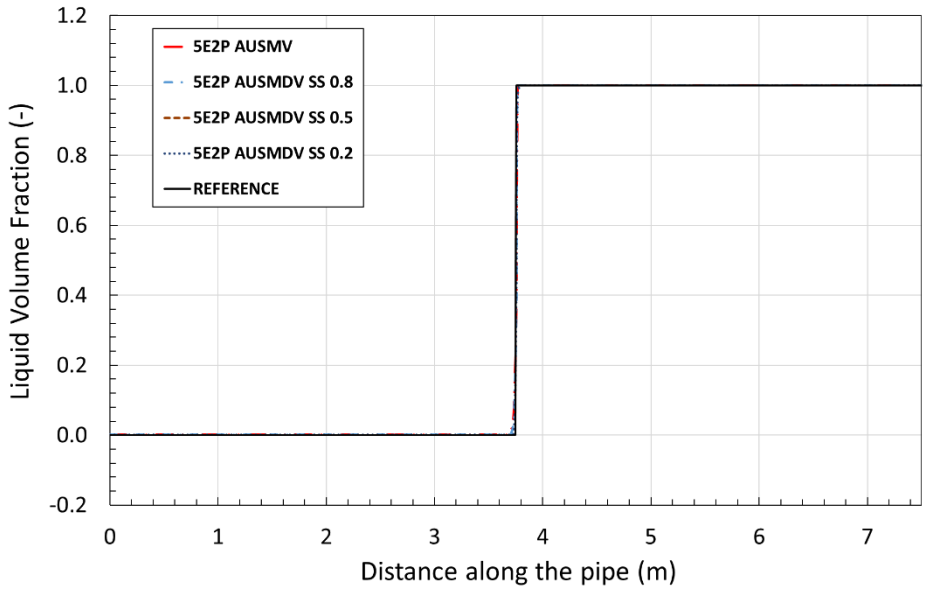

Figure 35: Liquid volume fraction (holdup) distribution along the line for the 5E2P model for the separation problem in the steady state.

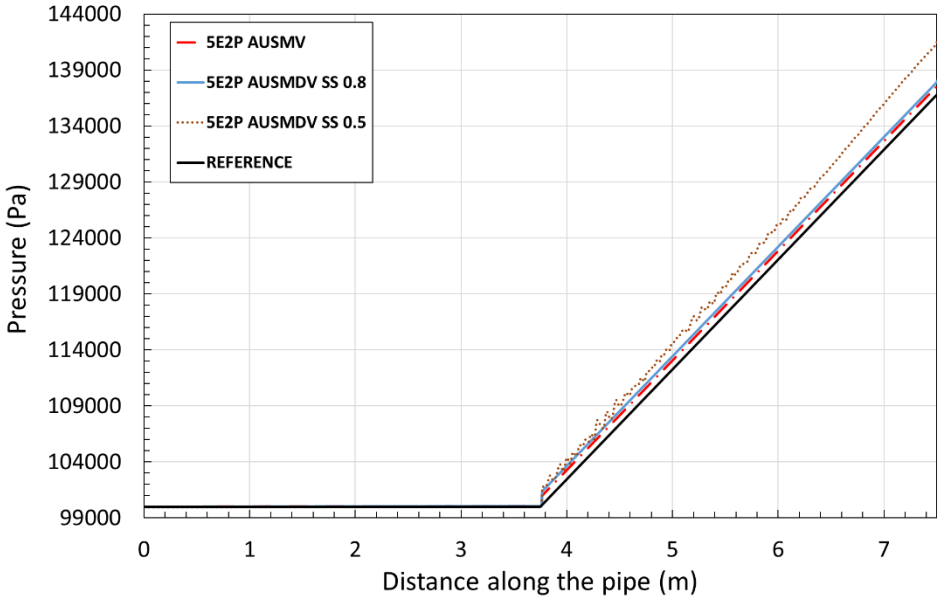

Figure 36: Pressure distribution along the line for the 5E2P model for the separation problem in the steady state.

It can be observed from the pressure result that the simulation using AUSMDV with *ss*=0.5 shows evidence of the initiation of the dispersive effect. The numerical results for the liquid volume fraction indicate that the gas is occupying the top part of the pipe and the liquid is accumulating in the bottom, as expected. As for the pressure distribution along the line, it has an increase downstream of the discontinuity, indicating the presence of the liquid in this region and, consequently, the hydrostatic column addition in the pressure.

The same simulations were performed with the 7E2P mathematical model in combination with the numerical technique that are being studied in this work, and the results are exhibited in Figs. 37 and 38.

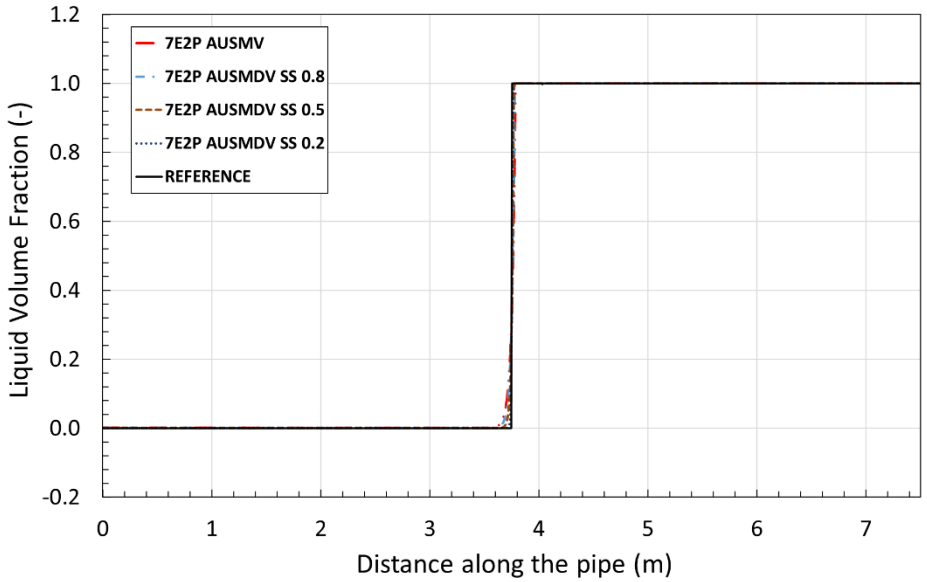

Figure 37: Liquid volume fraction (holdup) distribution along the line for the 7E2P model for the separation problem in the steady state.

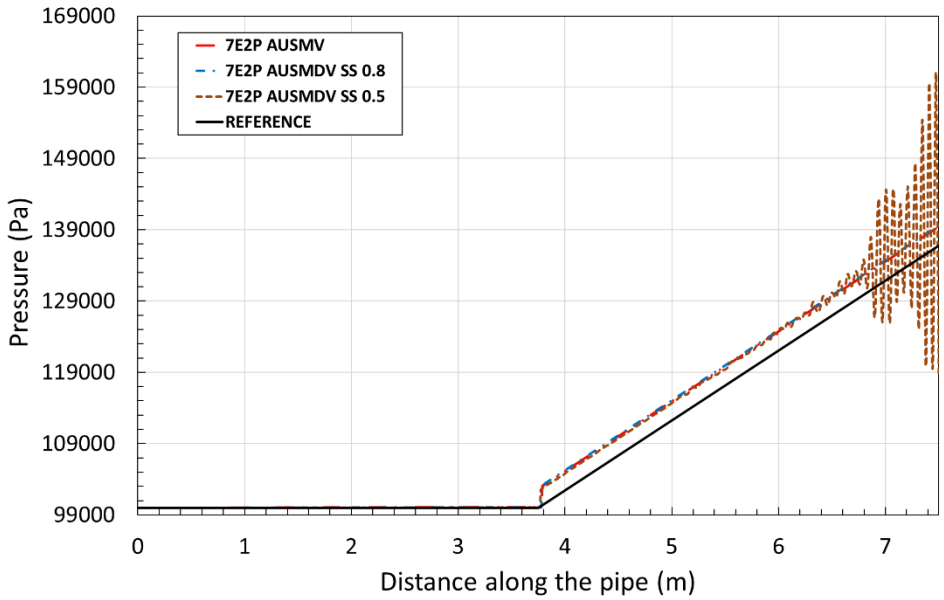

Figure 38: Pressure distribution along the line for the 7E2P model for the separation problem in the steady-state.

Analyzing the results of these numerical simulations we may conclude that the AUSMV and AUSMDV methods are the ones that best represented the expected solution for both flow variables: liquid volume fraction and pressure. As the AUSMDV numerical technique approaches the AUSMD method, the simulation gets chaotic due to dispersion and as the AUSMDV method goes towards the AUSMV method, the solution is smoother.

The solution using AUSMDV *ss*=0.8 was the most successful one for both mathematical models, extracting the best effects in the balance between the AUSMV and AUSMD.

The benchmark problems simulations were especially important in guiding the choice of the best mathematical model and numerical method combination. The presence of the discontinuity in all flow scenarios was crucial to identify the behavior of each model and method combination in solving the equations. For the slug capturing simulations, a robust and accurate method is desired, as well as generality of implementation and simplicity. In a general analysis, the AUSMDV *ss*=0.8 was the one that better matched the expectations. The results are very impressive, there is no need for characteristic analysis and the computational time is reduced if compared to the Roe method. In consonance with the benchmark study, the AUSMDV method is the most promising one to be used for the slug capturing simulations.

6.2 Accuracy Check of the Numerical Method

The accuracy check of the numerical method AUSMDV *ss*=0.8 is performed based on the simulation of a stratified flow scenario, in which a steady state can be achieved. For the intermittent flow pattern, the steady state is statistical, where the flow variables remain changing in time intermittently. In addition, the slug capturing simulations require more time, which would make the simulations with the refined meshes more computational demanding.

The accuracy study has the objective to determine whether the method is first or second order accurate in space and its relationship with the mesh discretization. For that, the same code was used for different mesh sizes, Δx, keeping the same Δt for all of them. For each different Δx, the CFL number changes, obeying the stability criterion for explicit discretization.

The accuracy analysis is based on the calculation of a global flow variable, the total momentum integrated along the domain, which combines all flow variables in one. The relative error is calculated according to

$$\xi = \frac{\left|P - P_{ref}\right|}{P_{ref}}, \tag{6.5}$$

where P_{ref} is the momentum value for the most accurate result, which means the momentum result obtained with the smallest Δx corresponds to the most refined mesh. For this study, results are obtained for 10000, 5000, 2000, 1000, 500 and 100 cells of discretization. The most refined mesh is 10000 cells, $\Delta t = 0.002025s$ for all the simulations and the 5E2P model was used. The initial and boundary conditions of this stratified case is presented in Table 10, and the pipeline configuration in Table 9, representing the simulation case described in Figueiredo *et al.* (2017). Holdup and fluids velocities are prescribed at the inlet and the fluids pressures are prescribed at the outlet as boundary conditions.

Table 9: Flow configuration for the study of the numerical method's accuracy.

Configuration	Value
Fluids	Oil and Gas
Pipeline Length	45 km
Internal Diameter	0.45 m
Pipeline Roughness	4.57 x 10^{-5} m
Liquid Reference Density	720 kg/m³
Speed of Sound in Liquid	900 m/s
Speed of Sound in Gas	350.9 m/s
Liquid Viscosity	4.4 x 10^{-4} Pa.s
Gas Viscosity	1.3 x 10^{-5} Pa.s
Temperature	293 K

Table 10: Inlet and outlet boundary conditions for the study of the numerical method's accuracy.

Flow Variable	Value
p at outlet ($x=L$)	6 MPa
u_G at *inlet* ($x=0$)	4.08 m/s
u_L at *inlet* ($x=0$)	1.24 m/s
α_L at *inlet* ($x=0$)	0.088 (-)

The following figure, Fig. 39, represents the relative error as a function of the dimensionless number, $\Delta x/L$, where L is the pipeline length. It is worth mentioning that

this analysis was also performed for the 7E2P model and the results obtained are remarkably similar and graphically, there is no difference between the curves.

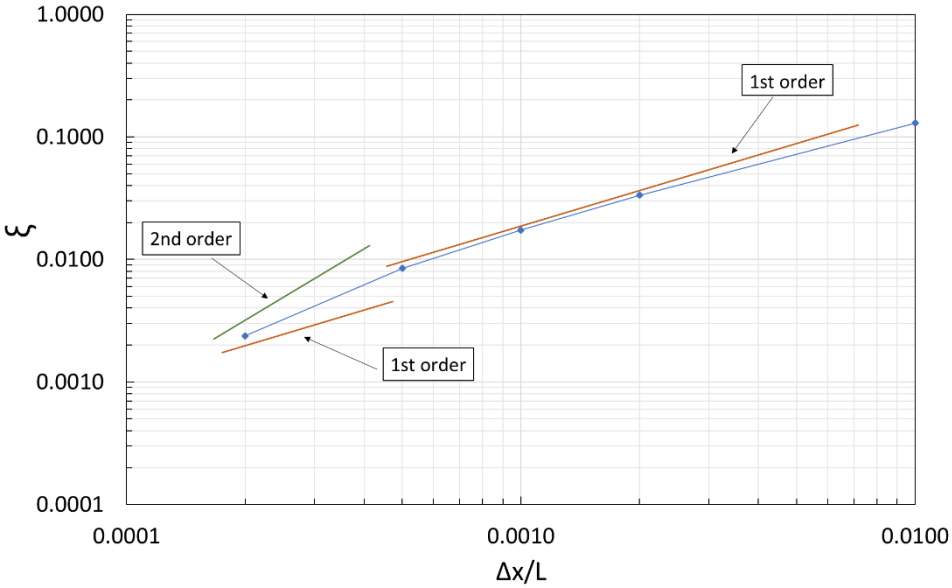

Figure 39: Relative error in the total momentum integrated along the pipeline as a function of $\Delta x/L$ for the AUSMDV *ss*=0.8 using 5E2P.

The colored lines that appear in Fig. 39, brown and green, correspond to a first and second order accuracies, respectively, and are indicated to assist the identification of the error on a log-log plot. The results reveal that the numerical method AUSMDV behaves as first-order accurate.

The same analysis was made for the AUSMV method, for the sake of curiosity, combined with 5E2P and 7E2P models to check if there is any major difference between the two numerical techniques in terms of order of accuracy in space. The results obtained show that both techniques have the same order of accuracy, presenting relative error as a function of the dimensionless number, $\Delta x/L$, with the same slope, as can be seen in Fig. 40 where the comparison is made with the 5E2P model. Once again, it is important to point out that the accuracy check of the AUSMV with the 7E2P model was also performed and returned similar results.

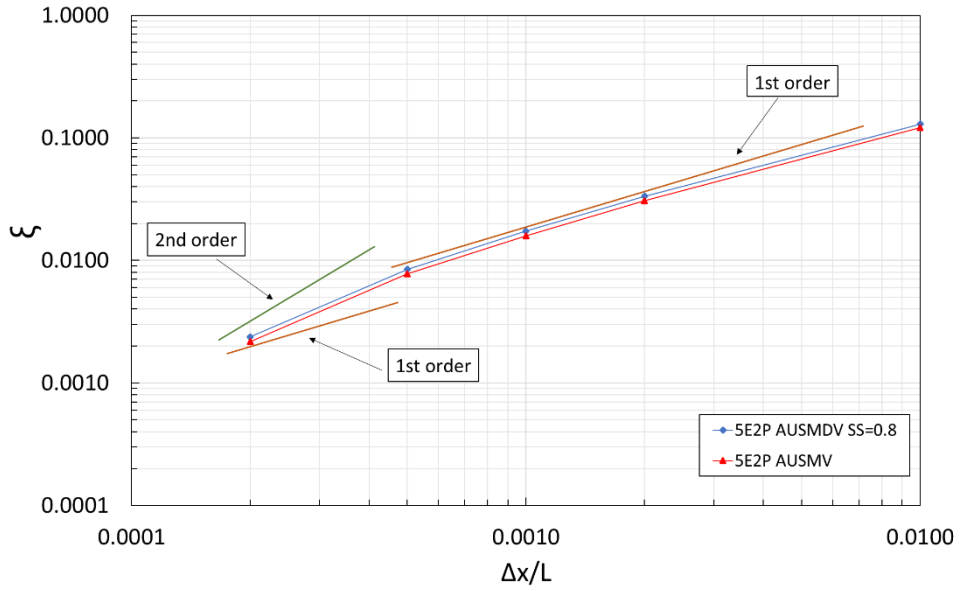

Figure 40: Relative error in the total momentum integrated along the pipeline as a function of $\Delta x/L$ for the AUSMV in comparison with AUSMDV ss=0.8 using 5E2P.

7 Numerical Results for Intermittent Flow

In this chapter, numerical simulations of intermittent two-phase flow are presented. First, a slug capturing simulation reported in the literature is performed in order to test the numerical model and check its ability to predict the transition from stratified to slug flow as a natural development of the flow. Then, experimental data that were obtained in the experimental campaign carried out at The University of Tulsa (Tulsa, Oklahoma, USA) is used as validation of the numerical model herein proposed herein.

7.1 Comparison with Literature Results

In the work of Ferrari *et al.* (2017), a simulation of slug formation and evolution is performed to verify the ability of the numerical code to predict the flow pattern transition. They employed a mathematical model comprised of five governing equations and two pressures, the 5E2P, in association with the Roe scheme. Inspired by this work, numerical simulations were run with the 5E2P and 7E2P models, combined with the AUSMDV numerical method, and the results were compared to the numerical results of Ferrari *et al.* (2017). Since Ferrari *et al*. (2017) used the Roe method in their simulations, simulations with the Roe method were also carried out and the results are also presented for this test case. The setup of the simulations is detailed in Table 12, and the boundary conditions that were prescribed for this test case are presented in Table 11.

Table 11: Inlet and outlet boundary conditions for the slug formation and evolution. Comparison with Ferrari *et al.* (2017).

Flow Variable	Value
p at outlet ($x=L$)	10^5 Pa
u_G at *inlet* ($x=0$)	4 m/s
u_L at *inlet* ($x=0$)	3 m/s
α_G at *inlet* ($x=0$)	0.5 (-)

Table 12: Flow configuration for slug formation and evolution. Comparison with Ferrari *et al.* (2017).

Configuration	Value
Fluids	Water and Air
Pipeline Length	36 m
Internal Diameter	0.078 m
Pipeline Roughness	3.4×10^{-5} m
Liquid Reference Density	1000 kg/m³
Speed of Sound in Liquid	1000 m/s
Speed of Sound in Gas	316.2 m/s
Liquid Viscosity	1.14×10^{-3} Pa.s
Gas Viscosity	1.79×10^{-5} Pa.s
CFL number (AUSM-type/Roe)	0.1/0.9
Mesh size	2000
Time (Snapshot)	8s

The graphs displayed in Figs. 41 to 44 present the results of the simulation with the 5E2P model, at t=8s, for all the flow variables: holdup, gas and liquid velocities, and pressure, respectively.

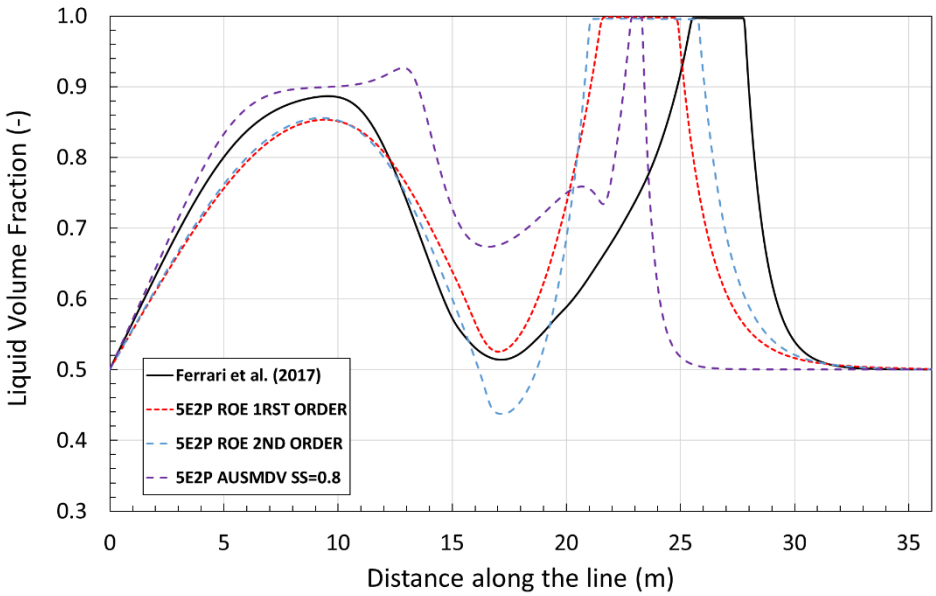

Figure 41: Liquid volume fraction distribution along the line for the 5E2P model for the slug formation and evolution test case at t=8s.

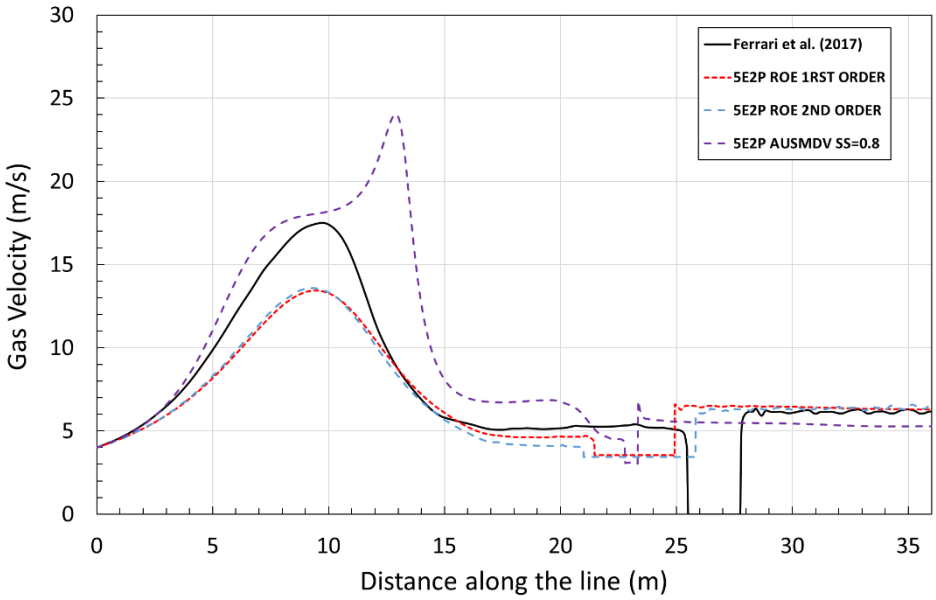

Figure 42: Gas velocity distribution along the line for the 5E2P model for the slug formation and evolution test case at t=8s.

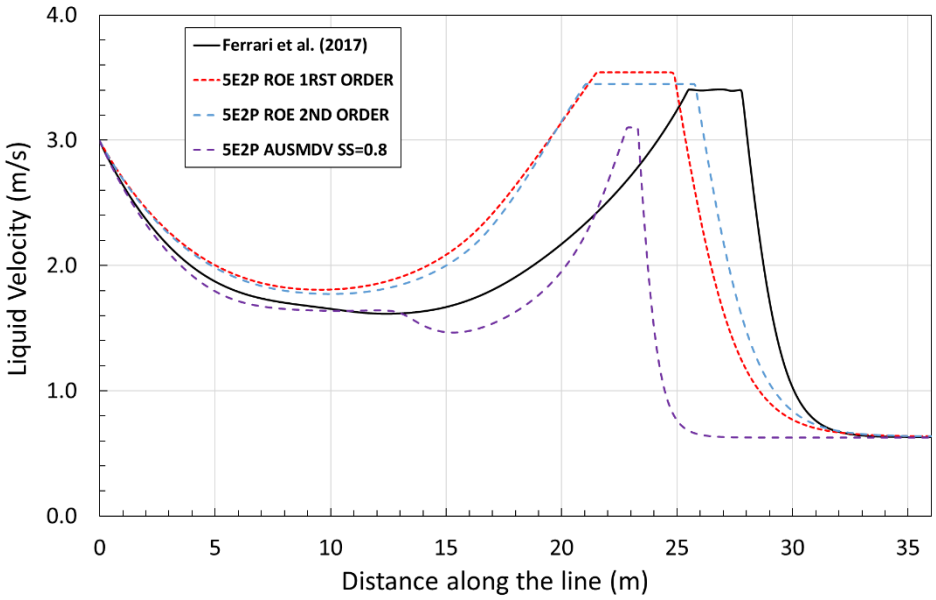

Figure 43: Liquid velocity distribution along the line for the 5E2P model for the slug formation and evolution test case at t=8s.

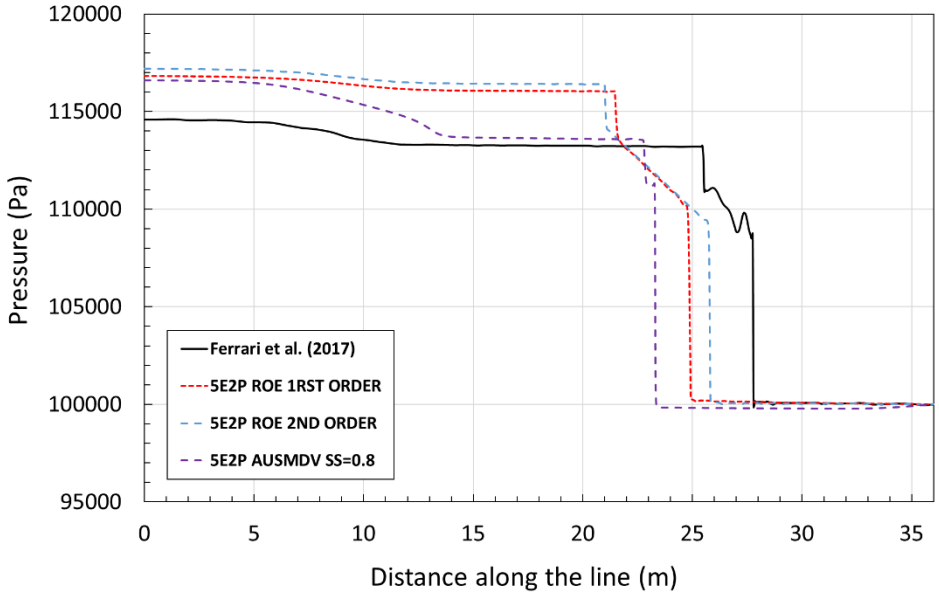

Figure 44: Pressure distribution along the line for the 5E2P model for the slug formation and evolution test case at t=8s.

From those graphs, it can be noticed that all the numerical models were able to generate the slug flow from the stratified flow. Moreover, the physics is well represented, since when the slug is formed, the pipe cross section area is filled with liquid and the gas volume fraction approaches the value of zero. In summary, the results show that, when the slug starts to form at the beginning of the pipe, the holdup increases and, to conserve mass, the liquid velocity decreases, followed by an increase of the gas velocity. The pressure in this region decreases slowly due to friction. Downstream of this slug initiation region, the holdup decreases and then increases again to start another slug-formation wave. As a consequence, a full slug region is generated, where the holdup approaches unity. In this slug region, the liquid velocity increases and the slug accelerates, due to the large pressure difference in the slug body that balances the high friction on the wall. On the other hand, because the void fraction goes to zero in the slug region, the gas tends to accelerate in a non-physical manner. To control this unrealistic effect, the velocity relaxation procedure is applied during the simulation, as explained in chapter 4. Therefore, the gas velocity is set equal to the relaxed liquid velocity, as Figs. 42 and 43 indicate. This approach to control the gas velocity produces more realistic physical results then the approach used by Ferrari *et al.* (2017), who set the gas velocity to zero in the slug region.

Regarding the numerical approaches, the Roe method's results are similar to the solution obtained by Ferrari *et al.* (2017), which was expected, since the authors used the

Roe method in their simulation. There are, nevertheless, small differences among the three mathematical models, which, in addition to the different treatment for the gas velocity, helps to explain the slight differences in the three sets of Roe' results observed in the plots. However, this does not make the Roe simulation better or worse than the AUSMDV solution since different numerical methodologies are being compared. The AUSMDV is advantageous in terms of the numerical structure of the method and computational time, as already mentioned. When the four sets of results are considered, the differences observed for the gas velocity and, consequently, the other flow variables are related to the different mathematical models, numerical methods, and procedures to calculate the gas phase in the slug body.

The same test case was run using the 7E2P model and the results are presented in Figs. 45 to 48. These graphs confirm that the 7E2P and 5E2P models return similar results for the studied cases. The 7E2P model was originally conceived as an attempt to improve the physics and free the mathematical model from its limitations regarding the artificial control of the volume fractions when one of the phases vanishes. As the model requires, the liquid and gas volume fractions must be within the open interval between zero and one. However, in the slug region for instance, the void fraction tends to zero, creating a singularity in the gas momentum equation. With the improvement in the slug-flow physics due to the addition of bubbles in the liquid phase and droplets in the gas phase, it was at first believed that the 7E2P model would be able to guarantee that the gas phase (or the liquid phase) would never vanish. From the study dedicated to this model, it was verified that this limitation of the two-fluid model was not fully eliminated and, for the slug capturing simulations, it did not reveal significant advantage over the 5E2P model, at least for the cases and the flow conditions considered. Table 13 presents the computational time required for this slug flow simulation considering each model and method combination. The configuration of the computer that was used for this study is Intel® Core ™ i7-8700 CPU 3.70GHz and in order to have a fair comparison in terms of CPU time, the simulations were run with CFL number of 0.45. Based on that analysis, the following results that shows a comparison with experimental data are performed only with the 5E2P model, since it ends up being less computationally demanding for having less equations to be solved. The 7E2P might be more suitable in more complex flow scenarios, such as the ones that droplets and bubbles have a more significant impact in the flow and/or with mass transfer terms added to the equations.

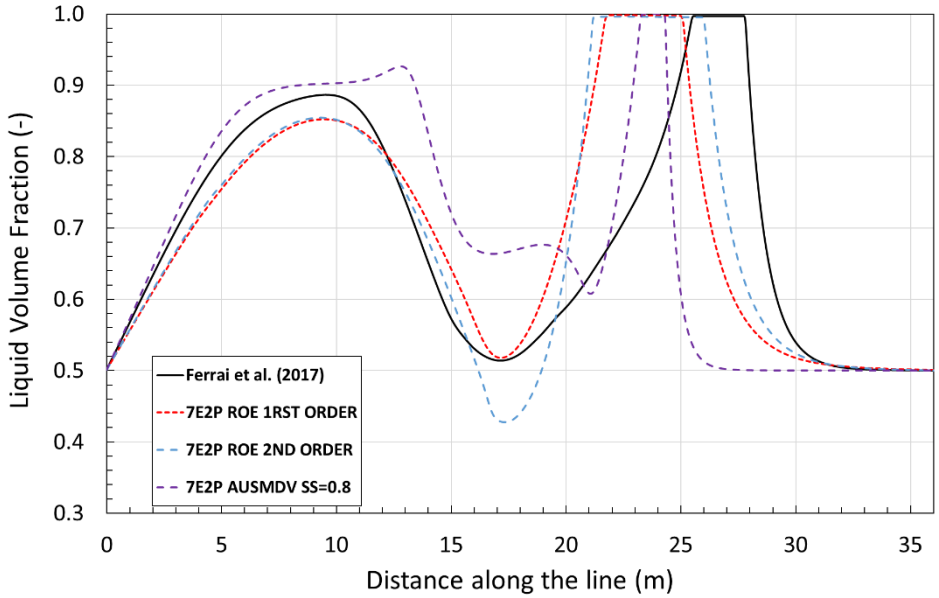

Figure 45: Liquid volume fraction distribution along the line for the 5E2P model for the slug formation and evolution test case at *t*=8s.

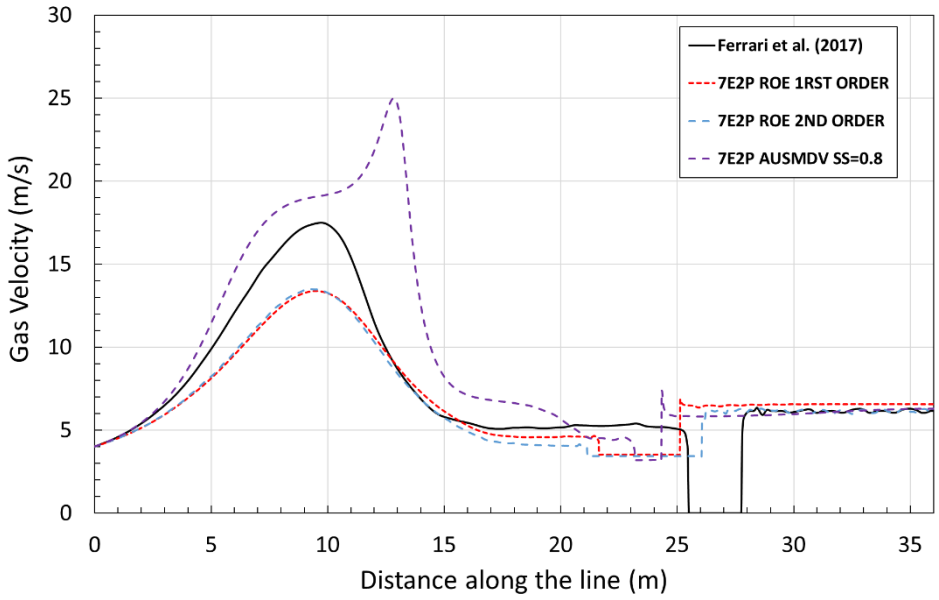

Figure 46: Gas velocity distribution along the line for the 5E2P model for the slug formation and evolution test case at *t*=8s.

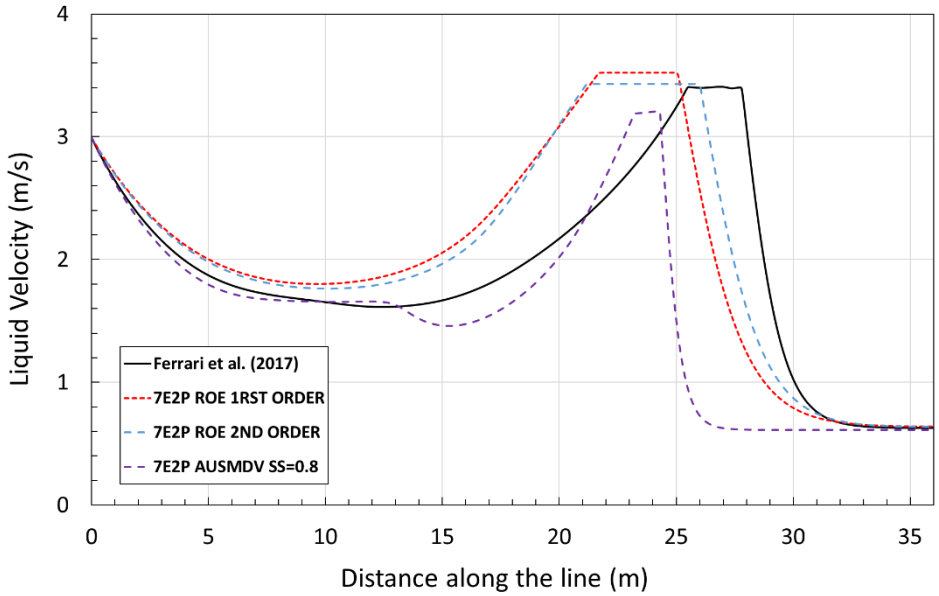

Figure 47: Liquid velocity distribution along the line for the 5E2P model for the slug formation and evolution test case at *t*=8s.

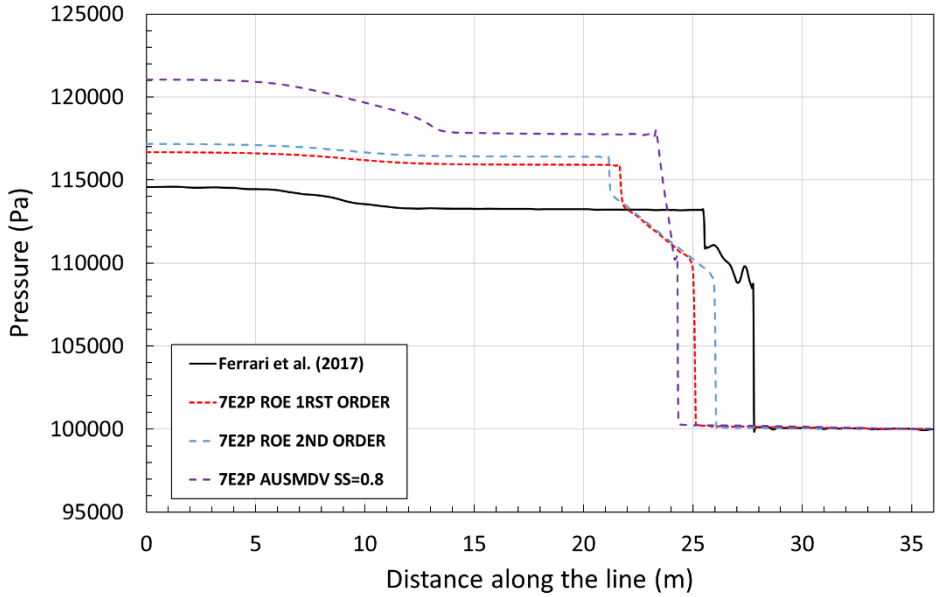

Figure 48: Pressure distribution along the line for the 5E2P model for the slug formation and evolution test case at *t*=8s.

Table 13: CPU time analysis for each model and method combination.

Model and Method	CPU Time
5E2P AUSMDV	2014.41 s
7E2P AUSMDV	3195.75 s
5E2P Roe (1rst order)	2805.36 s
7E2P Roe (1rst order)	5998.82 s
5E2P Roe (2nd order)	4131.57 s
7E2P Roe (2nd order)	8502.21 s

7.2 Comparison with Experimental Data

An experimental campaign was carried out at the University of Tulsa (Tulsa, OK, USA) in order to validate the proposed numerical model in simulating the intermittent flow pattern. The validation of the simulated results is performed comparing slug characteristics of each flow scenario.

To better understand and interpret the results that follow, some pieces of information regarding the numerical simulations are important to be highlighted in the list below.

- Only the 5E2P model in association with the AUSMDV ss=0.8 is used.
- Aiming at improving even further the physics embedded in the model, the velocity relaxation procedure was replaced, in the simulations that follows, by the Harmarthy (1960) correlation, given by Eq. (3.76). This equation is used to model the gas velocity in the slug body for all the simulations in the study described next. The motivation for employing this model lies in the experimentally observed fact that there is an actual slip between the gas bubbles and the liquid phase in the slug region.
- Taitel and Dukler (1976) friction correlation, Eq. (3.47), is used to model the gas friction with the wall and the interfacial friction. For the liquid friction with the wall, the correlation of Spedding and Hand (1997), Eq. (3.49), is implemented.
- The liquid volume fraction is a boundary condition that is prescribed at the pipe inlet in the numerical simulations. There is a certain difficulty in measuring liquid volume fraction experimentally at the inlet because of the mixing region of the fluids at this position. It is known that the superficial velocities are the important parameters of the flow, which means that the liquid volume fraction itself should

not affect the flow characteristics. Thus, a guess of the void fraction is determined from a relationship that expresses an equilibrium condition of the stratified flow (Taitel and Dukler, 1976), which is given by

$$\frac{\tau_{Gw}S_G}{\alpha_G} - \frac{\tau_{Lw}S_L}{1-\alpha_G} + \tau_I S_I \left(\frac{1}{1-\alpha_G} + \frac{1}{\alpha_G}\right) + (\rho_L - \rho_G)Ag\sin\theta = 0, \qquad (7.1)$$

where S_G, S_I and S_L are the gas, interface, and liquid wetted perimeters, respectively, that are calculated considering a stratified geometry. The quantities τ_{Gw}, τ_I and τ_{Lw} are the wall-gas, interface and wall-liquid shear stresses. Some tests were made, during the development of the work, with different values for the void fraction at the inlet. The results suggest that slug characteristics are not significantly affected if the void fraction at the inlet is changed, as long as the superficial velocities remain the same. However, a more detailed study regarding this effect on the flow needs to be carried out.

- Pressure correction and interfacial velocity terms are calculated according to Eqs. (3.42) and (3.43), respectively. Some tests were performed with the AUSMDV method using different interfacial velocity models, such as the one described in Furfaro and Saurel (2015), in which this parameter is calculated according to the acoustic impedance, and also considering values within gas and liquid velocities range. The results indicate that slug characteristics were not significantly affected with the changes in this parameter.
- During the numerical simulations, results were recorded for all flow variables at different positions of the pipeline along the time with a sample frequency of 1000 Hz.

7.2.1 Results for the Water-Air Facility

The experimental data was acquired fixing the liquid mass flow rate and varying the gas mass flow rate for several inclination angles: 2°, 5°, 15°, 20° and 30°. The first group of experiments were conducted for air-water system under steady-state condition. Even though the slug flow does not have a strict periodic behavior, its intermittency achieves a statistical steady state that allows the calculation of some slug characteristics, such as slug

frequency and translational velocity, that can be inferred from the experimental data and compared to the numerical simulation. Table 14 shows the flow configuration that were used in the numerical simulations. The flow temperature and pressure were set in the simulation based on the arithmetic average acquired from experimental data for each superficial gas velocity and inclination angle.

Table 14: Flow configuration for the comparison with the water-air experimental facility.

Configuration	Value
Fluids	Water and Air
Pipeline Length	20.42 m
Internal Diameter	0.1016 m
Pipeline Roughness	3.4×10^{-5} m
Liquid Reference Density	998 kg/m³
Speed of Sound in Liquid	1480 m/s
Gas Constant	287 (J/kg.K)
Liquid Viscosity	1.001×10^{-3} Pa.s
Gas Viscosity	1.9×10^{-5} Pa.s
CFL number	0.45
Mesh size	2000

Slug Frequency

Slug frequencies are determined based on the number of slugs that passes in a time window. Each of the following graph represents the slug frequency for a specific inclination angle plotted against the superficial gas velocity.

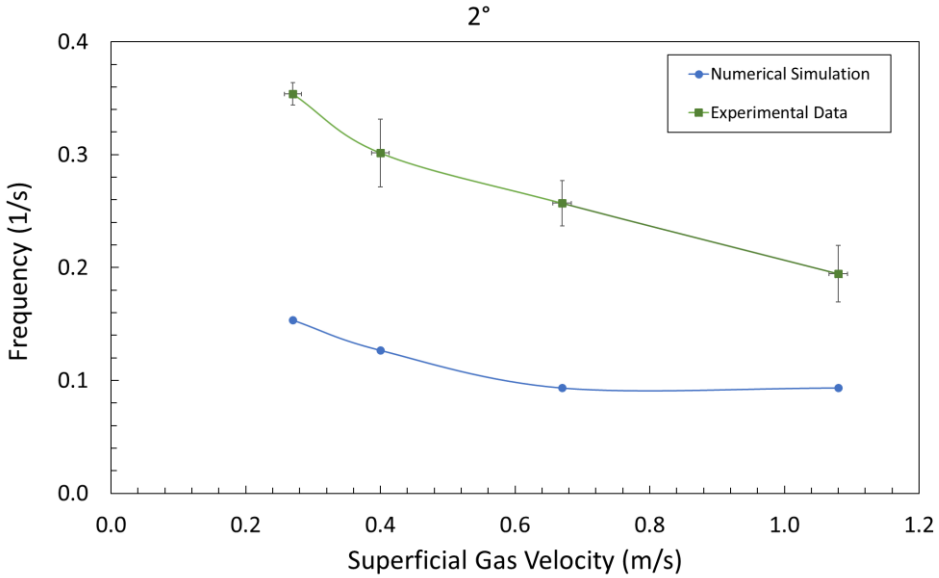

Figure 49: Slug frequency comparison between experiments and numerical simulation for the water-air facility with inclination angle of 2°.

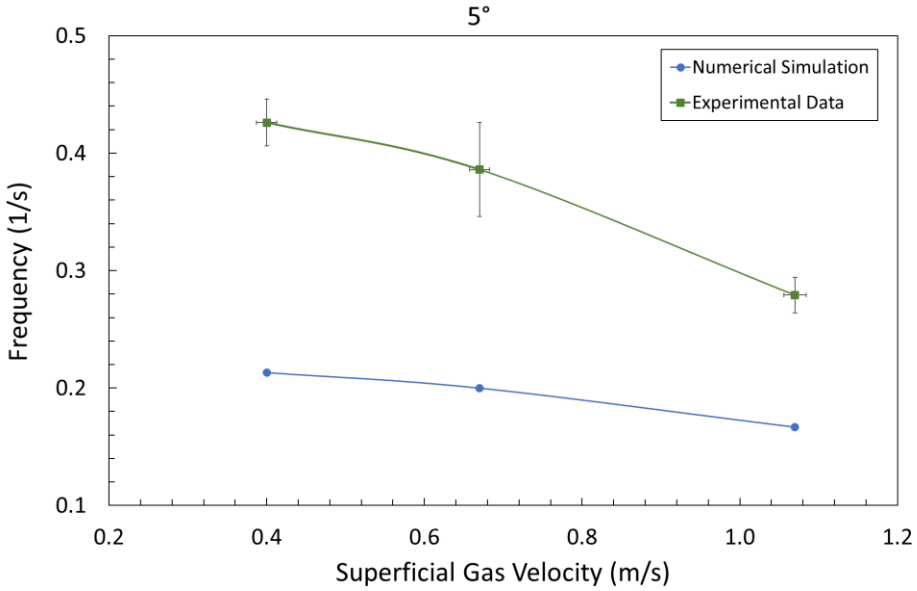

Figure 50: Slug frequency comparison between experiments and numerical simulation for the water-air facility with inclination angle of 5°.

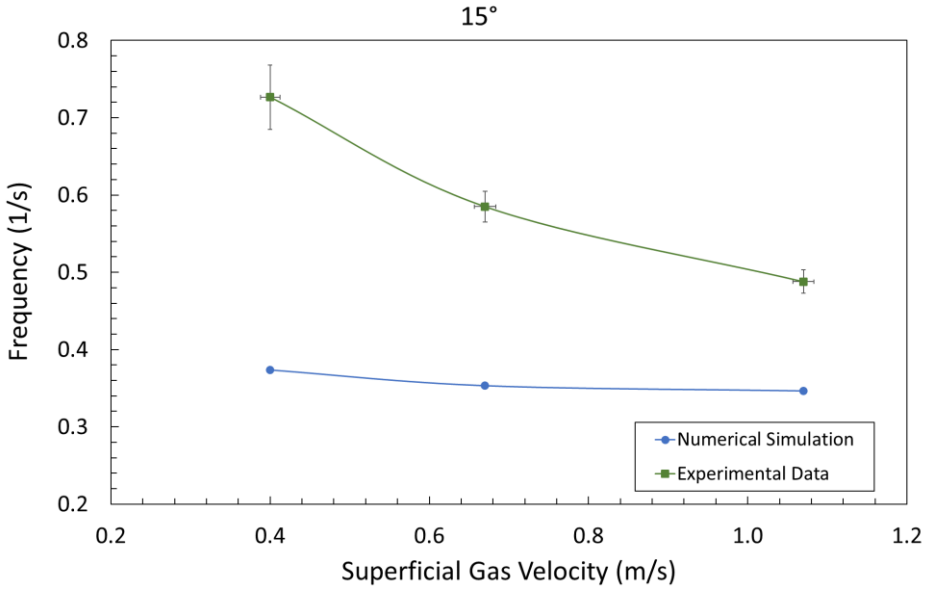

Figure 51: Slug frequency comparison between experiments and numerical simulation for the water-air facility with inclination angle of 15°.

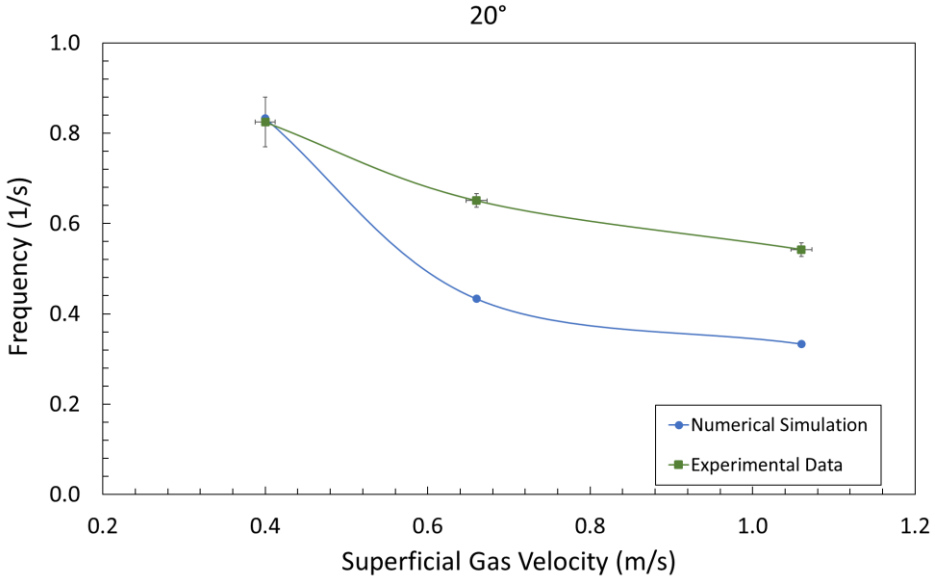

Figure 52: Slug frequency comparison between experiments and numerical simulation for the water-air facility with inclination angle of 20°.

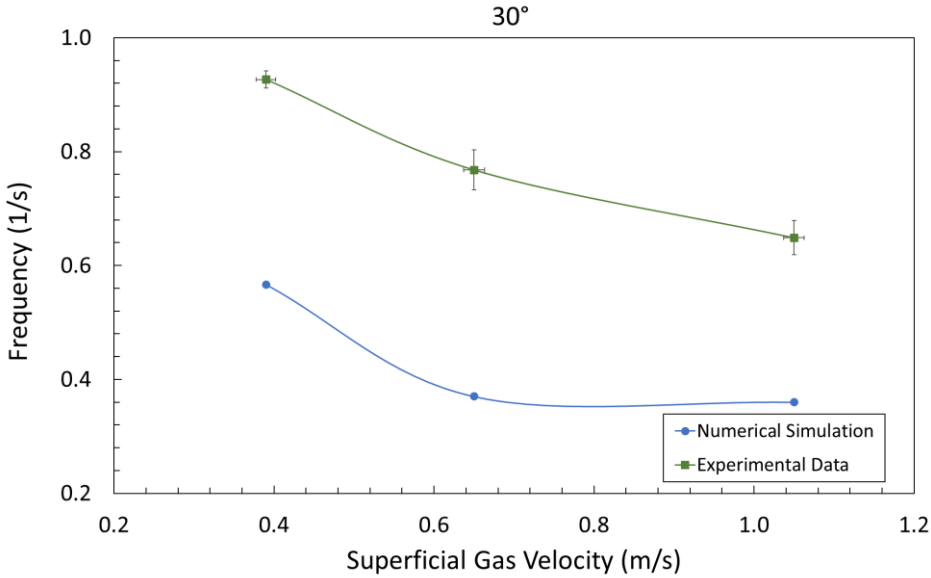

Figure 53: Slug frequency comparison between experiments and numerical simulation for the water-air facility with inclination angle of 30°.

It can be noticed from Figs. 49 to 53 that under similar operation conditions, the slug frequency decreased as the superficial gas velocity increased for both experiments and numerical simulations. Even though the results for the simulations are underpredicting the slug frequencies, the tendency observed in the experiments was also obtained with the simulations. The fact that numerical frequency is lower than the experimental frequency may be explained by several factors. First, the absence of gas entrainment in the model has some impact on the slug dynamics, which will implicate that the bubbles of gas remain in the gas pocket above the liquid film (the Taylor bubble), increasing the distance between two slug bodies. Consequently, it will generate sparser slugs and lower slug frequencies. Although the 7E2P model considers the presence of bubbles and droplets explicitly in its formulation, it does not allow for gas entrainment either and, therefore, it results in lower frequencies, as well. Also, experimental observation of slug flow suggests that there is significant agitation (turbulence) in the slug front region, which is responsible for an extra pressure gradient, called “vortex pressure drop” in the literature (Cook and Behnia; 2000). Since the models here studied are one-dimensional, it is not possible to take this effect directly into consideration. This phenomenon may have an impact on how rapid the slug is formed. Furthermore, a new model that encompasses separate momentum equations for all the phases (including bubbles and droplets), which comprises a system of nine nonlinear PDE’s, may help to generate numerical results for the slug frequency that are closer to the experiments.

To allow a direct comparison between the experimental and the numerical data, Fig. 54 presents the entire set of data concerning the slug frequencies for all inclination angles and superficial gas velocities, bounded by 60% error lines. A curve fit through this data implies that, on average, the numerical slug frequencies are about 40% lower than the experimental frequencies.

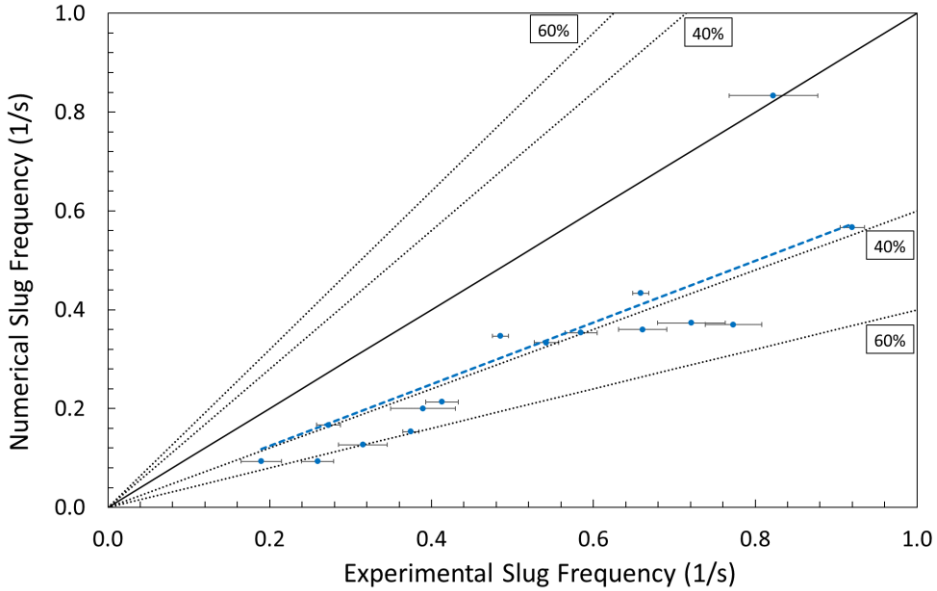

Figure 54: Numerical slug frequency compared against experimental slug frequency for the water-air facility.

Translational Velocity

According to Shoham (2006), there are two velocities associated to the slug flow that are important to describe the slug physics, the u_s and the u_t, which are the mean true velocity of the fluid in the slug body and the translational velocity, respectively. The translational velocity is the velocity of the slug front or the velocity of the interface between the gas (Taylor bubble) and the slug body. The slug velocity is the mixture velocity, $u_m = u_{sG} + u_{sL}$ and the translational velocity may be expressed in terms of the mixture velocity as

$$u_t = c_0 u_m + u_d \,, \tag{7.2}$$

where c_0 is a flow distribution coefficient and u_D is the drift velocity, which is the velocity of a Taylor bubble in a stagnant liquid. The distribution parameter is reported by Fabre (1994) and Shoham (2006) to be 1.2 for turbulent flow and 2 for laminar flow, based on the slug Reynolds number $Re_{LS} = \rho_L u_m D/\mu_L$. The drift velocity can be calculated, for instance, according to Bendiksen's correlation (Bendiksen, 1984) that is applicable to all inclinations,

$$u_d = 0.54\sqrt{gD}\cos\theta + 0.35\sqrt{gD}\sin\theta \quad \text{for } 0° \leq \theta \leq 90°, \tag{7.3}$$

where θ is the pipe inclination angle, g is the gravity and D is the pipeline diameter.

The translational velocity of the experiments is calculated using the cross-correlation, that was also used in many previous works, such as Gokcal (2008), Brito (2012) and Zhu (2019). The cross-correlation is a measure of how the two signals detected by the conductivity (or capacitance) sensors are correlated with each other based on the time delay between them. According to Brito (2012), if the signals are the same, the cross correlation returns one, whereas if they are completely different, it will be zero. With the output signals from the pair of conductivity (or capacitance) sensors, the cross-correlation analysis can be performed knowing the distance that separate the sensors from each other, and the translational velocity is obtained as follows

$$u_t = \frac{\Delta L}{\tau}. \tag{7.4}$$

In Eq. (7.4), ΔL is the distance between the pair of sensors and τ is the temporal lag in seconds. It is worth mentioning that the same procedure for calculation of the translational velocity was done with the numerical results, in order to have the same strategy of comparison.

The following graphs, shown in Figs. 55 to 59, show the translational velocity plotted against the mixture velocity for the numerical simulation, the experiments and the Bendiksen's correlation, for each inclination. The uncertainty associated with the Bendiksen's correlation, $U_{u_{tP}}$, is also displayed in the graphs and are calculated according to Aql (2020) as follows

$$U_{u_{tP}} = -0.115 \ln(u_m) + 0.14. \quad (7.5)$$

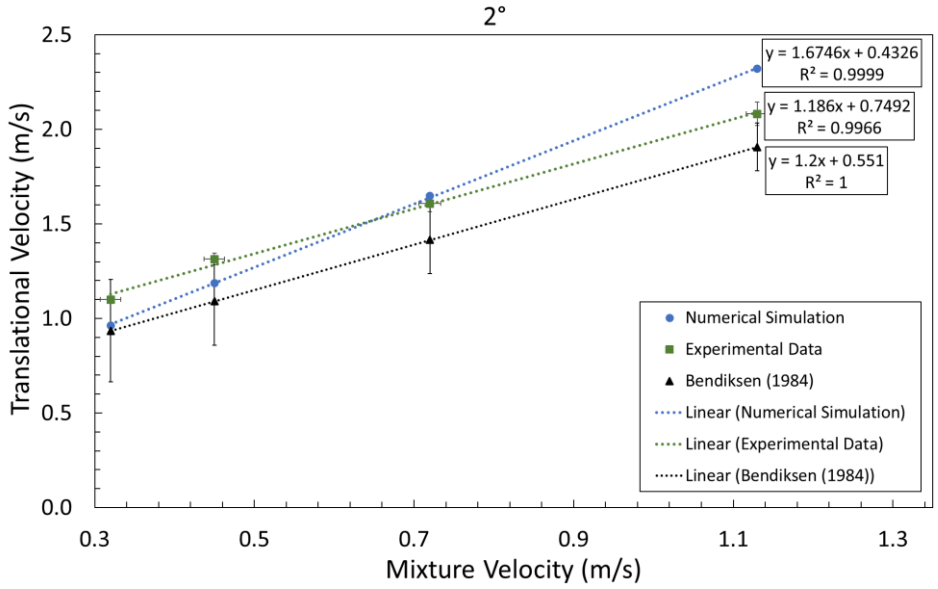

Figure 55: Translational velocity against the mixture velocity for the water-air facility with inclination of 2°.

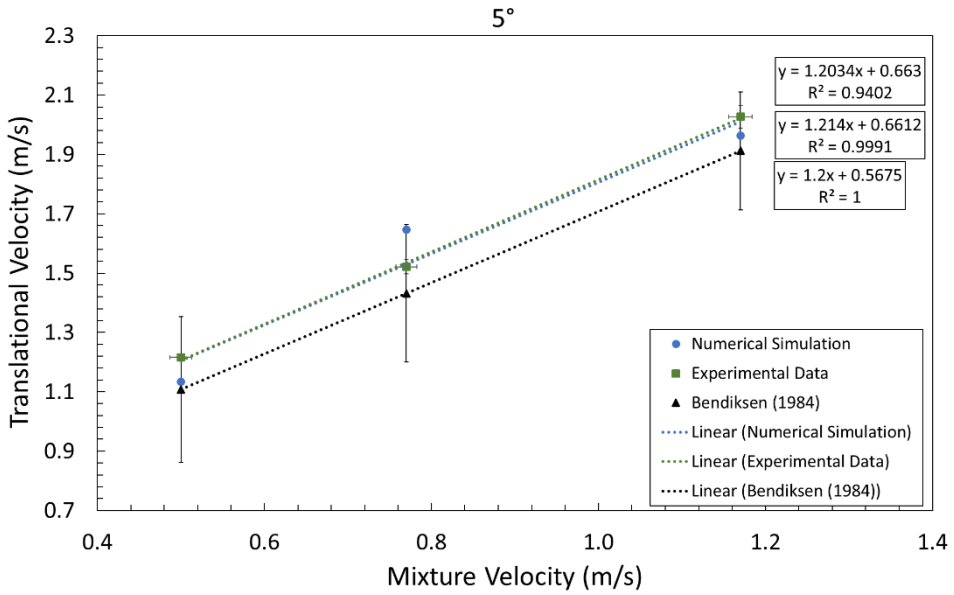

Figure 56: Translational velocity against the mixture velocity for the water-air facility with inclination of 5°.

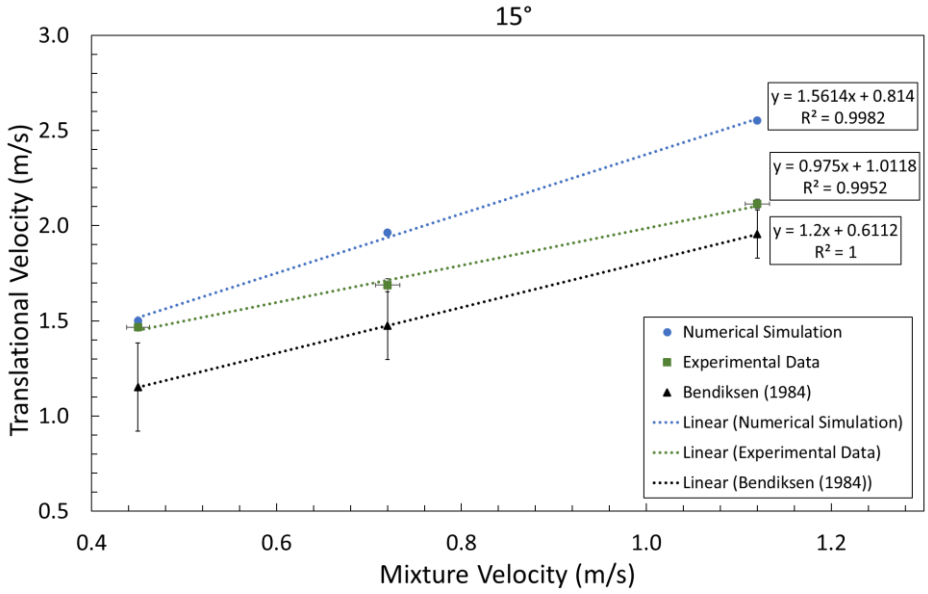

Figure 57: Translational velocity against the mixture velocity for the water-air facility with inclination of 15°.

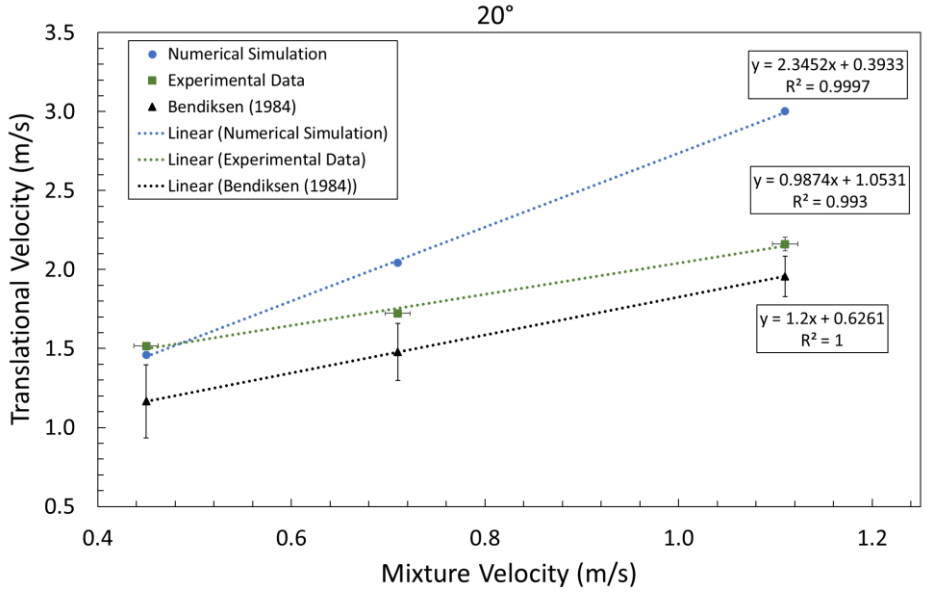

Figure 58: Translational velocity against the mixture velocity for the water-air facility with inclination of 20°.

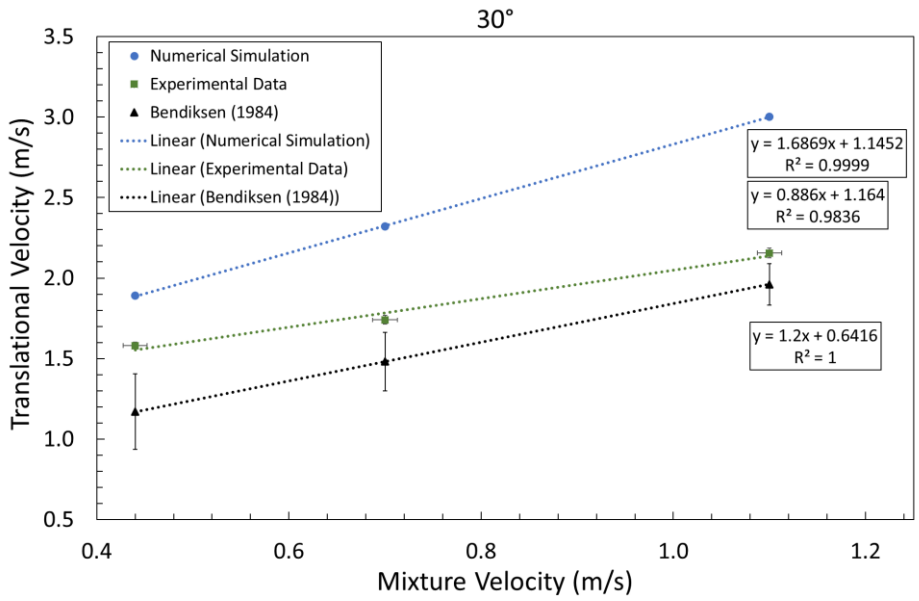

Figure 59: Translational velocity against the mixture velocity for the water-air facility with inclination of 30°.

The translational velocities obtained with the numerical simulations and experiments have a linear relation with the mixture velocity, as expected from the theory. The angular coefficient expected is 1.2 because we are dealing with turbulent flow for all inclination conditions. As can be observed, the translational velocity is, overall, being overpredicted by the numerical simulations. The slug flow is affected by a mixing region in front of the slug body that forms a recirculation zone that causes loss of momentum in different directions. Again, this effect is responsible for what the literature calls the "vortex pressure drop" (Cook and Behnia, 2000). The mathematical model herein used is a one-dimensional approach of the problem, and, consequently, there are some physical behaviors, such as the recirculation, that it is not capable of predicting. The differences observed in the graphs can be explained by the simplicity of the one-dimensional model in representing effects that are intrinsically three-dimensional. Fig. 60 represents the summary of the translational velocity of the simulations compared to the experiments with 30% error. A curve fit through this data implies that, on average, the numerical translational velocities are about 20% higher than the experimental ones.

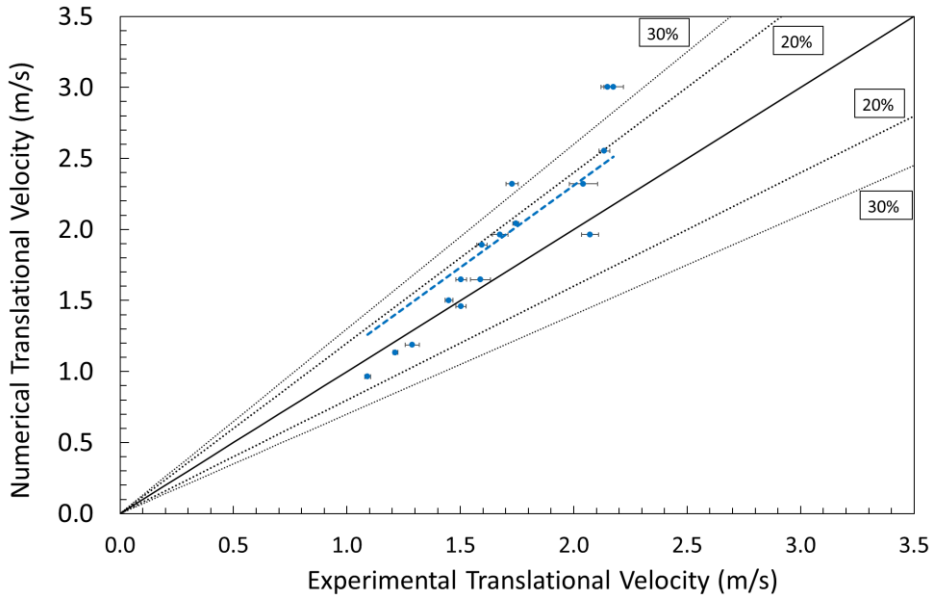

Figure 60: Numerical translational velocity compared against experimental translational velocity for the water-air facility.

Pressure Gradient

The pressure gradient is also compared to the experimental data. Single phase tests were conducted to check the proper functionality of the differential pressure sensors, as detailed in Appendix B. The pressure gradient results for the experiments are obtained according to Eq. (5.3), in which an arithmetic average of the three DP sensors is calculated. For the numerical simulation, pressure results at the same locations as in the experimental facility were acquired through time. The DP sensors are located at the second half of the pipeline, being the last two DPs very close to the outlet. During the simulations, it was possible to observe that there is a boundary effect near the outlet due to the boundary condition imposition at this location. Therefore, for the pressure gradient, only the first DP location was considered to obtain the numerical results for this facility. The pressure gradient obtained with the experimental runs are compared to the numerical results, as can be seen in Fig. 61.

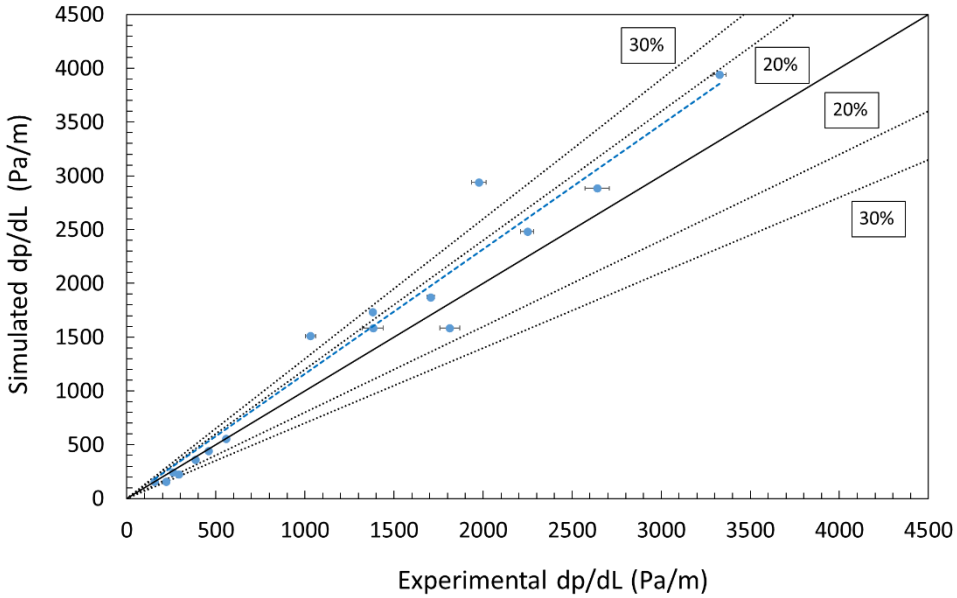

Figure 61: Numerical pressure gradient compared against experimental pressure gradient for the water-air facility.

From the previous graph, the pressure gradient results are comparable to the experimental ones with the same order of magnitude and the error range is 30%. The pressure is a flow variable that is very sensitive to the passage of the slugs during the simulation. This sensibility returns oscillations that increases numerical dispersion, impacting the accuracy of the measurement. Even though this behavior is observed, the obtained results are promising, presenting a good estimation of the expected pressure gradient. A curve fit through this data implies that, on average, the numerical pressure gradients are about 20% higher than the experimental pressure gradients.

7.2.2 Results for the High Viscosity Oil-Air Facility

The experimental data obtained at the high viscosity oil-air facility was acquired for one inclination angle only, the horizontal configuration, under steady-state condition. Different combinations of liquid and gas superficial velocities were analyzed. The high viscosity-air is an indoor facility in which the room temperature is controlled to keep the fluid's temperature at the desired state. The temperature affects the oil viscosity and density and, therefore, the dynamics of the slug flow.

Table 15 shows the flow configuration that were used in the numerical simulations. The flow temperature and pressure were set in the simulation based on the mean value acquired from experimental data for each flow condition. The fluids, oil and air, and the

flow conditions were chosen such that the slug flow was laminar to distinguish form the air-water flow studied at the other facility.

Table 15: Flow configuration for the comparison with the high viscosity oil-air experimental facility.

Configuration	Value
Fluids	Oil and Air
Pipeline Length	18.48 m
Internal Diameter	0.0508 m
Pipeline Roughness	3.4 x 10^{-5} m
Liquid Reference Density	849.92 kg/m³
Speed of Sound in Liquid	1450 m/s
Gas Constant	287 (J/kg.K)
Oil Temperature	70°F or 21.1°C
Liquid Viscosity	0.68 Pa.s
Gas Viscosity	1.9 x 10^{-5} Pa.s
CFL number	0.45
Mesh size	2000

Slug Frequency

The same slug frequency analysis is performed for the oil-air cases. Figures 62 to 66 show the numerical simulation results for slug frequency compared to experimental data for each superficial liquid velocity.

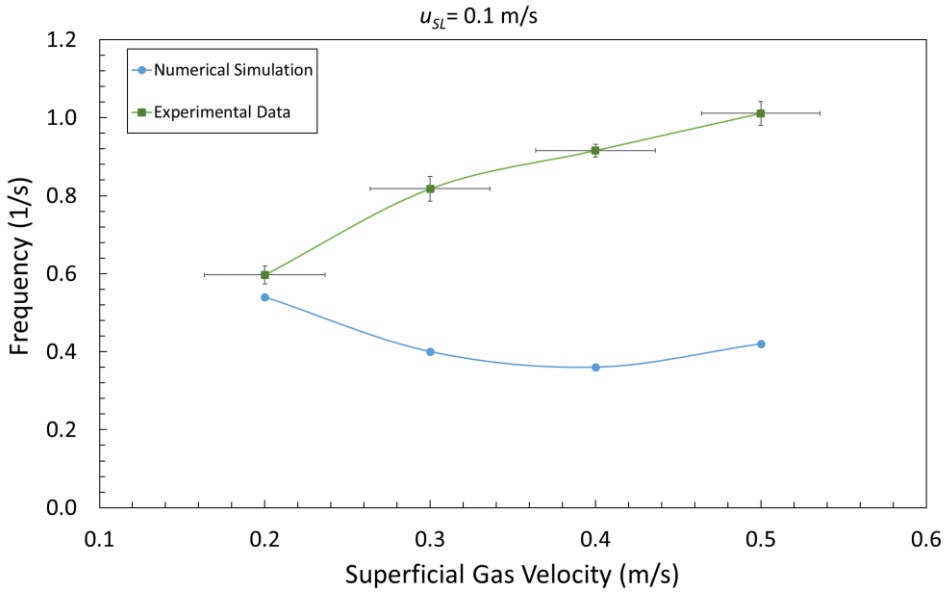

Figure 62: Slug frequency comparison between experiments and numerical simulation for the high viscosity oil-air facility with $u_{SL} = 0.1$m/s.

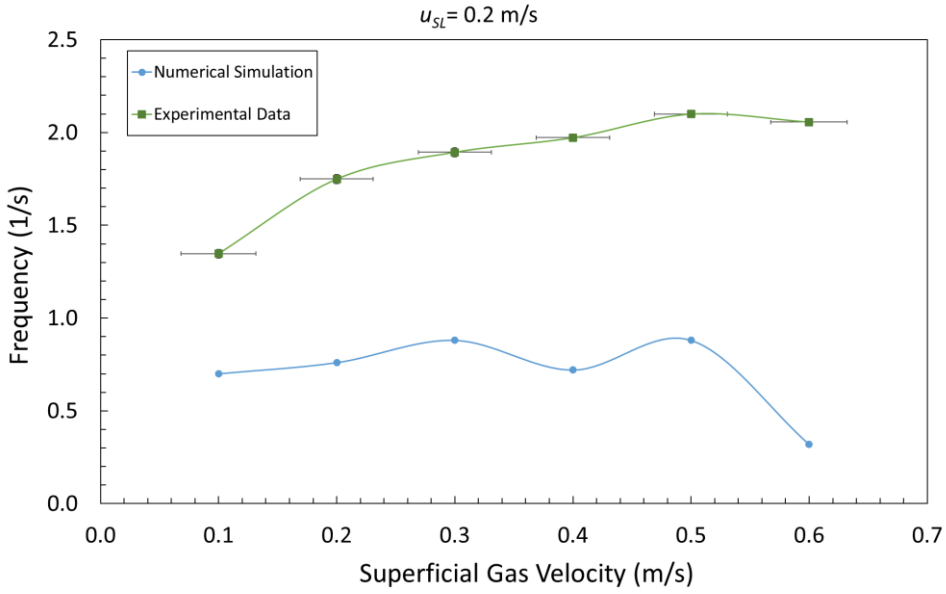

Figure 63: Slug frequency comparison between experiments and numerical simulation for the high viscosity oil-air facility with $u_{SL} = 0.2$m/s.

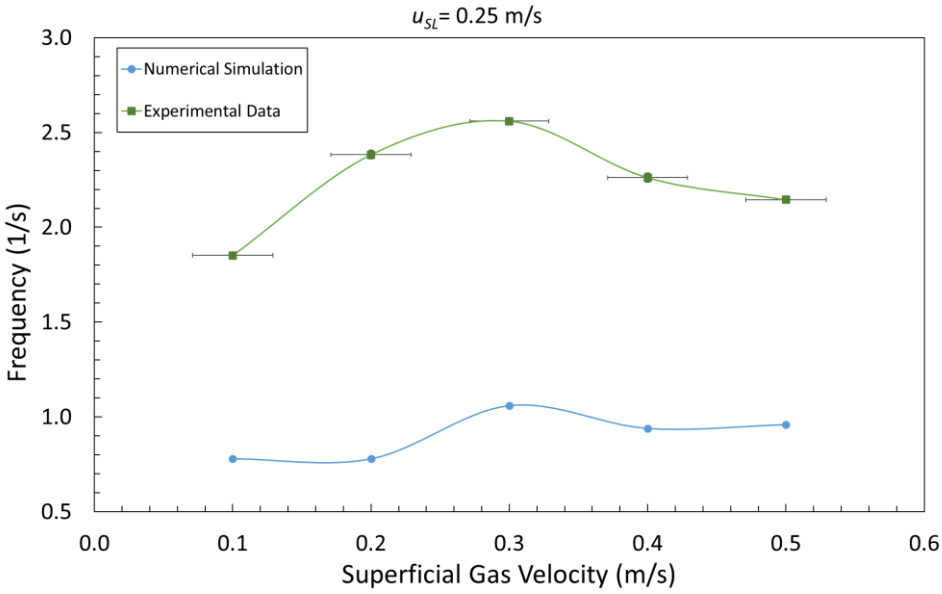

Figure 64: Slug frequency comparison between experiments and numerical simulation for the high viscosity oil-air facility with $u_{SL} = 0.25$m/s.

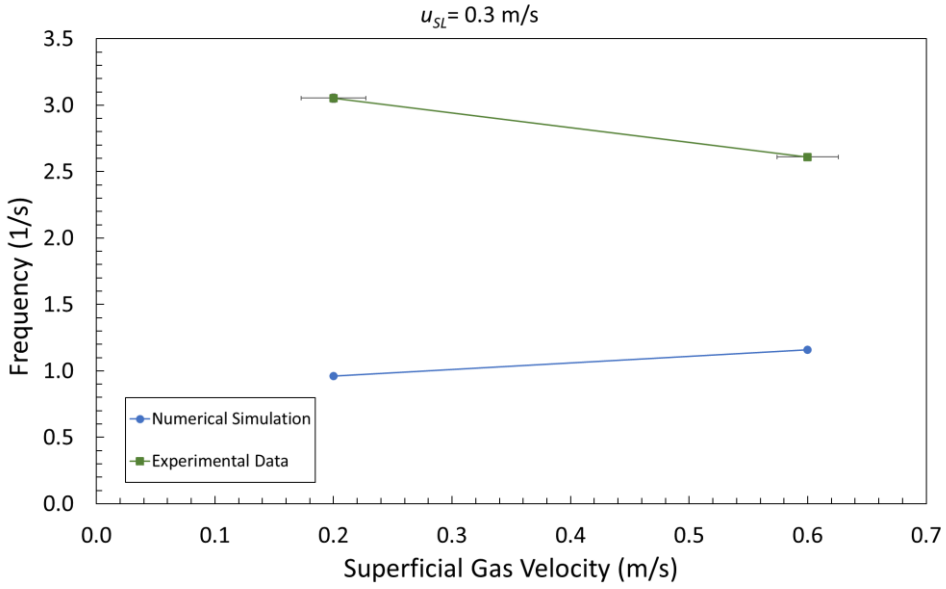

Figure 65: Slug frequency comparison between experiments and numerical simulation for the high viscosity oil-air facility with $u_{SL} = 0.3$m/s.

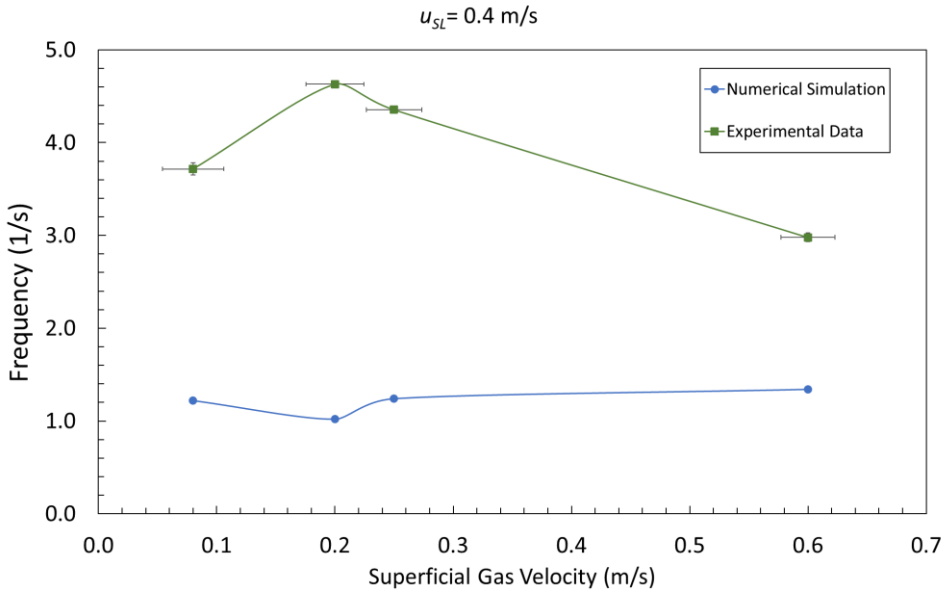

Figure 66: Slug frequency comparison between experiments and numerical simulation for the high viscosity oil-air facility with $u_{SL} = 0.4$m/s.

It can be observed that, once again, the slug frequencies are underpredicted by the numerical model. It is possible to notice that the slug frequencies, in general, increases with the increased viscosity, which was expected according to Gokcal (2008). The lower values of frequency can be explained by the lack of a gas entrainment model, as mentioned previously, leading to longer gas pockets and, therefore, a smaller number of slugs. Moreover, experimental observation of slug flow suggests that there is significant agitation (turbulence) in the slug front region, called "vortex pressure drop" in the literature (Cook and Behnia; 2000) that the one-dimensional models here studied are not taking into consideration.

The following graph presents the summary of the comparison of the slug frequency obtained numerically and experimentally with 70% error. As expected, based on the previous graphs, the slug frequencies were not as well captured by the numerical strategy as for the previous experiments. With the increased oil viscosity, the slug frequencies increased, however, it was not enough to have a better match with the experiments. A curve fit through this data implies that, on average, the numerical slug frequencies are about 70% lower than the experimental ones.

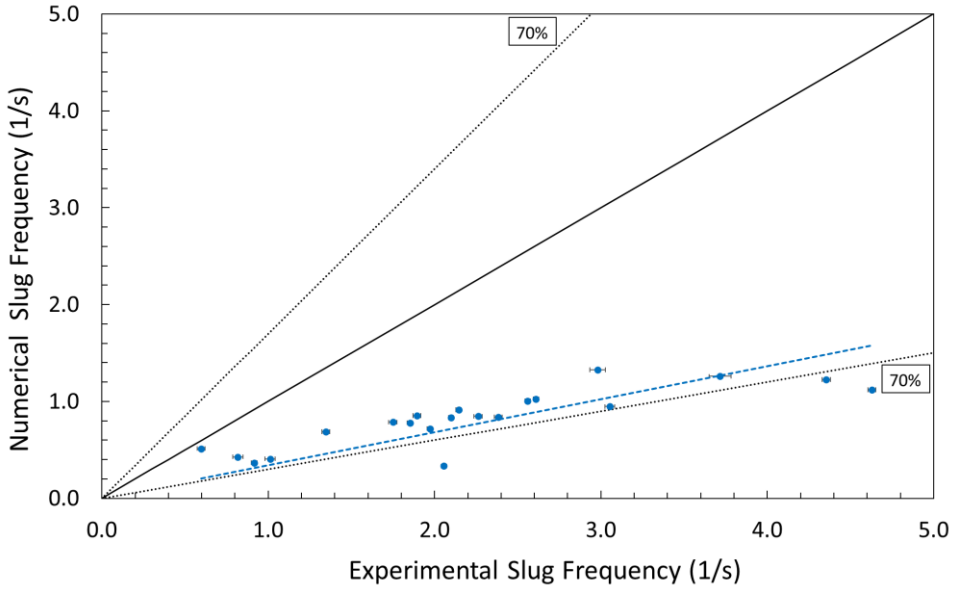

Figure 67: Numerical slug frequency compared against experimental slug frequency for the high viscosity oil-air facility.

Translational Velocity

In Eq. (7.3), the drift velocity was calculated according to Bendiksen's (1984) correlation. Despite being a great reference in obtaining the translational velocity, this correlation does not consider the liquid viscosity. Thus, another correlation is compared to the results taking into account the liquid viscosity. The correlation of Moreiras *et al.* (2014) is also plotted in the translational velocity graph with Bendiksen's (1984) correlation. This correlation is calculated as follows

$$u_d = \mathrm{Fr}\rho_L{}^{-0.5}[gD(\rho_L - \rho_G)]^{0.5}, \tag{7.6}$$

where

$$\mathrm{Fr} = \mathrm{Fr}_H \cos\theta^{1.2391} + \mathrm{Fr}_V \sin\theta^{1.2315} + Q, \tag{7.7}$$

$$\mathrm{Fr}_H = 0.54 - \frac{N_{vis}}{1.886N_{vis} + 0.01443}, \tag{7.8}$$

$$\mathrm{Fr}_V = -\frac{8}{3}N_{vis} + \sqrt{\frac{2}{9}\frac{\rho_L}{(\rho_L - \rho_G)} + \frac{64}{9}N_{vis}^2} - \left(\frac{\sqrt{2}}{3} - 0.35\right)\sqrt{\frac{\rho_L}{(\rho_L - \rho_G)}}, \quad (7.9)$$

where

$$N_{vis} = \frac{\mu}{\sqrt{gD^3(\rho_L - \rho_G)\rho_L}}. \quad (7.10)$$

If $(\mathrm{Fr}_V - \mathrm{Fr}_H) < 0$, then $Q = 0$. If $(\mathrm{Fr}_V - \mathrm{Fr}_H) \geq 0$,

$$\mathrm{Q} = 2.1589(\mathrm{Fr}_V - \mathrm{Fr}_H)^{0.70412}\sin\theta(1 - \sin\theta). \quad (7.11)$$

In Fig. 68 the translational velocity is plotted against the mixture velocity for the numerical simulations, experimental results and the two correlations, Bendiksen (1984) and Moreiras *et al.* (2014).

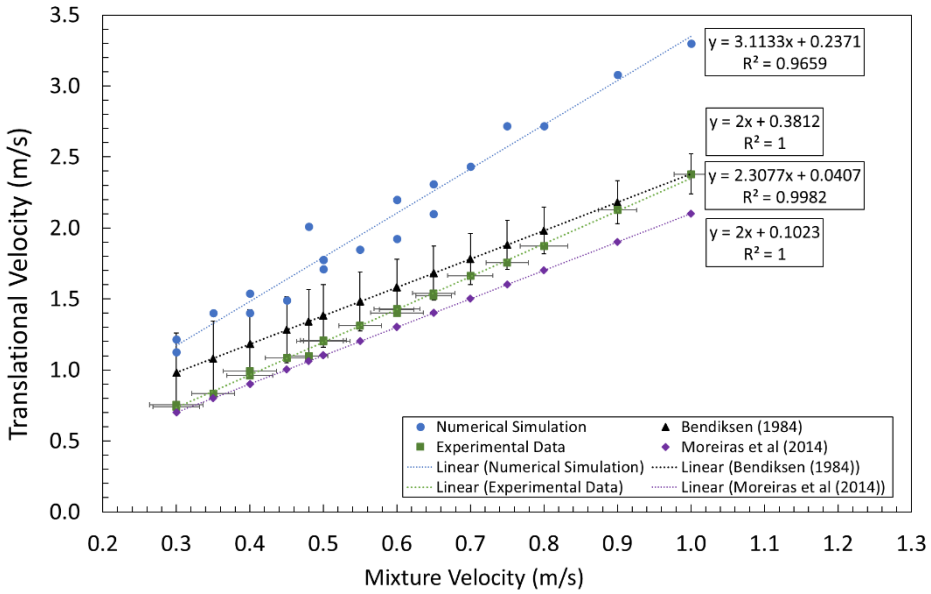

Figure 68: Translational velocity against the mixture velocity for the high viscosity oil-air facility.

It can be observed that the translational velocity and mixture velocity have a linear relation for all the results, the angular coefficient for the curves is greater than for the previous experimental facility results and near the value of 2, corresponding to laminar

flow, which was expected. The translational velocity obtained from the numerical results, once again, has differences if compared to the experimental results. These differences can be explained based on the absence of gas entrainment in the model that has some impact on the slug dynamics and the simplicity of the one-dimensional model in representing effects that are intrinsically three-dimensional, such as the significant agitation (turbulence) in the slug front region, which is responsible for an extra pressure gradient, called “vortex pressure drop”.

A summary of the simulated and experimental translational velocity and a curve fit through this data implies that, on average, are higher than the experimental translational velocities with 50% error, as presented in Fig. 69.

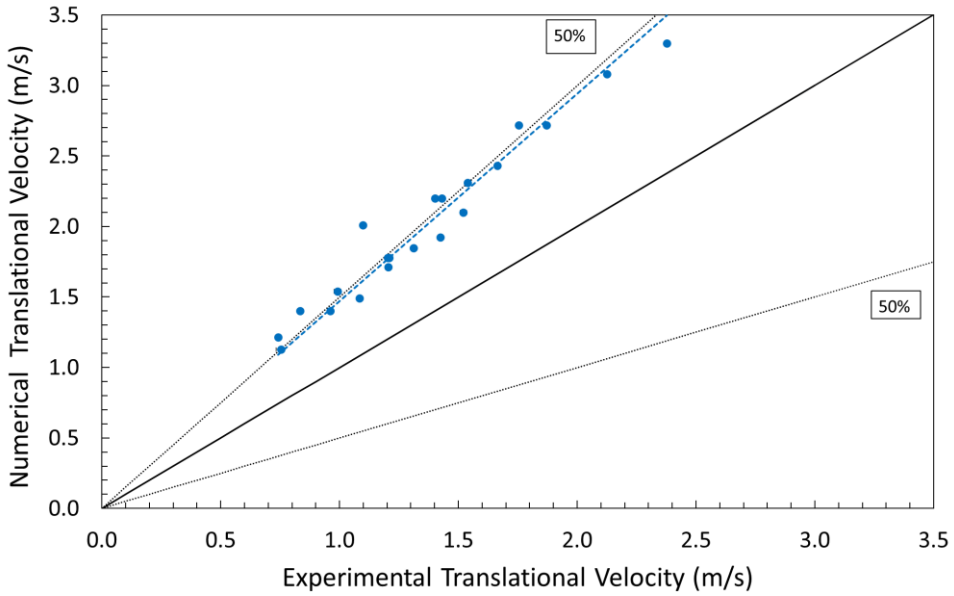

Figure 69: Numerical translational velocity compared against experimental translational velocity for the high viscosity oil-air facility.

Pressure Gradient

The pressure gradient is also compared to the experimental data. Single phase tests were performed to verify the proper functionality of the differential pressure sensors, as detailed in Appendix B. As can be observed in the Appendix B, for this experimental facility, the first two differential pressure sensors returned higher errors if compared to the others. For that reason, in the pressure gradient calculation for the experimental data, the first two DP sensors are neglected, and the arithmetic average was taken from the

others two sensors. For the numerical simulation, the same boundary effect can be observed, as described for the 4in facility. Therefore, an arithmetic average of DP1 and DP2 are taken to obtain the final pressure gradient result.

The pressure gradient that is generated by the numerical simulations are plotted against the experimental results with a range of 50% error, as presented in Fig. 70. It can be inferred from the graph that the pressure drop is overpredicted, in an overall perspective, by the numerical simulations. As already mentioned in the previous section, oscillations in the pressure results are observed, increasing numerical dispersion. For this facility as the flow conditions are smoother and the flow regime is laminar, the oscillations are smaller, and a more regular trend can be identified in the pressure gradient result.

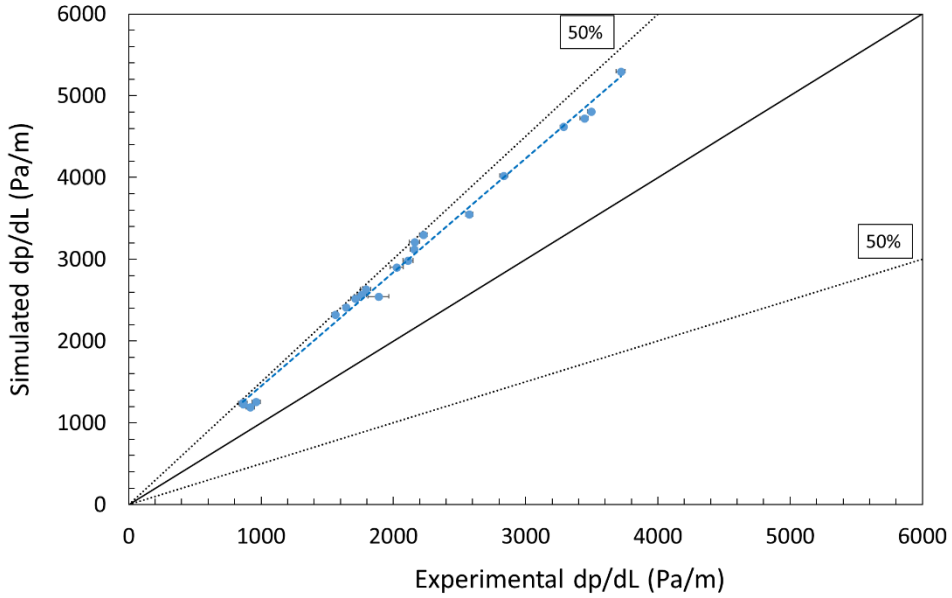

Figure 70: Numerical pressure gradient compared against experimental pressure gradient for high viscosity oil-air facility.

8 Final Considerations

This chapter summarizes all the studies developed in this work and shows the conclusions that are obtained from the analysis of the results. Moreover, recommendations for future work are suggested to improve the slug capturing numerical model.

8.1 Conclusions

During the development of this work, the transient one-dimensional two-fluid model is implemented considering two different approaches: the five-equation model, 5E2P, and the seven-equation model, 7E2P. The 5E2P is used in the literature for slug capturing simulation, while the 7E2P is a new mathematical model that encompasses the droplet and bubble phases. Both mathematical models have two pressures and the addition of the evolution equations for the volume fraction, Eqs. (3.1) and (3.9), turns the models hyperbolic, and the problem becomes well-posed. In comparison with models comprised of less equations, such as the 4E1P model, the two-pressure models present an analytical eigenstructure that facilitate the use of numerical methods that requires the determination of the characteristics, such as the Roe scheme presented. An important comment regarding the 7E2P is that, due to the way it is written, the bubble and droplet volume fractions must be small in order to guarantee that the mixtures wave speeds, gas-droplets and liquid-bubble, are as close as possible to the gas or liquid wave speeds, respectively. The wave speed affects the eigenvalues of the PDE system, which dictates how fast information travels in each phase, and the CFL condition.

Different numerical methods are also considered in the present work: AUSM-type and Roe. Even though all the numerical methods are accurate, they behave differently when compared with each other in the benchmark problem's simulations. The AUSM-type methods, despite being first-order accurate, according to the accuracy check study, are simpler to implement, there is no need for eigenstructure analysis, and the computational time is reduced if compared to the Roe method.

Mathematical models and numerical methods are combined with each other to solve benchmark problems: the water faucet, the shock tube and the separation problems. With this study, it is concluded that the 7E2P returns similar results than the 5E2P and the

AUSM-type of method represented better the expected solutions. The AUSMDV method is subject to a study regarding the tuning parameter that balances, essentially, diffusive and dispersive effects. For the cases that the method was tested in this work, the tuning parameter equals to 0.8 returns better results. According to the studies performed in this work and having in mind the desired application for the numerical strategy, the best model/method combination is the 5E2P with the AUSMDV ss=0.8. However, the 7E2P model, because it incorporates more physics in it, deserves a more thorough investigation on the conditions under which it produces significantly better results than the 5E2P model when compared to experiments. Simulations with higher values of α_B and α_D are imperative, and they must include a gas entrainment model as well as suitable friction correlations for the interaction among the four phases.

Regarding the slug capturing simulation, a comparison with a literature case, in which the slug flow is generated from the stratified flow due to the instabilities that grow in the interface between the fluids, is performed. For this study, the Roe and the AUSMDV methods are used to successfully verify the ability of the numerical model to capture the onset and evolution of the slug flow. Both two-fluid models demonstrated that they can capture the slug flow initiation and development along the line, as was reported in the literature.

Continuing the slug capturing study, an experimental campaign is carried out and the results are compared with the simulations by means of slug characteristics and pressure gradient. During the experimental campaign, two facilities are used: the 2inch and the 4inch facilities. The tests performed with the 4in facility are with water and air for different inclination angles, while for the 2in, the fluids are high viscosity synthetic oil and air and the flow loop is in the horizontal condition. The objective of the experimental campaign is to have enough experimental data that will serve as a validation of the numerical code under several slug flow conditions.

The results indicated that, in general, the frequency is being underpredicted and the translational velocity is being overpredicted by the numerical simulation. The two-fluid model is a one-dimensional approach of a physical problem that has intrinsically three-dimensional effects. Some of those effects are not being captured by the mathematical model herein presented due to its simplicity in representing the flow as a one-dimensional point of view. One effect that is present in the slug flow, is the recirculation zone in the slug front. The slug body, that is moving faster than the liquid film ahead of it, lifts it up and accelerates it generating a turbulent mixing zone. This phenomenon causes loss of

momentum in transverse directions that the two-fluid model is not capable to represent, and as a consequence, it impacts in the slug flow characteristics. Another detail that could explain the lower frequency values is that the gas phase remains in the gas pocket instead of in the slug body because of the lack of a gas entrainment model. This makes the gas pocket larger and the slug bodies more spares. A third possible attempt to improve the numerical results in the comparison with experiments is to increase the number of equations in the mathematical model, so that a momentum equation is added for the bubble and droplet phases. This approach will allow each phase to move with its own velocity and the slip velocity that occurs in the real flow will be embedded in the model explicitly, without the need to use empirical correlations.

To conclude, although the simulations are presenting relevant differences, the numerical model is showing promising results. The simulations that are performed in this work indicate that the numerical model is generating slugs and it keeps generating them through time, affirming the capability of the two-fluid model in predicting the intermittent flow automatically. The intermittent flow dynamics is very complex and presents an unsteady behavior with uncommon characteristics. Even though such complexity cannot be perfectly modelled with a one-dimensional perspective, the obtained results are showing that the two-fluid model is a good and reliable tool to estimate this flow behavior.

8.2 Recommendations for Future Work

A natural recommendation for future work would be the improvement of the mathematical model. The first modification should be the gas entrainment model that encompasses the presence of bubbles in the slug body. The 7E2P model might be a good start, if computational time is not the main concern, by including momentum equations for all the phases, giving rise to a 9E2P (nine-equation) model. The dynamics and shape of the bubble phase can be modeled in order to try to get better results in the comparison with experiments. Moreover, simulations with higher values of α_B and α_D are imperative, and they must include suitable friction correlations for the interaction among the four phases.

The 5E2P model could be improved with the inclusion of terms in the existing equations that could account for the momentum losses due to the recirculation zone in the slug front, for instance, as an alternative to try to represent better the effects that are not

being considered at the moment. This improvement requires a deep sensitivity study of the model to verify which term should be added to the equations.

Another improvement in the model that could be beneficial is the inclusion of mass transfer terms between the phases. Obviously, the inclusion of these terms is directly influenced by the necessity of them in the desired application of the mathematical model. Moreover, if thermal effects are important to be considered, the energy equations could be added as well. It is worth mentioning that the hyperbolicity analysis needs to be redone whenever a new equation is added to the mathematical model.

Regarding the boundary conditions imposition, a new strategy can be adopted to avoid the boundary effect near the outlet that was observed during the simulations. The boundary conditions implemented in this work are based on the standard strategy presented in the literature, such as Omgba-Essama (2004), Ferrari *et al.* (2017), Figueiredo *et al.* (2017), as described in section 4.4. In this strategy, the values of the flow variables that are not prescribed as boundary conditions are replications from the neighbor discretized inner cell. Therefore, indirectly, the ghost and its neighbor cells have the same values which implies in a null derivative condition. In order to improve this strategy, an idea would be to prescribe the ghost cell value by doing an extrapolation of this quantity based on the derivative from the neighbor inner cell.

References

Abbaspour, M., Chapman, K.S. and Glasgow, L.A., 2010, “Transient modeling of non-isothermal, dispersed two-phase flow in natural gas pipelines”, Applied Mathematical Modelling, v. 34, pp. 495–507.

Almeida, V. R., Conte, M. G., Barbuto, F. A. A., Cozin, C., Morales, R. E. M., 2017, “Numerical simulation of two-phase slug flow from horizontal to downward inclined pipe using a hybrid code based on slug tracking and two-fluid methodologies”, Proceedings of ASME 2017 Fluids Engineering Division Summer Meeting, Hawaii, August.

Ansari, M.R. and Daramizadeh, A., 2013, “Numerical simulation of compressible two-phase flow using a diffuse interface method”, International Journal of Heat and Fluid Flow, v. 42, pp. 209–223.

Aql, A., 2020, “Intermittent structure characteristics and Evolution in a slightly upward inclined pipe at a high pressure”, Ph.D. Dissertation, The University of Tulsa, Tulsa, Oklahoma, U.S.A.

Aziz, H.Z., Naghashzadegan, M., Shokri, V., 2018, “Comparison of the hyperbolic range of two-fluid models on two-phase gas-liquid flows”, International Journal of Engineering, v. 31, no.1, pp. 144-156.

Baer, M.R. and Nunziato, J.W., 1986, “A two-phase mixture theory for the deflagration-to-detonation transition (DDT) in reactive granular materials”, Int. J. Multiphase flow, v.12, n. 6, pp. 861-889.

Barnea, D., and Taitel, Y., 1993, “A model for slug length distribution in gas-liquid slug flow”, International Journal of Multiphase Flow, v.19, n. 5, pp. 829-838.

Barnea, D., and Taitel, Y., 1994, “Interfacial and structural stability of separated flow”, International Journal of Multiphase Flow, v.20, pp. 387-414.

Bendiksen, K.H., 1984, “An experimental investigations of the motion of long bubbles in inclined tubes”, Int. J. Multiphase flow, v.10, n. 4, pp. 467-483.

Bestion, D., 1990, “The physical closure laws in the CATHARE code”, Nuclear Engineering and Design, v.124, pp. 229–245.

Bonizzi, M., Issa, R.I., 2003, “A model for simulating gas bubble entrainment in two-phase horizontal slug flow”, International Journal of Multiphase Flow, v.29, pp. 1685–1717.

Brito, R., 2012, “Effect of medium oil viscosity on two-phase oil-gas flow behavior in horizontal pipes”, M.Sc. Thesis, The University of Tulsa, Tulsa, Oklahoma, U.S.A.

Clerc, S., 2000, “Numerical Simulation of the Homogeneous Equilibrium Model for Two-Phase Flows”, Journal of Computational Physics, v.161, pp. 354-375.

Coelho, R. M. L., Lage, P. L. C., Silva Telles, A., 2010, “A comparison of hyperbolic solvers II: AUSM-type and hybrid Lax-Wendroff-Lax-Friedrichs methods for two-phase flows”, Brazilian Journal of Chemical Engineering, v.27, pp. 153-171.

Cook, M., Behnia, M., 2000, “Pressure drop calculation and modelling of inclined intermittent gas-liquid flow”, Chemical Engineering Science, v.55, pp. 4699-4708.

Coquel, F., El Amine, K., Godlewski, E., Perthame, B., Rascle, P., 1997, “A numerical method using upwind schemes for the resolution of two-phase flows”, Journal of Computational Physics, v. 136, pp. 272-288.

Dieck, R.H., 2007, Measurement Uncertainty: Methods and Applications. ISA.

Drew, D.A. and Passman, S.L., 1999, Theory of Multicomponent Fluids. Springer.

Dukler, A. and Hubbard, M., 1975, “A model for gas-liquid slug flow in horizontal and near-horizontal tubes”, Industrial & Engineering Chemistry Fundamentals, v. 14, n. 4, pp. 337-347.

Evje, S., Flätten, T., 2003, “Hybrid flux-splitting schemes for a common two-fluid model”, Journal of Computational Physics, v.192, pp. 175–210.

Fabre, J., 1994, “Advancements of two-phase slug flow modeling”, Paper SPE 27961, University of Tulsa Centennial Petroleum Engineering Symposium, Tulsa, OK, U.S.A., pp.29-31, August.

Fabre, J., Line, A., Peresson, L., 1989, “Two-fluid/two-flow-pattern model for transient gas-liquid flow in pipes”. 4th BHRA Multiphase Flow International Conference, Cranfield University, London, UK, pp. 269-289, June.

Fan, Y., 2017, “A study of onset of liquid accumulation and pseudo-slug flow characterization”, Ph.D. Dissertation, The University of Tulsa, Tulsa, Oklahoma, U.S.A.

Ferrari, M., Bonzanini, A., Poesio, P., 2017, “A 5-equation, transient, hyperbolic, 1-dimensional model for slug capturing in pipes”, International Journal of Numerical Methods in Fluids, v. 85, pp. 327–362.

Ferrari, M., Bonzanini, A., Poesio, P., 2019, “A slug capturing method in unconventional scenarios: The 5ESCARGOTS code applied to non-Newtonian fluids, high viscosity oils and complex geometries”, Petroleum, v. 5, pp. 171–177.

Figueiredo, A.B., Baptista, R.M., Rachid, F.B.F. and Bodstein, G.C.R., 2017, “Numerical simulation of stratified-pattern two-phase flow in gas pipelines using a two-fluid model”, International Journal of Multiphase Flow, v. 88, pp. 30 – 49.

Freitas, R.V.N., 2017, “Estudo de modelos de dois fluidos acoplados ao método FCT em escoamentos bifásicos”, In portuguese, M.Sc. Dissertation, Universidade Federal do Rio de Janeiro, Rio de Janeiro, Brazil.

Furfaro, D., Saurel, R., 2015, “A simple HLLC-type Riemann solver for compressible non-equilibrium two-phase flows”, Computer & Fluids, v. 111, pp. 159–178.

Gonçalves, G. F. N., Baungartner, R., Loureiro, J. B. R., Silva Freire, A. P., 2018, “Slug flow models: Feasible domain and sensitivity to input distributions”, Journal of Petroleum Science and Engineering, v. 169, pp. 705-724.

Gokcal, B., 2008, “An experimental and theoretical investigation of slug flow for high oil viscosity in horizontal pipes”, Ph.D. Dissertation, The University of Tulsa, Tulsa, Oklahoma, U.S.A.

Harmathy, T. Z., 1960, “Velocity of large drops and bubbles in media of infinite or restricted extent”, A.I.Ch.E. Journal, v. 6, pp. 281-288.

Harten, A., 1983, “High resolution schemes for hyperbolic conservation laws”, Journal of Computational Physics, v. 49, pp. 357-393.

Ishii, M. and Hibiki, T., 2003, “One-dimensional drift-flux model and constitutive equations for relative motion between phases in various two-phase flow regimes”, International Journal of Heat and Mass Transfer, v. 46, pp. 4935-4948.

Ishii, M. and Hibiki, T., 2006, Thermo-Fluid Dynamics of Two-Phase Flow, 1st ed. New York, Springer Science.

Issa, R.I. and Kempf, M.H.W., 2003, “Simulation of slug flow in horizontal and nearly horizontal pipes with the two-fluid model”, International Journal of Multiphase Flow, v.29, pp. 69-95.

Jeffrey, A., 1976, Quasilinear Hyperbolic Systems and Waves, London, Pitman Publishing.

Kim, T., 2019, “Detailed flow field analysis of air and highly viscous liquid slug flow in horizontal pipes”, Ph.D. Dissertation, The University of Tulsa, Tulsa, Oklahoma, U.S.A.

Kitamura, K., Liou, M.-S., 2012, “Comparative study of AUSM-family schemes in compressible multiphase flow simulations”, Seventh International Conference on Computational Fluid Dynamics, Big Island, Hawaii, July.

Kjeldby, T., Henkes, R., Nydal, O. J., 2013, “Lagrangian slug flow modeling and sensitivity on hydrodynamic slug initiation mthods in a severe slugging case”, International Journal of Multiphase Flow, v.53, pp. 29-35.

LeVeque, R., 2004, Finite-volume methods for hyperbolic problems, Cambridge University Press, U.K.

Lin, P. Y., Hanratty, T. J., 1987, “Effect of pipe diameter on flow patterns for air-water flow in horizontal pipes”, International Journal of Multiphase Flow, v.13, pp. 549-563.

Liou, M-S., 1996, “A sequel to AUSM: AUSM+”, Journal of Computational Physics, v.129, pp. 364-382.

Liou, M-S., Steffen, C. J., 1993, “A new flux splitting scheme”, Journal of Computational Physics, v.107, pp. 23-39.

Loilier, P., Omgba-Essama, C., Thompson, C., 2005, “Numerical experiments of two-phase flow in pipelines with a two-fluid compressible model”, Proceedings of 12th International Conference on Multiphase Production Technology, Barcelona, May.

Masella, J.M., Tran, Q.H, Ferre, D. and Pauchon, C., 1998, “Transient simulation of two-phase flows in pipes”. International Journal Multiphase Flow, v. 24, pp. 739-755.

Moreiras, J., Pereyra, E., Sarica, C., Torres, C. F., 2014, “Unified drift velocity closure relationship for large bubbles rising in stagnant viscous fluids in pipes”, Journal of Petroleum Science and Engineering, v. 124, pp. 359-366.

Munkejord, S., 2005, “Analysis of the two-fluid model and the drift-flux model for numerical calculation of two-phase flow”. Ph.D. Thesis, NTNU Norwegian University of Science and Technology, Trondheim, Norway.

Munkejord, S.T., 2007, “Comparison of Roe-type methods for solving the two-fluid model with and without pressure relaxation”, Computer & Fluids, v. 36, pp. 1061-1080.

Munkejord, S.T., 2010, “A numerical study of two-fluid models with pressure and velocity relaxation”, Advances in Applied Mathematics and Mechanics, v. 2, pp. 131-159.

Munkejord, S.T., Evje, S., Flatten, T., 2009, “A MUSTA scheme for a non-conservative two-fluid model”, SIAM Journal on Scientific Computing, v. 31, pp. 2587-2622.

Nieckele, A.O., Carneiro, J.N.E., Chucuya, R.C., Azevedo, J.H.P., 2013, “Initiation of statistical evolution of horizontal slug flow with a two-fluid model”, Journal of Fluids Engineering, v. 135, pp. 121302 1-121302 11.

Nydal, O.J., Banerjee, S., 1996, “Dynamic slug tracking simulations for gas-liquid flow in pipelines”, Chemical Engineering Communications, v. 141-142, pp. 13-39.

Omgba-Essama, C., 2004, Numerical Modelling of Transient Gas-Liquid Flows (Application to Stratified & Slug Flow Regimes), PhD Thesis, School of Engineering Applied Mathematics and Computing Group, Cranfield University, Bedford, United Kingdom.

Ortega Malca, A. J., 2004, “Análise de padrão slug em tubulações horizontais utilizando o modelo de dois fluidos”, In portuguese, M.Sc. Dissertation, Pontifícia Universidade Católica do Rio de Janeiro, Rio de Janeiro, Brazil.

Paillère, H., Corre, C., García Cascales, J. R., 2003, “On the extension of the AUSM+ scheme to compressible two-fluid models”, Computer & Fluids, v. 32, pp. 891-916.

Prosperetti, A., 2007, “Computational Methods for Multiphase Flow”, Edited by A. Prosperetti and G. Tryggvason, Chapter 11, Cambridge University Press, Cambridge.

Ransom, V.H., 1987, “Numerical benchmark test no. 2.1: faucet flow”, Multiphase Science and Technology, v. 3, pp. 465-467.

Ransom, V. H. and Hicks, D. L., 1984, “Hyperbolic two-pressure models for two-phase flow”, Journal of Computational Physics, v. 53, pp. 124-151.

Renault, F., 2007, “A lagrangian slug capturing scheme for gas-liquid flows in pipes”, Ph.D. Thesis, Department of Energy and Process Engineering, Norwegian University of Science and Technology (NTNU), Trondheim, Norway.

Roe, P. L., 1981, “Approximate Riemann solvers, parameter vectors, and difference schemes”, Journal of Computational Physics, v. 43, pp. 357-372.

Rosa, E. S., Mazza, R. A., Morales, R. E. M., Rodrigues, H. T., Cozin, C., 2015, “Analysis of slug tracking model for gas-liquid flows in a pipe”, Journal of Brazilian Society of Mechanical Sciences and Engineering, DOI: 10.1007/s40430-015-0331-7.

Roullier, D., 2017, “Slug flow analysis in vertical large diameter pipes”, M.Sc. Thesis, The University of Tulsa, Tulsa, Oklahoma, U.S.A.

Santim, C. G. S., Rosa, E. S., 2015, “Roe-type Riemann solver for gas-liquid flows using drift-flux model with an approximate form of the Jacobian matrix”, International Journal for Numerical Methods in Fluids, v. 80, pp. 536–568.

Saurel, R. and Abgrall, R., 1999, “A multiphase Godunov method for compressible multifluid and multiphase flows”, Journal of Computational Physics, v. 150, pp. 425–467.

Shoham, O., 2006, Mechanistic modeling of gas-liquid two-phase flow in pipes. SPE Book.

Simões, E.F., Carneiro, J.N.E. and Nieckele, A.O, 2014, “Numerical prediction of non-boiling heat transfer in horizontal stratified and slug flow by Two-Fluid Model”, International Journal of Heat and Fluid Flow, v. 47, pp. 134-145.

Soedarmo, A., 2019, “Gas-oil flow in upward-inclined pipes: pseudo-slug flow modeling and upscaling studies”, Ph.D. Dissertation, The University of Tulsa, Tulsa, Oklahoma, U.S.A.

Soedarmo, A., Fan, Y., Pereyra, E., Sarica, C., 2018, “A unit cell model for gas-liquid pseudo-slug flow in pipes”, Journal of Natural Gas Science and Engineering, v. 60, pp. 125-143.

Sondermann, C.N., 2016, “Simulação de escoamento bifásico em gasodutos com uma equação da energia para a mistura utilizando o método numérico FCT”, In portuguese, M.Sc. Dissertation, Universidade Federal do Rio de Janeiro, Rio de Janeiro, Brazil.

Sondermann, C.N., Baptista, R.M., Rachid, F.B.F. and Bodstein, G.C.R., 2019, “Numerical simulation of non-isothermal two-phase flow in pipelines using a two-fluid model”, Journal of Petroleum Science and Engineering, v. 173, pp. 298-314.

Spedding, P.L., Hand, N.P., 1997, “Prediction in stratified gas-liquid co-current flow in horizontal pipelines”, International Journal of Heat and Mass Transfer, v. 40, pp. 1923-1935.

Taitel, Y. and Dukler, A. E.,1976, “A model for predicting flow regime transitions in horizontal and near-horizontal gas-liquid flow”. AIChE Journal, v. 22, n. 1, pp. 47-55, January.

Taitel, Y., Barnea, D., 1990, “Two-phase slug flow”, Advances in Heat Transfer, v. 20, pp. 83-132.

Taitel, Y., Vierkandt, S., Shoham, O., Brill, J. P., 1990, “Severe slugging in a riser system: experiments and modeling”, International Journal of Multiphase Flow, v. 16, pp. 57-68.

Toro, E. F., 1999, Riemann Solvers and Numerical Methods for Fluid Dynamics. Springer.

van Leer, B., 1974, “Towards the ultimate conservative difference scheme II. Monotonicity and conservation combined in a second-order scheme”, Journal of Computational Physics, v. 14, pp. 361-370.

Wada, Y., Liou, M-S., 1997, “An accurate and robust flux splitting scheme for shock and contact discontinuities”, Society for Industrial and Applies Mathematics, v. 18, n. 3, pp. 633-657.

Zhang, H. Q., Wang, Q., Sarica, C., Brill, J. P., 2003, “Unified model for gas-liquid pipe flow via slug dynamics – Part 1: model development”, ASME Journal of Energy Resources Technology, v. 125, pp. 266-273.

Zhu, Q., 2019, “Intermittent flow analysis in inclined large diameter pipes”, M.Sc. Thesis, The University of Tulsa, Tulsa, Oklahoma, U.S.A.

Zou, L., Zahao, H., Zhang, H., 2016, “New analytical solutions to the two-phase water faucet problem”, Progress in Nuclear Energy, v. 91, pp. 389-398.

Appendix A – Detailed Roe Scheme

In an algebraic point of view, it is not simple to obtain the Jacobian matrix, **A**, for the 5E2P and 7E2P mathematical models. A more direct way is to write the system of equations as a function of the primitive variables vector, **W**, as

$$\frac{\partial \mathbf{W}}{\partial t} + \mathbf{B}(\mathbf{W})\frac{\partial \mathbf{W}}{\partial x} = \varsigma(\mathbf{W}). \tag{A.1}$$

From Eq. (A.1), the matrix **A** can be determined by first calculating the matrices, **J** and its inverse matrix, $\mathbf{J^{-1}}$ defined as

$$\mathbf{J} \equiv \frac{\partial \mathbf{Q}}{\partial \mathbf{W}} \text{ e } \mathbf{J^{-1}} \equiv \frac{\partial \mathbf{W}}{\partial \mathbf{Q}}, \tag{A.2}$$

and, using the chain rule in Eq. (A.1),

$$\frac{\partial \mathbf{W}}{\partial \mathbf{Q}}\frac{\partial \mathbf{Q}}{\partial t} + \mathbf{B}(\mathbf{W})\frac{\partial \mathbf{W}}{\partial \mathbf{Q}}\frac{\partial \mathbf{Q}}{\partial x} = \varsigma(\mathbf{W}). \tag{A.3}$$

Using Eq. (A.2) in Eq. (A.3),

$$\mathbf{J^{-1}}\frac{\partial \mathbf{Q}}{\partial t} + \mathbf{B}(\mathbf{W})\mathbf{J^{-1}}\frac{\partial \mathbf{Q}}{\partial x} = \varsigma(\mathbf{W}). \tag{A.4}$$

Eq. (A.4) implies that

$$\mathbf{A} = \mathbf{J}\mathbf{B}\mathbf{J^{-1}} \tag{A.5}$$

and

$$\mathbf{S} = \mathbf{J}\boldsymbol{\eta}. \tag{A.6}$$

To determine **B**, the system of equation should be written as

$$\mathbf{C}\frac{\partial \mathbf{W}}{\partial t} + \mathbf{D}\frac{\partial \mathbf{W}}{\partial x} = \mathbf{E}(\mathbf{W}), \tag{A.7}$$

where **E = S**. For the 5E2P model,

$$\mathbf{C} = \begin{bmatrix} 1 & 0 & 0 & 0 & 0 \\ \rho_G & \alpha_G/c_G^2 & 0 & 0 & 0 \\ -\rho_L & 0 & \alpha_L/c_L^2 & 0 & 0 \\ 0 & 0 & 0 & \alpha_G\rho_G & 0 \\ 0 & 0 & 0 & 0 & \alpha_L\rho_L \end{bmatrix}, \tag{A.8}$$

and

$$\mathbf{D} = \begin{bmatrix} u_I & 0 & 0 & 0 & 0 \\ u_G\rho_G & \alpha_G u_G/c_G^2 & 0 & \alpha_G\rho_G & 0 \\ -u_L\rho_L & 0 & \alpha_L u_L/c_L^2 & 0 & \alpha_L\rho_L \\ \Delta p_{IG} & \alpha_G & 0 & \alpha_G\rho_G u_G & 0 \\ -\Delta p_{IL} & 0 & \alpha_L & 0 & \alpha_L\rho_L u_L \end{bmatrix}. \tag{A.9}$$

Comparing Eq. (A.1) and Eq. (A.7),

$$\mathbf{B} = \mathbf{C^{-1}D}, \tag{A.10}$$

and

$$\boldsymbol{\eta} = \mathbf{C^{-1}E}. \tag{A.11}$$

Then,

$$\mathbf{B} = \begin{bmatrix} u_I & 0 & 0 & 0 & 0 \\ \frac{c_G^2(u_G - u_I)\rho_G}{\alpha_G} & u_G & 0 & c_G^2\rho_G & 0 \\ -\frac{c_L^2(u_L - u_I)\rho_L}{\alpha_L} & 0 & u_L & 0 & c_L^2\rho_L \\ \frac{\Delta p_{IG}}{\alpha_G\rho_G} & \frac{1}{\rho_G} & 0 & u_G & 0 \\ -\frac{\Delta p_{IL}}{\alpha_L\rho_L} & 0 & \frac{1}{\rho_L} & 0 & u_L \end{bmatrix}. \quad \text{(A.12)}$$

Identifying the transformation matrix, **J** as

$$\mathbf{J} = \begin{bmatrix} 1 & 0 & 0 & 0 & 0 \\ \rho_G & \alpha_G/c_G^2 & 0 & 0 & 0 \\ -\rho_L & 0 & \alpha_L/c_L^2 & 0 & 0 \\ u_G\rho_G & \alpha_G u_G/c_G^2 & 0 & \alpha_G\rho_G & 0 \\ -u_L\rho_L & 0 & \alpha_L u_L/c_L^2 & 0 & \alpha_L\rho_L \end{bmatrix}, \quad \text{(A.13)}$$

it is possible to obtain the Jacobian matrix, **A**,

$$\mathbf{A}(\mathbf{Q}) = \begin{bmatrix} u_I & 0 & 0 & 0 & 0 \\ 0 & 0 & 0 & 1 & 0 \\ 0 & 0 & 0 & 0 & 1 \\ \Delta p_{IG} - \rho_G c_G^2 & c_G^2 - u_G^2 & 0 & 2u_G & 0 \\ -\Delta p_{IL} + \rho_L c_L^2 & 0 & c_L^2 - u_L^2 & 0 & 2u_L \end{bmatrix}. \quad \text{(A.14)}$$

The eigenvalues are analytical expressions, given by: $\lambda_1 = u_I$, $\lambda_2 = u_G - c_G$, $\lambda_3 = u_G + c_G$, $\lambda_4 = u_L - c_L$ e $\lambda_5 = u_L + c_L$. The eigenvectors of matrix **A**, with the right eigenvectors, **R**, in columns, can be expressed as

$$\mathbf{R} = \begin{bmatrix} \frac{(c_L+u_I-u_L)(c_L-u_I+u_L)}{u_I(\Delta p_{IL}-\rho_L c_L^2)} & 0 & 0 & 0 & 0 \\ -\frac{(c_L+u_I-u_L)(c_L-u_I+u_L)(\Delta p_{IG}-\rho_G c_G^2)}{u_I(c_G+u_I-u_G)(c_G-u_I+u_G)(\Delta p_{IL}-\rho_L c_L^2)} & \frac{1}{u_G-c_G} & \frac{1}{u_G+c_G} & 0 & 0 \\ \frac{1}{u_I} & 0 & 0 & \frac{1}{u_L-c_L} & \frac{1}{u_L+c_L} \\ \frac{(c_L+u_I-u_L)(c_L-u_I+u_L)(-\Delta p_{IG}+\rho_G c_G^2)}{(c_G+u_I-u_G)(c_G-u_I+u_G)(\Delta p_{IL}-\rho_L c_L^2)} & 1 & 1 & 0 & 0 \\ 1 & 0 & 0 & 1 & 1 \end{bmatrix}, \quad \text{(A.15)}$$

and being the matrix $\mathbf{R^{-1}}$ the inverse matrix of **R**, given by

$$\mathbf{R^{-1}} = \begin{bmatrix} \frac{u_I(\Delta p_{IL}-\rho_L c_L^2)}{(c_L+u_I-u_L)(c_L-u_I+u_L)} & 0 & 0 & 0 & 0 \\ \frac{(c_G-u_G)(-\Delta p_{IG}+\rho_G c_G^2)}{2c_G(c_G+u_I-u_G)} & \frac{u_G^2-c_G^2}{2c_G} & 0 & \frac{c_G-u_G}{2c_G} & 0 \\ -\frac{(c_G+u_G)(-\Delta p_{IG}+\rho_G c_G^2)}{2c_G(c_G-u_I+u_G)} & \frac{c_G^2-u_G^2}{2c_G} & 0 & \frac{c_G+u_G}{2c_G} & 0 \\ -\frac{(c_L-u_L)(-\Delta p_{IL}+\rho_L c_L^2)}{2c_L(c_L+u_I-u_L)} & 0 & \frac{u_L^2-c_L^2}{2c_L} & 0 & \frac{c_L-u_L}{2c_L} \\ \frac{(c_L+u_L)(-\Delta p_{IL}+\rho_L c_L^2)}{2c_L(c_L-u_I+u_L)} & 0 & \frac{c_L^2-u_L^2}{2c_L} & 0 & \frac{c_L+u_L}{2c_L} \end{bmatrix}. \quad \text{(A.16)}$$

For the 7E2P model, the Eqs. (A.8 – A.9) and Eqs. (A.12 – A.16) are written as

$$\mathbf{C} = \begin{bmatrix} 1 & 0 & 1 & 0 & 0 & 0 & 0 \\ \rho_G & 0 & 0 & \alpha_G/c_G^2 & 0 & 0 & 0 \\ -\rho_L & -\rho_L & -\rho_L & 0 & \alpha_L/c_L^2 & 0 & 0 \\ 0 & 0 & 0 & 0 & 0 & (\alpha_G\rho_G+\alpha_D\rho_L) & 0 \\ 0 & 0 & 0 & 0 & 0 & 0 & (\alpha_L\rho_L+\alpha_B\rho_G) \\ 0 & \rho_G & 0 & 0 & \alpha_B/c_G^2 & 0 & 0 \\ 0 & 0 & \rho_L & \alpha_D/c_L^2 & 0 & 0 & 0 \end{bmatrix}. \quad \text{(A.17)}$$

$$\mathbf{D} = \begin{bmatrix} u_I & 0 & u_I & 0 & 0 & 0 & 0 \\ \rho_G u_G & 0 & 0 & \alpha_G u_G/c_G^2 & 0 & \alpha_G\rho_G & 0 \\ -\rho_L u_L & -\rho_L u_L & -\rho_L u_L & 0 & \alpha_L u_L/c_L^2 & 0 & \alpha_L\rho_L \\ \Delta p_{IG} & 0 & \Delta p_{IG} & \alpha_G+\alpha_D & 0 & (\alpha_G\rho_G+\alpha_D\rho_L)u_G & 0 \\ -\Delta p_{IL} & 0 & -\Delta p_{IL} & 0 & \alpha_L+\alpha_B & 0 & (\alpha_L\rho_L+\alpha_B\rho_G)u_L \\ 0 & \rho_G u_L & 0 & 0 & \alpha_B u_L/c_G^2 & 0 & \alpha_B\rho_G \\ 0 & 0 & \rho_L u_G & \alpha_D u_G/c_L^2 & 0 & \alpha_D\rho_L & 0 \end{bmatrix}. \quad \text{(A.18)}$$

Defining $X \equiv c_G^2\alpha_D\rho_G + c_L^2\alpha_G\rho_L$ and $Y \equiv c_G^2\alpha_L\rho_G + c_L^2\alpha_B\rho_L$ to obtain matrix **B**,

$$\mathbf{B} = \begin{bmatrix} \frac{c_G^2 u_G \alpha_D \rho_G + c_L^2 u_I \alpha_G \rho_L}{X} & 0 & \frac{c_L^2 (u_I - u_G)\alpha_G \rho_L}{X} & 0 & 0 & \frac{\alpha_G \alpha_D (c_G^2 \rho_G - c_L^2 \rho_L)}{X} & 0 \\ \frac{c_L^2 (u_L - u_I)\alpha_B \rho_L}{Y} & u_L & \frac{c_L^2 (u_L - u_I)\alpha_B \rho_L}{Y} & 0 & 0 & 0 & \frac{\alpha_B \alpha_L (c_G^2 \rho_G - c_L^2 \rho_L)}{Y} \\ \frac{c_G^2 (u_I - u_G)\alpha_D \rho_G}{X} & 0 & \frac{c_G^2 u_I \alpha_D \rho_G + c_L^2 u_G \alpha_G \rho_L}{X} & 0 & 0 & \frac{\alpha_G \alpha_D (c_L^2 \rho_L - c_G^2 \rho_G)}{X} & 0 \\ \frac{c_G^2 c_L^2 (u_G - u_I)\rho_L \rho_G}{X} & 0 & \frac{c_G^2 c_L^2 (u_G - u_I)\rho_L \rho_G}{X} & u_G & 0 & \frac{c_G^2 c_L^2 (\alpha_D + \alpha_G)\rho_L \rho_G}{X} & 0 \\ \frac{c_G^2 c_L^2 (u_I - u_L)\rho_L \rho_G}{Y} & 0 & \frac{c_G^2 c_L^2 (u_I - u_L)\rho_L \rho_G}{Y} & 0 & u_L & 0 & \frac{c_G^2 c_L^2 (\alpha_B + \alpha_L)\rho_L \rho_G}{Y} \\ \frac{\Delta p_{IG}}{\alpha_G \rho_G + \alpha_D \rho_L} & 0 & \frac{\Delta p_{IG}}{\alpha_G \rho_G + \alpha_D \rho_L} & \frac{\alpha_D + \alpha_G}{\alpha_G \rho_G + \alpha_D \rho_L} & 0 & u_G & 0 \\ -\frac{\Delta p_{IL}}{\alpha_B \rho_G + \alpha_L \rho_L} & 0 & -\frac{\Delta p_{IL}}{\alpha_B \rho_G + \alpha_L \rho_L} & 0 & \frac{\alpha_B + \alpha_L}{\alpha_B \rho_G + \alpha_L \rho_L} & 0 & u_L \end{bmatrix} \tag{A.19}$$

$$\mathbf{J} = \begin{bmatrix} 1 & 0 & 1 & 0 & 0 & 0 & 0 \\ \rho_G & 0 & 0 & \alpha_G / c_G^2 & 0 & 0 & 0 \\ -\rho_L & -\rho_L & -\rho_L & 0 & \alpha_L / c_L^2 & 0 & 0 \\ \rho_G u_G & 0 & \rho_L u_G & \frac{\alpha_G u_G}{c_G^2} + \frac{\alpha_D u_G}{c_L^2} & 0 & (\alpha_G \rho_G + \alpha_D \rho_L) & 0 \\ -\rho_L u_L & (\rho_G u_L - \rho_L u_L) & -\rho_L u_L & 0 & \frac{\alpha_L u_L}{c_L^2} + \frac{\alpha_B u_L}{c_G^2} & 0 & (\alpha_L \rho_L + \alpha_B \rho_G) \\ 0 & \rho_G & 0 & 0 & \alpha_B / c_G^2 & 0 & 0 \\ 0 & 0 & \rho_L & \alpha_D / c_L^2 & 0 & 0 & 0 \end{bmatrix}. \tag{A.20}$$

Using the definition of X and Y that were defined to obtain the matrix **B**, and adding $Z \equiv c_G^2 c_L^2 (\alpha_D + \alpha_G)$ and $K \equiv c_G^2 c_L^2 (\alpha_B + \alpha_L)$, to obtain the Jacobian matrix for the 7E2P model

$$\mathbf{A} = \begin{bmatrix} u_I & 0 & 0 & 0 & 0 & 0 & 0 \\ 0 & \frac{\alpha_D u_G \rho_L}{\alpha_G \rho_G + \alpha_D \rho_L} & 0 & \frac{\alpha_G \rho_G}{\alpha_G \rho_G + \alpha_D \rho_L} & 0 & 0 & -\frac{\alpha_G u_G \rho_G}{\alpha_G \rho_G + \alpha_D \rho_L} \\ 0 & 0 & \frac{\alpha_B u_L \rho_G}{\alpha_L \rho_L + \alpha_B \rho_G} & 0 & \frac{\alpha_L \rho_L}{\alpha_L \rho_L + \alpha_B \rho_G} & -\frac{\alpha_L u_L \rho_L}{\alpha_L \rho_L + \alpha_B \rho_G} & 0 \\ \Delta p_{IG} - \frac{Z \rho_L \rho_G}{X} & \frac{Z \rho_L}{X} - u_G^2 & 0 & 2u_G & 0 & 0 & \frac{Z \rho_G}{X} - u_G^2 \\ -\Delta p_{IL} + \frac{K \rho_L \rho_G}{Y} & 0 & \frac{K \rho_G}{Y} - u_L^2 & 0 & 2u_L & \frac{K \rho_L}{Y} - u_L^2 & 0 \\ 0 & 0 & -\frac{\alpha_B u_L \rho_G}{\alpha_B \rho_G + \alpha_L \rho_L} & 0 & \frac{\alpha_B \rho_G}{\alpha_B \rho_G + \alpha_L \rho_L} & \frac{\alpha_L u_L \rho_L}{\alpha_B \rho_G + \alpha_L \rho_L} & 0 \\ 0 & -\frac{\alpha_D u_G \rho_L}{\alpha_G \rho_G + \alpha_D \rho_L} & 0 & \frac{\alpha_D \rho_L}{\alpha_G \rho_G + \alpha_D \rho_L} & 0 & 0 & \frac{\alpha_G u_G \rho_G}{\alpha_G \rho_G + \alpha_D \rho_L} \end{bmatrix} \tag{A.21}$$

The eigenvalues of the matrix **A** are: $\lambda_1 = u_I,\ \lambda_2 = u_G, \lambda_3 = u_L, \lambda_4 = u_G - \sqrt{\frac{c_G^2 c_L^2 (\alpha_D+\alpha_G)^2 \rho_L \rho_G}{(\alpha_G \rho_G + \alpha_D \rho_L) X}}$, $\lambda_5 = u_G + \sqrt{\frac{c_G^2 c_L^2 (\alpha_D+\alpha_G)^2 \rho_L \rho_G}{(\alpha_G \rho_G + \alpha_D \rho_L) X}}$, $\lambda_6 = u_L - \sqrt{\frac{c_G^2 c_L^2 (\alpha_B+\alpha_L)^2 \rho_L \rho_G}{(\alpha_B \rho_G + \alpha_L \rho_L) Y}}$ e $\lambda_7 = u_L + \sqrt{\frac{c_G^2 c_L^2 (\alpha_B+\alpha_L)^2 \rho_L \rho_G}{(\alpha_B \rho_G + \alpha_L \rho_L) Y}}$.

$$\mathbf{R} =$$

$$\begin{bmatrix}
\frac{(-u_i^2+2u_iu_G-\lambda_4\lambda_5)(\alpha_G\rho_G+\alpha_D\rho_L)}{\alpha_D\rho_L(-\Delta p_{IG}+\frac{Z\rho_L\rho_G}{X})} & 0 & 0 & 0 & 0 & 0 & 0 \\
\frac{\alpha_G\rho_G}{\alpha_D\rho_L} & -\frac{\rho_G}{\rho_L} & 0 & \frac{\alpha_G\rho_G}{\alpha_D\rho_L} & \frac{\alpha_G\rho_G}{\alpha_D\rho_L} & 0 & 0 \\
\frac{\alpha_L(\Delta p_{IL}-\frac{K\rho_L\rho_G}{Y})(u_i^2-2u_iu_G+\lambda_4\lambda_5)(\alpha_G\rho_G+\alpha_D\rho_L)}{\alpha_D(\Delta p_{IG}-\frac{Z\rho_L\rho_G}{X})(-u_i^2+2u_iu_L-\lambda_6\lambda_7)(\alpha_B\rho_G+\alpha_L\rho_L)} & 0 & -\frac{\rho_L}{\rho_G} & 0 & 0 & \frac{\alpha_L\rho_L}{\alpha_B\rho_G} & \frac{\alpha_L\rho_L}{\alpha_B\rho_G} \\
\frac{u_i(\alpha_G\rho_G+\alpha_D\rho_L)}{\alpha_D\rho_L} & -\frac{u_G(\rho_G-\rho_L)}{\rho_L} & 0 & \frac{\lambda_4(\alpha_G\rho_G+\alpha_D\rho_L)}{\alpha_D\rho_L} & \frac{\lambda_5(\alpha_G\rho_G+\alpha_D\rho_L)}{\alpha_D\rho_L} & 0 & 0 \\
-\frac{u_i(\Delta p_{IL}-\frac{K\rho_L\rho_G}{Y})(u_i^2-2u_iu_G+\lambda_4\lambda_5)(\alpha_G\rho_G+\alpha_D\rho_L)}{\alpha_D\rho_L(\Delta p_{IG}-\frac{Z\rho_L\rho_G}{X})(u_i^2-2u_iu_L+\lambda_6\lambda_7)} & 0 & -\frac{u_L(-\rho_G+\rho_L)}{\rho_G} & 0 & 0 & \frac{\lambda_6(\alpha_B\rho_G+\alpha_L\rho_L)}{\alpha_B\rho_G} & \frac{\lambda_7(\alpha_B\rho_G+\alpha_L\rho_L)}{\alpha_B\rho_G} \\
\frac{\alpha_B\rho_G(\Delta p_{IL}-\frac{K\rho_L\rho_G}{Y})(-u_i^2+2u_iu_G-\lambda_4\lambda_5)(\alpha_G\rho_G+\alpha_D\rho_L)}{\alpha_D\rho_L(\Delta p_{IG}-\frac{Z\rho_L\rho_G}{X})(u_i^2-2u_iu_L+\lambda_6\lambda_7)(\alpha_B\rho_G+\alpha_L\rho_L)} & 0 & 1 & 0 & 0 & 1 & 1 \\
1 & 1 & 0 & 1 & 1 & 0 & 0
\end{bmatrix}.$$

(A.22)

$$\mathbf{R^{-1}} =$$

$$\begin{bmatrix}
\frac{\alpha_D\rho_L(-\Delta p_{IG}+\frac{Z\rho_L\rho_G}{X})}{(-u_i^2+2u_iu_G-\lambda_4\lambda_5)(\alpha_G\rho_G+\alpha_D\rho_L)} & 0 & 0 & 0 & 0 & 0 & 0 \\
0 & -\frac{\alpha_D\rho_L}{(\alpha_D+\alpha_G)\rho_G} & 0 & 0 & 0 & 0 & \frac{\alpha_G}{(\alpha_D+\alpha_G)} \\
0 & 0 & -\frac{\alpha_B\rho_G}{(\alpha_B+\alpha_L)\rho_L} & 0 & 0 & \frac{\alpha_L}{(\alpha_B+\alpha_L)} & 0 \\
\frac{\alpha_D\rho_L(-\Delta p_{IG}+\frac{Z\rho_L\rho_G}{X})(-u_i+\lambda_5)}{2(u_i^2-2u_iu_G+\lambda_4\lambda_5)(\lambda_5-u_G)(\alpha_G\rho_G+\alpha_D\rho_L)} & \frac{\alpha_D\rho_L\left[\frac{u_G\alpha_D(-\rho_G+\rho_L)}{\alpha_G\rho_G+\alpha_D\rho_L}-\lambda_5\right]}{2(\lambda_5-u_G)[-(\alpha_D+\alpha_G)\rho_G]} & 0 & -\frac{\alpha_D\rho_L}{2(\lambda_5-u_G)(\alpha_G\rho_G+\alpha_D\rho_L)} & 0 & 0 & \frac{\alpha_D\rho_L\left[\frac{u_G\alpha_G(\rho_G-\rho_L)}{\alpha_G\rho_G+\alpha_D\rho_L}-\lambda_5\right]}{2(\lambda_5-u_G)[-(\alpha_D+\alpha_G)\rho_L]} \\
\frac{\alpha_D\rho_L(-\Delta p_{IG}+\frac{Z\rho_L\rho_G}{X})(u_i-\lambda_4)}{2(u_i^2-2u_iu_G+\lambda_4\lambda_5)(\lambda_5-u_G)(\alpha_G\rho_G+\alpha_D\rho_L)} & \frac{\alpha_D\rho_L\left[\frac{u_G\alpha_D(\rho_G-\rho_L)}{\alpha_G\rho_G+\alpha_D\rho_L}+\lambda_4\right]}{2(\lambda_5-u_G)[-(\alpha_D+\alpha_G)\rho_G]} & 0 & \frac{\alpha_D\rho_L}{2(\lambda_5-u_G)(\alpha_G\rho_G+\alpha_D\rho_L)} & 0 & 0 & \frac{\alpha_D\rho_L\left[\frac{u_G\alpha_G(-\rho_G+\rho_L)}{\alpha_G\rho_G+\alpha_D\rho_L}+\lambda_4\right]}{2(\lambda_5-u_G)[-(\alpha_D+\alpha_G)\rho_L]} \\
-\frac{\alpha_B\rho_G(-\Delta p_{IL}+\frac{K\rho_L\rho_G}{Y})(-u_i+\lambda_7)}{2(u_i^2-2u_iu_L+\lambda_6\lambda_7)(\lambda_7-u_L)(\alpha_B\rho_G+\alpha_L\rho_L)} & 0 & \frac{\alpha_B\rho_G\left[\frac{u_L\alpha_B(\rho_G-\rho_L)}{\alpha_B\rho_G+\alpha_L\rho_L}-\lambda_7\right]}{2(\lambda_7-u_L)[-(\alpha_B+\alpha_L)\rho_L]} & 0 & -\frac{\alpha_B\rho_G}{2(\lambda_7-u_L)(\alpha_B\rho_G+\alpha_L\rho_L)} & \frac{\alpha_B\rho_G\left[\frac{u_L\alpha_L(-\rho_G+\rho_L)}{\alpha_B\rho_G+\alpha_L\rho_L}-\lambda_7\right]}{2(\lambda_7-u_L)[-(\alpha_B+\alpha_L)\rho_G]} & 0 \\
-\frac{\alpha_B\rho_G(-\Delta p_{IL}+\frac{K\rho_L\rho_G}{Y})(u_i-\lambda_6)}{2(u_i^2-2u_iu_L+\lambda_6\lambda_7)(\lambda_7-u_L)(\alpha_B\rho_G+\alpha_L\rho_L)} & 0 & \frac{\alpha_B\rho_G\left[\frac{u_L\alpha_B(\rho_G-\rho_L)}{\alpha_B\rho_G+\alpha_L\rho_L}+\lambda_6\right]}{2(\lambda_7-u_L)[-(\alpha_B+\alpha_L)\rho_L]} & 0 & \frac{\alpha_B\rho_G}{2(\lambda_7-u_L)(\alpha_B\rho_G+\alpha_L\rho_L)} & \frac{\alpha_B\rho_G\left[\frac{u_L\alpha_L(\rho_G-\rho_L)}{\alpha_B\rho_G+\alpha_L\rho_L}+\lambda_6\right]}{2(\lambda_7-u_L)[-(\alpha_B+\alpha_L)\rho_G]} & 0
\end{bmatrix}.$$

(A.23)

Appendix B – Single Phase Test

Single phase tests were conducted in order to ensure that the DP sensors of the experimental facilities were working properly. The total pressure gradient is a sum of the frictional, gravitational and acceleration pressure gradients. For single phase flow, those three terms can be calculated, based on the mass and momentum conservation laws, according to

$$-\frac{dp}{dL} = \frac{2}{D} f_F \rho u^2 + \rho g \sin\theta + \rho u \frac{du}{dL}, \tag{B.1}$$

where f_F is the Fanning friction factor, u is the fluid velocity. This equation is simplified, based on the totally developed flow condition,

$$-\frac{dp}{dL} = \frac{2}{D} f_F \rho u^2 + \rho g \sin\theta \tag{B.2}$$

and $f_F = C_f \mathrm{Re}^{-n}$, in which $C_f = 16$ and $n = 1$ for laminar flow and $C_f = 0.046$ and $n = 0.2$. For the 4-in facility, test for different inclination angles were performed and the comparison between the experimental result and the calculated DPs are presented in Figs. B.1 to B.3 with less than 5% error for all the sensors.

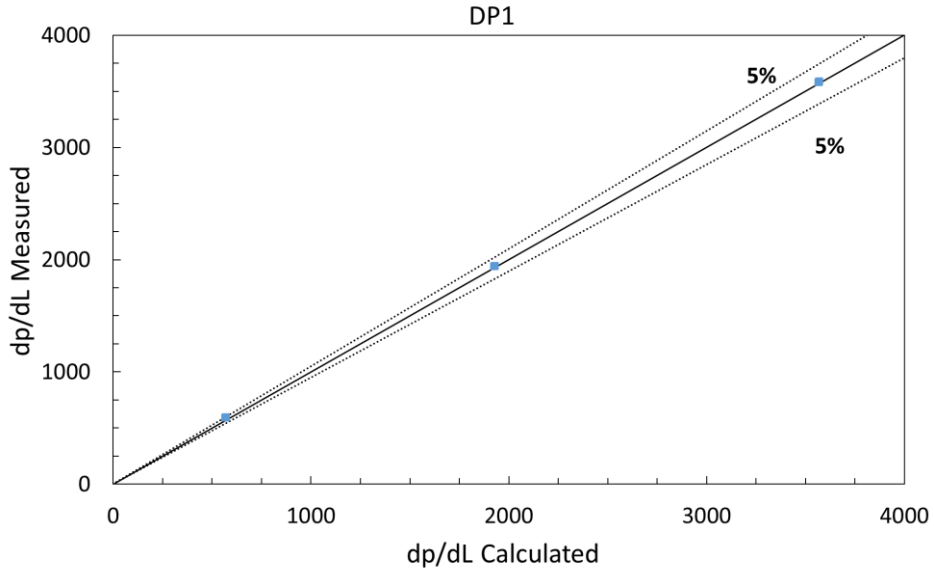

Figure B. 1: 4-in facility single phase test for DP1.

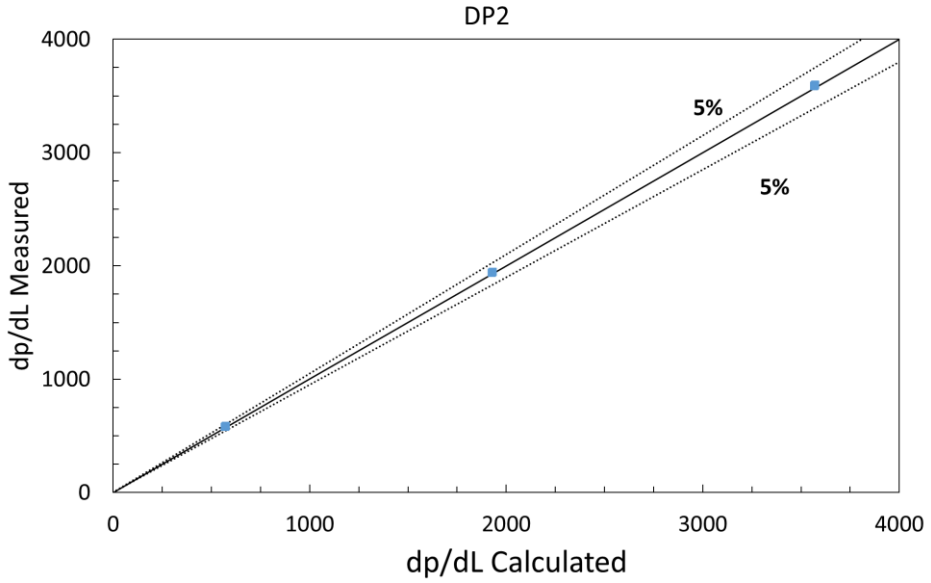

Figure B. 2: 4-in facility single phase test for DP2.

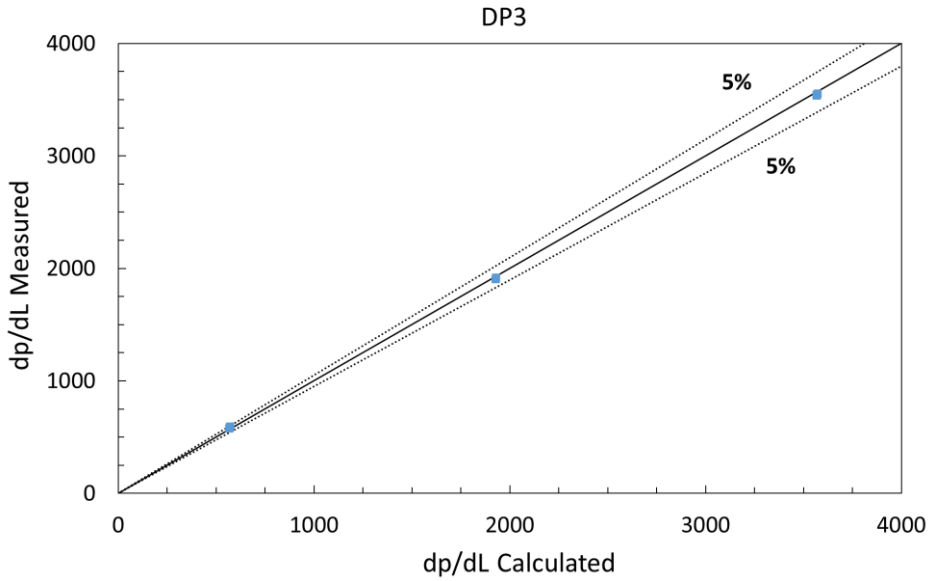

Figure B. 3: 4-in facility single phase test for DP3.

The single phase test was repeated for the DP sensors located at the 2-in facility. In the following graphs, the DP calculated, and the DP measured are compared.

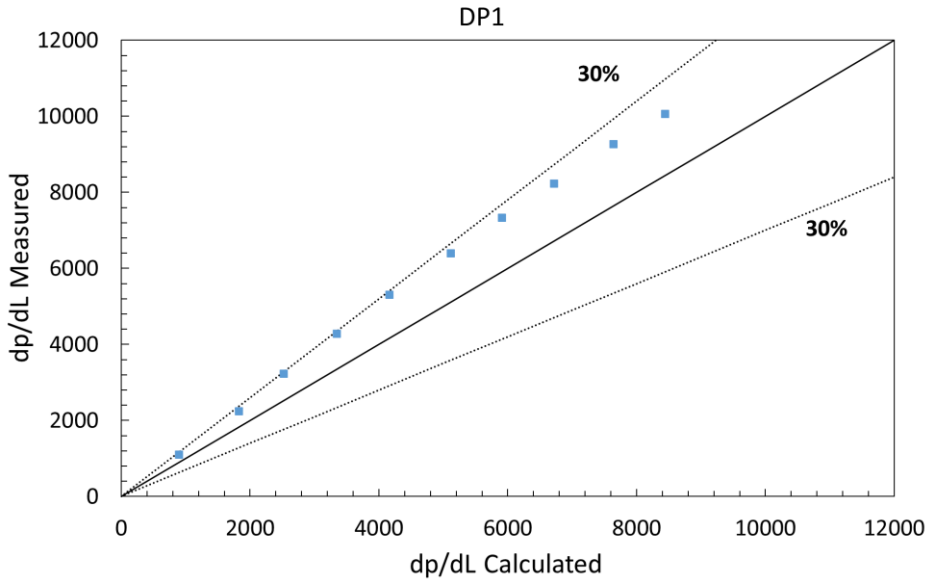

Figure B. 4: 2-in facility single phase test for DP1.

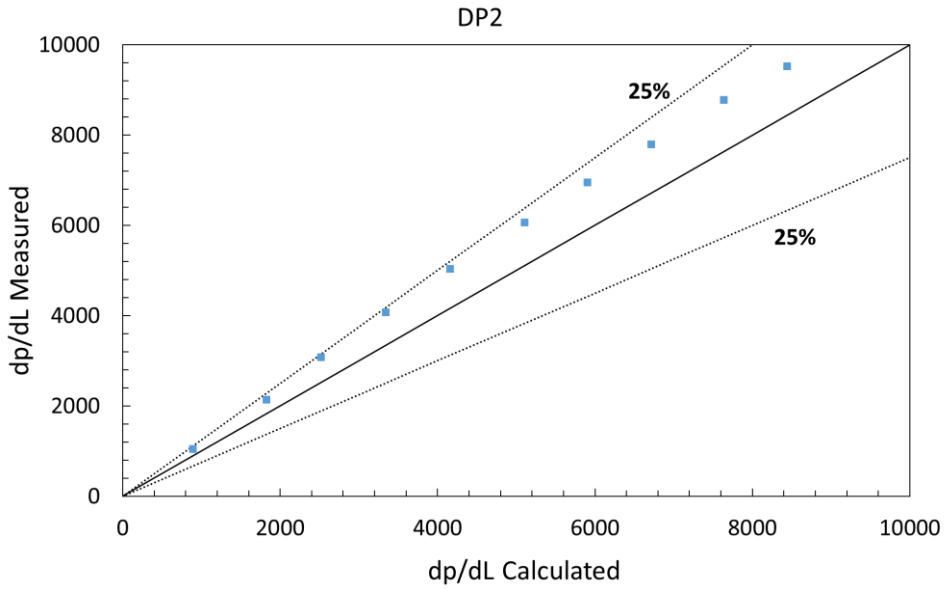

Figure B. 5: 2-in facility single phase test for DP2.

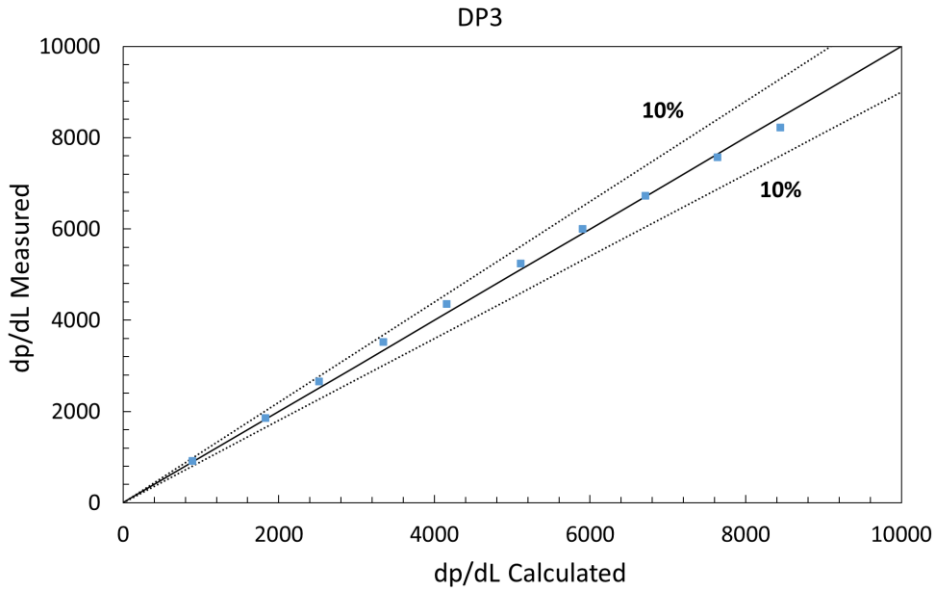

Figure B. 6: 2-in facility single phase test for DP3.

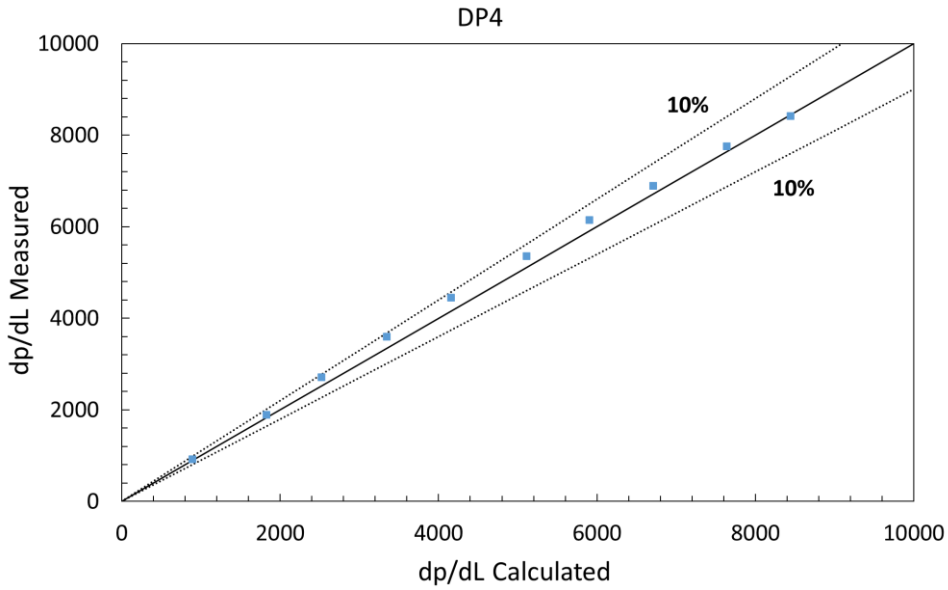

Figure B. 7: 2-in facility single phase test for DP4.

According to Figs. B.4 to B.7, the errors for DP1 and DP2 are higher than DP3 and DP4. Even though the percentage error for DP1 and DP2 are relatively low, the results obtained with DP3 and DP4 are the ones considered in this work.

Appendix C – Uncertainty Analysis

Experimental measurements are performed to quantify and guide the understanding of a physical event. However, errors are intrinsically present in all measurement and they must be estimated in order to have a better confidence in the obtained results. The uncertainty analysis estimates the limits of the error and gives reliability in the results.

There are two types of error: the random (precision error) and the systematic error (bias error). Random errors are generated by random oscillations intrinsic to the measurements and changes from one reading to other, while systematic errors are constant for all experiments and are caused by calibration errors, data acquisition errors, etc. The random and systematic uncertainties are calculated below, according to Dieck (2007), Gokcal (2008), Fan (2017) and Zhu (2019).

- Random Uncertainty

Considering N_p the number of data points, X_i the value of the i^{th} measurement and $\bar{X}$ is the average value of all data points, the standard deviation of the average can be obtain as follows

$$S_X = \sqrt{\frac{\sum_{i=1}^{N_p}(X_i - \bar{X})^2}{N_p - 1}}. \tag{C.1}$$

The standard deviation of the average is given by

$$S_{\bar{X}} = \frac{S_X}{\sqrt{N_p}}. \tag{C.2}$$

- Systematic Uncertainty

The systematic error from different sources can be combined and calculated as

$$b_R = \left(\sum_{i=1}^{N_S} (b_i)^2 \right)^{1/2}, \tag{C.3}$$

where b_R is the combined systematic uncertainty of the test result, b_i corresponds to each source of the systematic uncertainty and N_S is the number of systematic uncertainty source. Tables C.1 and C.2 presents the systematic uncertainty of the instruments for each experimental facility used.

Table C. 1: Systematic uncertainty of instruments for the 4-in facility.

Instrument	Measured Variable	Systematic Uncertainty
Promass 83F	Gas Mass Flow Rate	±0.35%
Promass 83F	Liquid Mass Flow Rate	±0.10%
Rosemount 3051S2	Differential Pressure	±0.15%
Rosemount 300S1	Pressure	±0.15%
Rosemount 3144P	Temperature	±0.25°F
Digital Angle Finder	Inclination Angle	±0.2°

Table C. 2: Systematic uncertainty of instruments for the 2-in facility.

Instrument	Measured Variable	Systematic Uncertainty
MicroMotion™	Gas Mass Flow Rate	±0.1%
MicroMotion™	Liquid Mass Flow Rate	±0.1%
RTD	Temperature	±0.5°C
Rosemount	Pressure	±0.1%
Rosemount	Differential Pressure	±0.1%

- Combination of random and systematic uncertainty

Random and systematic uncertainty are combined according to

$$U_{95} = \pm t_{95}\left[\left({}^{b_R}/_{2}\right)^2 + (S_{\bar{X}})^2\right]^{1/2}, \qquad \text{(C.4)}$$

where U_{95} is the overall uncertainty, t_{95} is the student-t coefficient of 95%.

- Uncertainty Propagation

The uncertainty propagation is calculated whenever a parameter is calculated from two or more parameters that can be directly measured by the instrumentation. The uncertainty propagation is applied, for instance, for the superficial gas and liquid velocities. It is calculated according to Taylor's series as

$$U(f(x_1, x_2, \dots, x_m)) = \sqrt{\sum_{i=1}^{m} \left(\frac{\partial f}{\partial x_i} U(x_i)\right)^2}, \tag{C.5}$$

where U is the propagated uncertainty and x_i are the independent parameter that are directly measured.

According to Soedarmo (2019), the slug frequency systematic uncertainty calculation consider that one slug can be incorrectly accounted close to the start and end of the measurement. Besides that, the difference between the slug count of the sensors is added into the frequency uncertainty calculation. For the slug frequency, random uncertainty is not applicable.

The following table, Table C.3, presents the experimental data acquired for the 2inch and 4inch facilities and their calculated uncertainties. First, the 2inch high viscosity oil/air facility results are displayed. Then, the results for the 4-inch water/air facility are presented separated by each inclination angle.

Table C. 3: Experimental data and uncertainties.

2-inch High viscosity Oil/Air Indoor Facility															
Gas mass flow rate [kg/s]	Uncertainty [kg/s]	Liquid mass flow rate [kg/s]	Uncertainty [kg/s]	Usg [m/s]	Uncertainty [m/s]	Usl [m/s]	Uncertainty [m/s]	Um [m/s]	Uncertainty [m/s]	dP/dx [Pa/m]	Uncertainty [Pa/m]	Slug frequency [1/s]	Uncertainty [1/s]	Translational velocity [m/s]	Uncertainty [m/s]
0.000583	0.000115	0.183	0.005	0.177	0.036	0.106	0.002	0.283	0.036	857.79	28.43	0.597	0.023	0.754	0.003
0.000877	0.000114	0.178	0.005	0.267	0.036	0.103	0.002	0.370	0.036	851.42	33.50	0.818	0.032	0.992	0.010
0.001180	0.000115	0.179	0.005	0.358	0.036	0.104	0.002	0.462	0.036	907.34	30.27	0.916	0.016	1.202	0.002
0.001467	0.000114	0.179	0.005	0.440	0.036	0.104	0.002	0.544	0.036	949.96	31.76	1.011	0.030	1.402	0.008
0.000349	0.000114	0.346	0.009	0.092	0.031	0.200	0.004	0.292	0.032	1541.68	25.40	1.347	0.024	0.741	0.008
0.000667	0.000113	0.350	0.004	0.174	0.031	0.203	0.002	0.377	0.031	1621.60	25.07	1.749	0.024	0.961	0.003
0.001040	0.000114	0.347	0.007	0.269	0.031	0.201	0.004	0.470	0.031	1689.23	34.52	1.893	0.024	1.201	0.005
0.001380	0.000115	0.344	0.008	0.357	0.031	0.200	0.004	0.557	0.031	1738.43	35.16	1.972	0.016	1.429	0.002
0.001720	0.000114	0.342	0.008	0.441	0.031	0.198	0.004	0.639	0.031	1763.98	38.17	2.099	0.015	1.663	0.004
0.002080	0.000119	0.343	0.007	0.524	0.032	0.199	0.004	0.723	0.032	1867.26	78.89	2.056	0.016	1.871	0.009
0.000351	0.000114	0.434	0.008	0.085	0.029	0.252	0.004	0.337	0.029	2055.04	49.60	1.852	0.016	0.833	0.003
0.000737	0.000114	0.433	0.006	0.177	0.029	0.252	0.003	0.429	0.029	2082.95	38.54	2.383	0.023	1.084	0.006
0.001110	0.000114	0.427	0.004	0.266	0.029	0.248	0.002	0.514	0.029	2128.09	27.37	2.559	0.015	1.311	0.002
0.001480	0.000113	0.419	0.007	0.356	0.029	0.243	0.003	0.599	0.029	2133.15	38.23	2.261	0.024	1.539	0.004
0.001840	0.000116	0.424	0.004	0.437	0.029	0.247	0.002	0.684	0.029	2197.24	28.77	2.145	0.016	1.755	0.012
0.000793	0.000116	0.525	0.004	0.178	0.027	0.305	0.002	0.483	0.027	2541.51	28.40	3.053	0.030	1.205	0.008
0.002520	0.000114	0.517	0.007	0.521	0.026	0.301	0.003	0.822	0.026	2795.98	31.54	2.609	0.015	2.125	0.009
0.003180	0.000115	0.695	0.004	0.058	0.024	0.404	0.003	0.462	0.026	3245.57	27.03	3.176	0.065	1.098	0.007
0.000908	0.000114	0.694	0.008	0.179	0.023	0.403	0.002	0.582	0.023	3399.63	30.16	4.629	0.023	1.424	0.008
0.001114	0.000117	0.683	0.008	0.219	0.024	0.397	0.004	0.615	0.024	3451.14	27.91	4.354	0.024	1.521	0.014
0.002780	0.000114	0.683	0.007	0.527	0.023	0.397	0.003	0.924	0.023	3669.69	34.67	2.979	0.047	2.377	0.003
0.000253	0.000114	0.085	0.004	0.085	0.040	0.049	0.002	0.134	0.040	434.16	36.65	0.140	0.016	0.433	0.008
0.000506	0.000114	0.084	0.004	0.170	0.040	0.049	0.002	0.219	0.040	398.07	24.82	0.137	0.013	0.622	0.015
0.000797	0.000113	0.084	0.004	0.270	0.041	0.049	0.002	0.319	0.040	391.13	25.29	0.159	0.016	0.844	0.021
0.001304	0.000115	0.085	0.004	0.441	0.041	0.049	0.002	0.490	0.041	418.03	24.93	0.194	0.016	1.244	0.015
4-inch Water/Air Facility - Inclination: 2°															
Gas mass flow rate [kg/s]	Uncertainty [kg/s]	Liquid mass flow rate [kg/s]	Uncertainty [kg/s]	Usg [m/s]	Uncertainty [m/s]	Usl [m/s]	Uncertainty [m/s]	Um [m/s]	Uncertainty [m/s]	dP/dx [Pa/m]	Uncertainty [Pa/m]	Slug frequency [1/s]	Uncertainty [1/s]	Translational velocity [m/s]	Uncertainty [m/s]
0.0152	0.000682	0.410	0.006	0.270	0.013	0.0500	0.00071	0.320	0.013	295.06	8.92	0.354	0.010	1.100	0.012
0.0228	0.000666	0.409	0.006	0.400	0.013	0.0500	0.00074	0.450	0.013	256.66	11.84	0.301	0.030	1.314	0.031
0.0378	0.000685	0.410	0.006	0.670	0.014	0.0500	0.00073	0.720	0.014	183.63	13.48	0.257	0.020	1.607	0.044
0.0604	0.000708	0.410	0.006	1.080	0.014	0.0500	0.00072	1.130	0.014	122.16	15.34	0.194	0.025	2.082	0.062

4-inch Water/Air Facility - Inclination: 5°															
Gas mass flow rate [kg/s]	Uncertainty [kg/s]	Liquid mass flow rate [kg/s]	Uncertainty [kg/s]	Usg [m/s]	Uncertainty [m/s]	Usl [m/s]	Uncertainty [m/s]	Um [m/s]	Uncertainty [m/s]	dP/dx [Pa/m]	Uncertainty [Pa/m]	Slug frequency [1/s]	Uncertainty [1/s]	Translational velocity [m/s]	Uncertainty [m/s]
0.0228	0.0007	0.407	0.006	0.400	0.013	0.0500	0.0007	0.450	0.013	549.35	10.39	0.426	0.020	1.216	0.011
0.0379	0.0007	0.406	0.006	0.670	0.013	0.0500	0.0007	0.720	0.013	461.49	13.79	0.385	0.040	1.521	0.023
0.0604	0.0007	0.406	0.006	1.070	0.014	0.0500	0.0007	1.120	0.014	346.06	15.89	0.279	0.015	2.027	0.037

4-inch Water/Air Facility - Inclination: 15°															
Gas mass flow rate [kg/s]	Uncertainty [kg/s]	Liquid mass flow rate [kg/s]	Uncertainty [kg/s]	Usg [m/s]	Uncertainty [m/s]	Usl [m/s]	Uncertainty [m/s]	Um [m/s]	Uncertainty [m/s]	dP/dx [Pa/m]	Uncertainty [Pa/m]	Slug frequency [1/s]	Uncertainty [1/s]	Translational velocity [m/s]	Uncertainty [m/s]
0.0228	0.0007	0.409	0.006	0.400	0.012	0.0500	0.0007	0.450	0.012	1712.04	20.79	0.726	0.042	1.466	0.018
0.0378	0.0007	0.408	0.006	0.670	0.013	0.0500	0.0007	0.720	0.013	1408.06	58.98	0.585	0.020	1.688	0.034
0.0605	0.0007	0.408	0.006	1.070	0.013	0.0500	0.0007	1.120	0.013	1033.72	28.21	0.488	0.010	2.114	0.024

4-inch Water/Air Facility - Inclination: 20°															
Gas mass flow rate [kg/s]	Uncertainty [kg/s]	Liquid mass flow rate [kg/s]	Uncertainty [kg/s]	Usg [m/s]	Uncertainty [m/s]	Usl [m/s]	Uncertainty [m/s]	Um [m/s]	Uncertainty [m/s]	dP/dx [Pa/m]	Uncertainty [Pa/m]	Slug frequency [1/s]	Uncertainty [1/s]	Translational velocity [m/s]	Uncertainty [m/s]
0.0229	0.0007	0.408	0.006	0.400	0.012	0.0500	0.0007	0.450	0.012	2274.04	36.96	0.824	0.055	1.516	0.023
0.0378	0.0007	0.407	0.006	0.660	0.013	0.0500	0.0007	0.710	0.013	1844.81	57.00	0.651	0.010	1.722	0.013
0.0606	0.0007	0.408	0.006	1.060	0.013	0.0500	0.0007	1.110	0.013	1414.61	17.51	0.542	0.015	2.161	0.043

4-inch Water/Air Facility - Inclination: 30°															
Gas mass flow rate [kg/s]	Uncertainty [kg/s]	Liquid mass flow rate [kg/s]	Uncertainty [kg/s]	Usg [m/s]	Uncertainty [m/s]	Usl [m/s]	Uncertainty [m/s]	Um [m/s]	Uncertainty [m/s]	dP/dx [Pa/m]	Uncertainty [Pa/m]	Slug frequency [1/s]	Uncertainty [1/s]	Translational velocity [m/s]	Uncertainty [m/s]
0.0228	0.0007	0.408	0.006	0.400	0.012	0.0500	0.0007	0.450	0.012	3354.65	38.52	0.926	0.015	1.580	0.022
0.0376	0.0007	0.407	0.006	0.670	0.013	0.0500	0.0007	0.720	0.013	2637.15	68.53	0.768	0.035	1.741	0.027
0.0607	0.0007	0.408	0.006	1.070	0.013	0.0500	0.0007	1.120	0.013	1907.08	40.67	0.648	0.030	2.156	0.030